NASA Technical Paper 1626

Viscous-Inviscid Calculations of Jet Entrainment Effects on the Subsonic Flow Over Nozzle Afterbodies

Richard G. Wilmoth

APRIL 1980

NASA

NASA Technical Paper 1626

Viscous-Inviscid Calculations of Jet Entrainment Effects on the Subsonic Flow Over Nozzle Afterbodies

Richard G. Wilmoth
Langley Research Center
Hampton, Virginia

SUMMARY

A viscous-inviscid interaction model has been developed to account for jet entrainment effects in the prediction of the subsonic flow over nozzle afterbodies. The jet entrainment model is based on the concept of a weakly interacting shear layer in which the local streamline deflections due to entrainment are accounted for by a displacement-thickness type of correction to the inviscid plume boundary. The entire flow field is solved in an iterative manner to account for the effects on the inviscid external flow of the turbulent boundary layer, the turbulent mixing and chemical reactions in the shear layer, and the inviscid jet exhaust flow. The individual components of the computational model are described, and numerical results are presented to illustrate the interactive effects of entrainment on the overall flow structure. The validity of the interactive model is assessed by comparisons with data obtained from flow-field measurements on cold-air jet exhausts. Numerical results and experimental data are also given to show the entrainment effects on nozzle boattail drag under various jet exhaust and free-stream flow conditions.

INTRODUCTION

The prediction of nozzle boattail drag requires an accurate description of several flow regions with widely different flow characteristics (see fig. 1). The flow field is typically characterized by relatively large turbulent boundary layer and turbulent mixing regions and an underexpanded or overexpanded jet exhaust flow. The mutual interactions between these various regions are particularly important at subsonic and transonic speeds. While analyses based on solving the Reynolds averaged Navier-Stokes equations can provide a description of this complex flow field, the computer resources required to achieve adequate resolution are generally prohibitive for engineering computations. Therefore, most engineering predictions are made by using the so-called patched viscous-inviscid interaction procedure in which the separate flow regions are solved iteratively (e.g., see refs. 1 to 5). This patched procedure has been shown to account adequately for the effects of jet plume blockage and boundary-layer displacement on nozzle boattail drag. However, jet entrainment effects either have been neglected completely by treating the inviscid jet plume boundary as an effective solid body (see refs. 1 and 2) or an entrainment correction based on a simple isobaric mixing model has been applied to the inviscid boundary (see refs. 3 to 5). Such approximations appear to be reasonable for jets operating near ideal design conditions. However, where a mismatch exists between jet exhaust and external stream velocities and pressures, jet entrainment can produce a rather large effect on the nozzle drag (see ref. 6). The use of such approximations typically leads to a significant underprediction of the drag (see refs. 7 and 8).

A measure of the effect of jet entrainment on nozzle boattail drag can be obtained by comparing experimental data for cold-air jets with those for a

solid plume simulator. Such a comparison, based on the data of Reubush (ref. 9), is shown in figure 2 for two circular-arc boattails, one with an attached boundary layer and the other with a separated boundary layer. In each case the increment in boattail drag coefficient between the cold-air jet and solid simulator is about one-half of the value for the cold-air jet. Evidence that this increment is primarily attributable to entrainment effects is shown in figure 3 where the relative drag increment is seen to correlate well with the shear-layer velocity ratio. The band of data in figure 3 was obtained from the drag measurements of Reubush for eight different circular-arc nozzles having boattail chord angles β_c ranging from about 8° to 17° and free-stream Mach numbers ranging from 0.4 to 0.9. These data show clearly that the use of solid plume simulators which simulate only the inviscid plume shape can lead to significant errors in determining nozzle boattail drag except near ideal design conditions; that is, where the velocity ratio is unity. It can also be inferred that similar errors will occur in predictions that neglect the effects of jet entrainment.

As a result of the evident need to account for jet entrainment effects, an effort has been undertaken to develop a more accurate computational approach for including such effects within the framework of viscous-inviscid interaction techniques. This goal has been accomplished by developing a computational model (ref. 10) which treats the turbulent mixing and thermochemical processes occurring in near-field shear layers of jet exhaust plumes while interacting with the inviscid exhaust and external flow fields in a unique, overlaid manner. The external inviscid and boundary-layer flow fields are computed with a viscous-inviscid interaction procedure used previously for predicting nozzle boattail drag at subsonic and transonic speeds (ref. 2), whereas the inviscid exhaust flow field is computed with a modified version of the supersonic jet exhaust model described in reference 11. The entrainment effect on the inviscid, external flow field is obtained by displacing the inviscid plume boundary such that the induced inviscid mass flow crossing the outer shear-layer boundary is that predicted by the turbulent mixing solution. The entire flow field is then solved iteratively.

Preliminary results (refs. 8 and 12) from the application of the computational model to the prediction of nozzle boattail pressures have shown good agreement with experimental data for cold-air jet exhausts. These results indicated that the major contribution to the entrainment effect on the inviscid flow resulted from the acceleration or "washing away" of the external boundary-layer defect by the jet momentum and that this washing away was quite sensitive to the pressure gradients typically found near the end of nozzle boattails. Furthermore, the resultant nozzle drag predictions obtained in reference 8 were found to be quite sensitive to temperature and density gradients across the mixing layer. However, in view of the various model approximations used in both of these preliminary studies, a more thorough examination of the sensitivity of the predictions to both model and flow-field parameters is needed.

The purpose of this paper is to give a complete description of the viscous-inviscid interactive model of jet entrainment and to assess the accuracy of this model for predicting nozzle boattail pressures and drag. A derivation of the model is given to show clearly the analogy to the displacement-thickness concept used in conventional boundary-layer theory. Results of numerical experiments

are presented to show qualitatively how the inviscid flow field is modified by entrainment. The model is then applied to the prediction of nozzle afterbody flows, and results are given to indicate the sensitivity of these predictions to local pressure gradients, boundary layers, and turbulence models. The validity of the interactive approach is assessed by comparisons with flow-field data and drag measurements for nozzle boattails with cold-air jet exhausts. Drag predictions are also presented to show the expected trends due to temperature and density variations and possible external afterburning chemical reactions.

The methodology for incorporating the entrainment correction into a viscous-inviscid interaction approach was developed jointly by the author and Sanford M. Dash and Harold S. Pergament of the Aeronautical Research Associates of Princeton, Inc., who also developed the overlaid computational model for the mixing-layer calculation.

SYMBOLS

A	boattail cross-sectional area, cm^2
A_{max}	maximum cross-sectional area, cm^2
C_D	boattail pressure drag coefficient, $\dfrac{1}{A_{max}} \displaystyle\int_0^{l} C_p \, dA$
C_p	static-pressure coefficient, $\dfrac{p - p_\infty}{q_\infty}$
d_b	boattail base diameter, cm
D	boattail maximum diameter, cm
I_1, I_2	integrals defined by equations (A3) and (A4), respectively
$k\varepsilon 2$	two-equation kinetic-energy turbulence model
l	axial length of boattail; total width of mixing layer, cm
l_m	mixing length, cm
L	length of forebody from nose to start of boattail, cm
$\dot{m}$	mass-flow rate, g/s
M	Mach number
ML	Prandtl mixing-length turbulence model
NPR	nozzle pressure ratio; ratio of jet total pressure to free-stream static pressure
N_{Re}	Reynolds number

3

p	static pressure, Pa
p_t	total pressure, Pa
q	dynamic pressure, Pa
r	radial distance from axis, cm
r_B	body radius, cm
r_e	distance from axis to outer edge of mixing layer, cm
r_i	radius of inviscid jet core, cm
R	gas constant, J/g-K
T	temperature, K
u	axial component of velocity, cm/s
v	radial component of velocity, cm/s
W	molecular weight, g/g-mol
x	axial distance, cm
β_c	boattail chord angle; angle measured clockwise from horizontal to line intersecting start and end of boattail, deg
γ	ratio of specific heats
δ	boundary-layer thickness, cm
δ^*	displacement thickness, cm
Δ	incremental value
η	nondimensional shear-layer coordinate
θ_f	local flow angle, deg
μ	turbulent viscosity coefficient, g/cm-s
ξ	coordinate along outer shear-layer computational boundary, cm
ρ	density, g/cm^3
σ	dimensionless spread-rate parameter (eq. (A9))
ψ	stream-function coordinate (eq. (1))
ω	underrelaxation parameter (eq. (9))

Subscripts:

bl   external boundary layer

e   inviscid external flow property

eff   conditions at effective plume boundary

ent   entrainment

j   inviscid jet exhaust property

∞ free-stream condition

β boattail surface

1   inner mixing-layer boundary

2   outer mixing-layer boundary

Superscript:

I   equivalent inviscid property

ANALYSIS

Definition of Jet Entrainment

Consider an axisymmetric jet exhausting parallel to an external stream such that the two streams are at the same pressure but have different velocities. In the absence of viscous forces, the two streams will remain parallel with a discontinuous velocity (free shear) at the inviscid jet boundary. It is well known that this free shear boundary cannot be maintained but will be dissipated by viscous forces as the two flows move downstream. Thus a (usually turbulent) mixing layer is created and spreads both inward and outward until at a sufficiently long distance downstream a uniform velocity profile is achieved. If the jet velocity is greater than the external stream velocity, the external stream will be locally accelerated along the outer edge of the mixing region. Thus mass will be entrained into the mixing region and the external streamlines will be deflected to account for this mass entrained. The amount of streamline deflection produced by the mixing is then defined as the jet entrainment effect since, in the absence of mixing, no deflections would be produced.

In order to illustrate the magnitude of these deflections, a simple incompressible model (described in appendix A) of the mixing region was constructed and used to calculate streamline patterns for various ratios of jet velocity to free-stream velocity. The results are presented in figure 4. Streamlines are presented for a constant increment $\Delta\psi = \psi_j$, where the stream function ψ is defined in the usual manner by

$$\psi(r,x) = \sqrt{2 \int_0^r \rho u r' \, dr'} \tag{1}$$

(Thus $\pi\psi^2$ is the total mass flow in the stream tube.) The dividing streamline $\psi = \psi_j$ is indicated by a dashed line in figure 4, whereas the assumed mixing region is indicated by the shaded area.

When the jet and free-stream velocities are equal ($u_j/u_\infty = 1$ in fig. 4), no entrainment occurs and all streamlines are parallel. However, as the velocity ratio increases, mass is entrained and the streamlines are deflected inward. In the limiting case $u_j/u_\infty \rightarrow \infty$, which represents a jet exhausting into still air, the only external motion is that induced by jet entrainment. This induced flow is that required to satisfy conservation of mass and momentum in the mixing layer. A relative measure of the magnitude of the entrainment effect at any velocity ratio is given by the local streamline slope which is equal to the local radial-to-axial velocity ratio v/u. If v/u is known along some arbitrary boundary in the region where the flow is predominantly inviscid (such as the outer mixing-layer boundary), the external flow field (outside the mixing layer) may be solved by purely inviscid techniques with the entrainment effect introduced by specifying the known $v/u = v_e/u_e$ as a boundary condition. This idea forms the basis for the interactive model used in this paper.

Derivation of Interactive Model

Previous viscous-inviscid studies of jet entrainment effects (refs. 3 to 5) have employed a displacement-thickness correction to the inviscid plume boundary. In one of these studies (ref. 3) a simple, integral approach similar to that used in integral boundary-layer procedures was used for the mixing analysis, whereas the other studies (refs. 4 and 5) used the two-dimensional, constant-pressure mixing analysis of Korst and Chow (ref. 13). The displacement-thickness concept would appear to be a valid first-order attempt to introduce the streamline deflections associated with entrainment. However, the application of the displacement correction to the inviscid plume boundary appears to be an ad hoc assumption and the exact meaning of this correction is not clearly stated in previous studies. Furthermore, a two-dimensional, constant-pressure mixing analysis cannot be justified in applications to nozzle afterbody flows with thick external boundary layers and significant axial pressure gradients. In the following analysis, an expression is derived for an effective plume boundary (which is displaced to account for entrainment) in a manner completely analogous to that used in conventional boundary-layer theory and an attempt is made to show clearly the assumptions and approximations used in applying the expression to the prediction of nozzle afterbody flows. This interactive model is then applied in conjunction with a finite-difference mixing-layer solution to account for the local axial and radial pressure gradient variation throughout the mixing layer.

6

Effective plume boundary.- Consider the control volume shown in figure 5(a), and apply the continuity equation for axisymmetric flow given by

$$\frac{\partial \rho u}{\partial x} + \frac{1}{r} \frac{\partial \rho v r}{\partial r} = 0 \qquad (2)$$

Integrating equation (2) from the axis $(r = 0)$ to the outer edge of the mixing layer $(r = r_e)$ gives

$$\int_0^{r_e} \frac{\partial \rho u}{\partial x} r \, dr = -\rho_e v_e r_e \qquad (3)$$

By assuming that all streamline deflections are due solely to mixing (i.e., the jet is fully expanded), the term $-\rho_e v_e r_e \, \Delta x$ is defined as the mass entrained into the control volume between x and $x + \Delta x$. By referring to figure 5(b), an effective plume boundary $r_{eff}(x)$ is now sought such that the inviscid outer solution over this boundary will give the same mass entrained (i.e., mass crossing the boundary $r_e(x)$) as that given by equation (3). Integration of equation (2) from $r = r_{eff}$ to $r = r_e$ gives

$$\int_{r_{eff}}^{r_e} \frac{\partial \rho^I u^I}{\partial x} r \, dr = -\rho_e^I v_e^I r_e + \rho_{eff}^I v_{eff}^I r_{eff} \qquad (4)$$

where the superscript I denotes inviscid quantities. By applying Liebnitz' formula to the integral in equation (4) and by using the tangency condition $v_{eff}/u_{eff} = dr_{eff}/dx$, equation (4) can be written as

$$\frac{d}{dx} \int_{r_{eff}}^{r_e} \rho^I u^I r \, dr = -\rho_e^I v_e^I r_e + \rho_e^I u_e^I r_e \frac{dr_e}{dx} \qquad (5)$$

In principle, equation (5) can be solved for r_{eff} if the inviscid flow field is known. This solution would require an iterative procedure in which an initial guess is made for $r_{eff}(x)$, an inviscid outer solution is constructed subject to the tangency condition at $r = r_{eff}$, and a viscous inner solution is obtained subject to the outer boundary conditions $\rho_e = \rho_e^I$ and $u_e = u_e^I$. This iterative process would continue until the additional matching condition $v_e = v_e^I$ is met. Then the mass crossing the boundary $r = r_e(x)$ in the inviscid solution would match the mass entrainment calculated by the viscous solution.

In deriving equation (5), note that no assumption about the relative thickness of the mixing layer is required to achieve an exact mass balance between

7

the inner and outer solutions. However, consideration must also be given to the balance of momentum between the two solutions. In the near-field mixing model of reference 10, the pressure field is obtained from an inviscid solution. The viscous mixing solution is then obtained by a parabolic marching procedure with the local axial pressure gradient imposed by overlaying the mixing-layer computational grid onto the inviscid pressure field. Although the radial momentum equation is not solved directly as part of the mixing-layer solution, the radial variation in pressure predicted by the inviscid solution is imposed to account for local variations in density due to pressure. Thus, while the equation set used for the viscous solution is strictly parabolic, elliptic effects are introduced into the subsonic portion of the mixing layer in a more detailed manner than that normally used in boundary-layer interactions; that is, where dp/dr is usually assumed to be zero across the viscous layer. The use of this approximate procedure still imposes certain limitations on the class of problems that can be solved. First, the parabolic approximation in the mixing layer requires a weak coupling between the viscous and inviscid effects; that is, the mixing effects are assumed to act as a perturbation which can be super-imposed on the inviscid pressure field. Second, imposing the radial pressure variation obtained from an inviscid solution implies that the viscous forces in the radial direction are small. Both of these approximations require that the streamline deflections associated with jet entrainment be small and would appear (fig. 4) to place an upper limit on the allowable velocity ratio across the mixing layer. By using the overlaid mixing model of reference 10, the maximum streamline deflection angle for velocity ratios less than 10 was estimated to be less than about 6°. For such small angles, the radial component of the stream-wise shear stress is at least one order of magnitude less than the axial component and the overlaid approximation should be reasonable.

Application to nozzle afterbody flows.- Consistent with the usual boundary-layer-like approximation, equation (5) can be simplified by letting $\rho^I u^I$ be constant across the mixing layer and equal to the edge value $\rho_e u_e$. After some rearrangement, equation (5) becomes

$$\frac{d}{dx}\left(\frac{1}{2}\,\rho_e u_e r_{eff}^2\right) = \rho_e v_e r_e + \frac{1}{2}\,r_e^2\,\frac{d\rho_e u_e}{dx} \tag{6}$$

If the variation in $\rho_e u_e$ is small (i.e., $d\rho_e u_e/dx \approx 0$) or if the mixing layer is sufficiently thin, equation (6) can be further approximated by

$$\frac{d}{dx}\left(\frac{1}{2}\,r_{eff}^2\right) = \frac{v_e r_e}{u_e} \tag{7}$$

Thus, in the weakly interacting, thin shear-layer limit, the effect of entrainment is equivalent to a source distribution of strength $v_e r_e$ imposed along the inviscid computational boundary $r = r_j = $ Constant. (In principle, this source distribution can be transferred to any $r = $ Constant boundary as long as the source strength $v_e r_e$ is maintained at $r = r_e$. However, in axisym-

8

metric flow the effective velocity v_{eff} is approximately given by $v_{eff} \sim v_e r_e/r$ and since v_{eff}/u_e must be $\ll 1$ to apply the weak interaction approach, the choice of an appropriate boundary is limited; e.g., $r = 0$ is obviously precluded.) In the present application, the source strength is obtained from the viscous mixing solution and used in either equation (6) or (7) to obtain the effective plume boundary. Most calculations have been performed by using the simpler equation (7) which appears to give better results in the viscous-inviscid iteration procedure.

For underexpanded plumes, an additional streamline deflection occurs because of the outward expansion of the inviscid plume boundary. This plume blockage effect is included in the calculation of the term $v_e r_e/u_e$ by the overlaid procedure of reference 10 and therefore must be included in the definition of r_{eff}. Evaluation of r_{eff} in the inviscid limit (see appendix B) shows that the definition given by equation (6) or (7) does account for this inviscid plume curvature. However, for highly underexpanded plumes, the viscous contribution to the term $v_e r_e/u_e$ will be in error since the mixing-layer computational grid is not properly aligned with the inviscid plume boundary; that is, the shear stress component in the radial direction is neglected. This error diminishes as the nozzle pressure ratio decreases and is assumed to have a negligible effect on the effective boundary calculation for the mildly underexpanded jets (NPR $\lesssim$ 4) considered in this paper. An improvement in the mixing-layer calculation could be obtained by using a plume-oriented coordinate system such as that described in reference 14.

Definition of plume displacement thickness.- The effective plume boundary is defined by equation (7) only to within an arbitrary constant. (See appendix B.) This constant can be determined by requiring that the effective boundary be continuous at the nozzle exit; that is, $r_{eff} = r_j + \delta^*_{bl}$. (See fig. 6.) This initial condition provides a convenient choice for the definition of an effective displacement thickness for the plume; namely

$$\delta^*_{eff} = r_{eff} - r_j \tag{8}$$

which includes both the effect of entrainment and plume blockage. For a fully expanded jet, the inviscid plume boundary radius is constant and equal to the nozzle exit radius r_j, and this definition gives the displacement thickness due to entrainment only. Note that this definition of δ^*_{eff} is arbitrary. A definition which includes only the entrainment contribution is obtained by subtracting the inviscid plume boundary radius from r_{eff} and gives a displacement thickness similar to that defined in reference 5. However, such a definition can only be applied a posteriori since blockage and entrainment effects are not readily separable in the effective plume boundary relation given by either equation (6) or (7). Most results presented in this paper are for nearly fully expanded plumes for which the two definitions give approximately the same δ^*_{eff}.

Note that the choice of a displacement-thickness (or effective-body) concept in performing viscous-inviscid interaction calculations is somewhat arbitrary. For very thin shear layers, equivalent results can be obtained by simply

9

specifying the calculated entrainment velocity v_e along the boundary $r = r_e$. (See ref. 15.) The choice was made here on the basis of the type of boundary condition employed in the inviscid, external solution procedure of reference 16. The analogy between plume and boundary-layer displacement thickness is discussed in appendix B.

COMPUTATIONAL APPROACH

The use of the interactive model requires an iterative procedure for coupling the jet plume and boundary-layer displacement effects with the inviscid flow analyses. In developing such a procedure and in selecting the specific computational approach for each flow-field region, the following key assumptions are employed:

(1) The inviscid jet exhaust flow is supersonic at all computational boundaries; that is, upstream inflow (at nozzle exit) boundary, upper plume boundary, and downstream outflow boundary, except at the jet center line where the flow may be subsonic downstream of the normal shock (Mach disc) which develops when the jet is underexpanded $(p_j \overset{>}{=} p_\infty)$.

(2) The streamline deflections due to plume underexpansion are small $(\lesssim 10^\circ)$.

(3) The dominant viscous effect in the mixing layer is due to the turbulent shear stress in the axial direction. All other viscous forces are negligible.

(4) The external flow is inviscid and irrotational.

(5) The external boundary layer is turbulent and remains attached, that is, no reverse flow.

(6) The viscous-inviscid interaction is weak; that is, the added streamline deflections produced by viscous interaction with the boundary layer and mixing layer are small compared with the local streamline flow angles associated with purely inviscid flow.

Note that only assumption (6) is necessary for the application of the interactive jet entrainment model. All other assumptions could be eliminated, in principle at least, by the use of different computational techniques for the jet exhaust, mixing layer, external flow, and boundary layer than those chosen for the present study.

Iteration Procedure

A schematic of the main viscous-inviscid iteration loop employed in the present work is shown in figure 7. The primary computational elements of the loop and their order of calculation are: (1) an inviscid jet exhaust calculation (the SCIPPY code, ref. 11); (2) an overlaid mixing-layer calculation (the BOAT code, ref. 10); (3) an inviscid external flow calculation (the RAXBOD

code, refs. 16 and 17); and (4) a turbulent boundary-layer calculation (the Reshotko-Tucker method, ref. 18, as modified in ref. 19). To begin the loop, the external flow field is initially set to uniform free-stream conditions and the displacement thickness is set to zero. Thus, in the first pass through the loop, the inviscid jet exhaust and mixing-layer calculations are performed for a uniform external flow, whereas the first inviscid, external flow calculation is performed over the actual body geometry. The inviscid flow properties for use in the overlaid mixing-layer calculation are updated immediately after the corresponding inviscid calculation. The inviscid plume boundary shape $r_j^I(x)$ and the pressure along this boundary are also updated after the inviscid jet and external flow calculations, respectively. The loop is repeated until convergence is obtained on both $C_p(x)$ and $\delta^*(x)$.

The effective body shape for the inviscid external flow calculation is calculated by underrelaxing the displacement-thickness distribution by using

$$\delta^*(x) = \omega \delta^*_{old}(x) + (1 - \omega)\delta^*_{new}(x) \tag{9}$$

to suppress oscillations in $C_p(x)$ and $\delta^*(x)$ which typically appear in the first few iterations. For most of the results presented in this paper, $\omega = 0.5$ was sufficient to obtain a convergence level of ≤ 0.1 percent in both $C_p(x)$ and $\delta^*(x)$ in about 10 iterations. For cases with very large shear-layer velocity ratios and hot jet exhausts, $\omega = 0.75$ was required to give about the same convergence level. An indication of the typical convergence behavior of the solution is given in figure 8.

An important feature of the iteration loop shown in figure 7 is that only a single loop is required to obtain a stable iteration process. No subcycling between the various flow regions, such as that used in reference 7, appears to be needed. This simplification is made possible by a combination of the under-relaxation technique with an attempt to match as many flow properties as possible in a manner consistent with the interaction model at each stage of the iteration. For example, in the inviscid jet exhaust analysis, the pressure along the inviscid plume boundary is updated, based on the most recently calculated boundary location. Since the inviscid external flow calculation is performed over an effective viscous plume boundary, which is displaced from the inviscid boundary, an interpolation procedure is used to obtain the updated pressures along the most recently calculated inviscid plume boundary. A similar procedure is used to generate the inviscid flow maps for the shear-layer calculation. Thus, the inviscid pressure field is as self-consistent as possible among the various flow regions.

Inviscid Jet Exhaust Calculation

The assumption that the jet exhaust flow is completely supersonic except for the small region in the nozzle boundary layer and downstream of the Mach disc allows the use of steady-state marching procedures because of the hyperbolic character of the flow equations. For underexpanded jets ($p_j > p_e$), the

supersonic regions were solved by a modified version of the shock-capturing—shock-fitting model of reference 11. This model uses an explicit steady-state marching procedure to solve the conservative finite-difference form of the inviscid flow equations. The pressure is specified along the plume boundary with other boundary properties calculated by using characteristic techniques. Oblique shocks are numerically captured, whereas shock fitting is used at the triple point if a Mach disc is present in the flow. Since the flow field downstream of a Mach disc contains an embedded subsonic region, a direct marching procedure cannot be used in this region. Rather than attempting to solve this region in a rigorous fashion, a simple ad hoc model was devised to handle the flow downstream of the first Mach disc (if one was present). This model consists of: (1) Estimating the primary wavelength of the inviscid cell; (2) imposing an exponential decay for the pressure in each stream tube from its value just downstream of the Mach disc to free-stream pressure; and (3) allowing each stream tube to expand isentropically, based on the imposed pressure gradient. While this simplistic model neglects the detailed pressure variations that result from the oblique shock reflected upward from the triple point and the small perturbations introduced by the curvature of the Mach disc slipstream, it was found for mildly underexpanded plumes to give almost the same boundary shape over the first inviscid cell as the iterative shock-fitting method of Salas (ref. 20).

When the nozzle exit flow is nearly sonic and near full expansion, a supersonic marching technique is found to be very inefficient because of the small marching step size required for numerical stability of the explicit finite-difference solution. Thus, for the calculations presented in this paper at a nozzle pressure ratio of about 2, jet exhaust properties were calculated by using simple isentropic relations with the axial pressure gradient imposed by the inviscid external flow solution. Since the gradients in the flow properties are small and the plume boundary does not deviate significantly from a cylinder, this procedure was found to be sufficiently accurate and much more efficient than the use of a supersonic marching technique for such cases.

Overlaid Mixing-Layer Calculation

The computational model of reference 10 (BOAT) used to calculate the mass entrainment into the mixing layer employs an overlaid procedure shown schematically in figure 9. The inviscid flow field is first mapped into cylindrical (x,ψ) coordinates. The computational grid is then distributed across the mixing layer in evenly spaced increments in ψ. The initial profiles in velocity, density, and temperature at the nozzle exit location are determined from the boundary-layer calculation, and the solution is marched along the plume interface by integration of the parabolic mixing equations written in (x,ψ) coordinates. At each integration step, the edge conditions and the pressure and pressure gradients at each grid point are determined by direct interpolation (in (x,ψ) coordinates) from the inviscid flow maps. Thus the solution to the inviscid radial momentum equation is contained implicitly in the mixing solution by imposing $p(x,\psi)$ as a known quantity. The computational boundaries $\psi_1(x)$ and $\psi_2(x)$ are allowed to grow according to the edge rule specified in reference 21 to prevent the buildup of fictitious velocity (and other properties)

gradients at the edges of the mixing layer. The radial location of the inner boundary $\psi_1(x)$ is determined by interpolation in the inviscid jet exhaust map to account for the position and curvature of the inviscid plume boundary. The mass entrainment (per unit length) needed to calculate the effective plume boundary by equation (7) is obtained from

$$\rho_e v_e r_e = \rho_e u_e r_e \frac{dr_e}{dx} - \frac{1}{2}\left(\frac{d\psi_2}{dx}^2\right)_\xi \tag{10}$$

where ξ is along the computational boundary $\psi_2(x)$. The mass entrainment calculated in this manner thus includes contributions from both viscous (turbulent mixing) and inviscid (plume blockage) processes. In order to obtain the effective viscous plume boundary, equation (10) is combined with either equation (6) or (7) and integrated over the distance Δx corresponding to the axial length of the computational cell used in the inviscid, external flow calculation. Since the step size used in the parabolic mixing calculation is generally much smaller than the inviscid step size, the matching of the radial velocity v_e is accomplished only in an average sense over the distance Δx.

Turbulence effects are modeled by either a Prandtl mixing length (ML) model or the two-equation ($k\varepsilon 2$) model of reference 22. In using the $k\varepsilon 2$ model, parabolized transport equations for the turbulent kinetic energy and dissipation rate are solved in addition to the parabolized x-momentum and energy equations. For most cases considered in this paper, calculations were performed by using the $k\varepsilon 2$ model, and a discussion of the sensitivity of the results to the turbulence modeling is provided later in the paper. However, both models have been found to give good predictions of mean flow quantities in flows for which the pressure variations were negligible. (See ref. 10.)

The BOAT code also treats chemical reactions in the mixing layer by an implicit finite-rate chemistry solution procedure (ref. 23) for the species continuity equations. Although the implicit treatment of the chemical source terms in the species continuity equations removes the marching step stability limit associated with these terms, some reduction in step size is still necessary for cases with fast chemistry so as to reduce truncation errors which can cause negative mole fractions to be calculated. For the cases considered in this paper, the computational times are increased by about a factor of 2 owing to the reduced step size and the additional computations involved in the cases with chemistry. Because of the weak interaction hypothesis of the entrainment model, only the treatment of mildly reacting plumes should be considered by the present approach. Constant Prandtl and Lewis numbers of unity have also been assumed in all calculations.

Inviscid External Flow Calculation

The external flow calculation is performed with the relaxation technique developed by South and Jameson (ref. 16) for solving the inviscid, full potential equation for axisymmetric flow. This technique uses a body-normal coordinate system from the nose up to the first horizontal tangent and a sheared

cylindrical system aft of this point. The computational grid is stretched to infinity in physical space in both the normal and downstream axial directions to facilitate handling of the far-field boundary conditions. The upstream computational boundary lies on the axis of symmetry, whereas the lower boundary lies on the effective body surface along which the tangency boundary condition is satisfied.

For the present calculations, a cone-cylinder forebody (L/D = 8) was used ahead of the start of the afterbody to duplicate the experimental configuration of Reubush (ref. 9). This forebody produced negligible effects on the afterbody flow and was used strictly to produce the proper Reynolds number at the start of the afterbody. Since only the afterbody-exhaust region is of interest here, the axial grid points were concentrated between the start of the boattail and a point about three body diameters downstream of the nozzle exit by using the coordinate stretching functions described in reference 17. A total of 77 grid points were used in the streamwise or x-direction of which about 27 were in the afterbody-exhaust region, whereas 39 grid points were used in the normal or radial direction. For the viscous-inviscid interaction, 200 relaxation cycles were performed during each inviscid analysis.

Turbulent Boundary-Layer Calculation

The external boundary-layer displacement-thickness distribution $\delta_{bl}^*(x)$ over the forebody and afterbody up to the nozzle exit is calculated by using the integral boundary-layer method for turbulent flow given by Reshotko and Tucker (ref. 18). The integration procedure and modified form of the shear integral used are given in reference 19. The resulting displacement-thickness distribution is added to the body radius by using the relaxed value of δ^* calculated by equation (9). The value of δ_{bl}^* at the nozzle exit is used to calculate the initial profile for the mixing-layer calculation as described in reference 10.

Since the external boundary layer was quite thick compared with the internal nozzle boundary layer for the cases considered in this paper, no internal boundary-layer analysis was included in the viscous-inviscid scheme. In all cases considered, the internal displacement thickness was held constant at 0.01 times the nozzle exit radius which corresponds approximately to the value calculated by Yaros (ref. 5) for the internal configuration of Reubush's experiments (ref. 9). Typical external displacement thicknesses were about 20 times greater, and the mixing-layer calculation has been found to be insensitive to the nozzle boundary layer. (See ref. 12.)

RESULTS

Interactive Effects of Jet Entrainment

Effect on inviscid flow field.- In order to illustrate the interactive effects of entrainment and to demonstrate the validity of the jet entrainment model, the viscous-inviscid procedure was first applied to a simple example

problem. Consider a supersonic jet ($M_j = 2$) exhausting into a subsonic ($M_\infty = 0.4$) external stream with a boundary layer at the nozzle exit corresponding to a Reynolds number of about 1.2×10^7. (See fig. 10.) In the absence of viscous effects, the flow is assumed to be parallel to the axis and to have constant pressure everywhere. Thus, the inviscid plume boundary is simply a cylinder extending downstream from the nozzle exit. When the viscous-inviscid calculation is performed, the effective plume boundary is found to have a negative slope because of both the washing away of the boundary-layer defect and the acceleration of the external flow by the higher velocity jet. The inviscid external flow is influenced by this effective boundary a considerable distance upstream of the nozzle exit as shown by the pressure distribution along the afterbody. (See fig. 10.) Since most of the near-field effect is due to the streamline turning required to fill in the boundary-layer defect, this influence shows up as an expansion and recompression centered approximately at the nozzle exit location. For the nonparallel flows near nozzle boattails, a qualitatively similar effect can be expected to be superimposed onto the inviscid flow structure; that is, even though the external flow must be compressed as the flow approaches the end of the boattail, the effect of entrainment is to weaken this compression, thereby reducing the adverse pressure gradient over the boattail and increasing the boattail drag.

Since the pressure along the inviscid plume boundary is assumed to match that in the external flow, the pressure variations shown in figure 10 must also have an effect on the inviscid jet exhaust structure. This effect is illustrated by the pressure coefficient contours given in figure 11. The reduced pressures near the nozzle exit propagate downward into the jet exhaust creating a weak reflected shock pattern characteristic of mildly underexpanded plumes. Since for purely inviscid flow, the pressure is constant everywhere (i.e., $C_p = 0$), this structure is produced entirely by the interactive viscous effect.

Mass entrainment comparison.- The validity of the displacement concept can also be demonstrated from this example by comparing the mass entrained into the mixing layer in the inviscid solution with that calculated by the BOAT code. Such a comparison may be obtained by integrating the term $-\rho_e v_e r_e \, dx$ along the outer mixing-layer boundary to give the total mass entrained from the start of the mixing layer to a given axial distance downstream. The result of this calculation is shown in figure 12 where the viscous and inviscid results are seen to be in excellent agreement. Since v_e/u_e is proportional to the slope of the mass entrainment curve, this agreement also implies a matching of the radial velocity distribution (at least in an average sense over the distance corresponding to the inviscid grid size) and thus a matching of the streamline slopes along the mixing-layer boundary.

Effect of jet exhaust parameters.- As shown by Lighthill (ref. 24), the displacement effect of a boundary layer is equivalent to a source of strength proportional to $v_e r_e$. Based on the shear-layer—boundary-layer analogy given in appendix B of this paper, the term $v_e r_e$ can also be used to show the relative strength of the viscous-inviscid interaction of entrainment. Thus, a series of BOAT calculations were performed for the problem of figure 10 in which jet and free-stream conditions were systematically varied to simulate various engine exhaust conditions. In order to further isolate the basic effect

of mixing from external boundary-layer effects, these calculations were all performed with no initial boundary layers (i.e., fully developed velocity and density profiles were assumed at the nozzle exit). The calculated source strengths $v_e r_e / u_e r_j$ are shown in figure 13 for two values of the velocity ratio as a function of the mass-flow parameter $\rho_j u_j / \rho_\infty u_\infty$. (In the absence of initial boundary layers, the magnitude of $v_e r_e$ is found to be approximately constant over the region of interest in near-field interactions, i.e., $0 \lesssim x/r_j \lesssim 1$, and only the value at $x/r_j = 1$ has been plotted in the figure.)

The results shown in figure 13 can be summarized in the following statements:

$$\frac{v_e r_e}{u_e r_j} = 0 \quad \text{for} \quad \frac{\rho_j u_j}{\rho_\infty u_\infty} = 1$$

$$\frac{\partial (v_e r_e / u_e r_j)}{\partial (\rho_j u_j / \rho_\infty u_\infty)} < 0 \quad \text{for} \quad \frac{u_j}{u_\infty} = \text{Constant}$$

$$\frac{\partial |v_e r_e / u_e r_j|}{\partial (u_j / u_\infty)} > 0 \quad \text{for} \quad \frac{\rho_j u_j}{\rho_\infty u_\infty} = \text{Constant}$$

These statements suggest that the source strength behaves qualitatively as though

$$\frac{v_e r_e}{u_e r_j} \propto \frac{u_j}{u_\infty} \left(1 - \frac{\rho_j u_j}{\rho_\infty u_\infty} \right)$$

The cause of this behavior is made clear by examining the mass-flow profiles for different density ratios shown in figure 14. For density ratios such that $\rho_j u_j / \rho_\infty u_\infty < 1$ ($\rho_j / \rho_\infty = 1/14$ and $1/7$), the profile is "seen" by the external flow as a mass defect in the mixing layer which produces a positive (outward) displacement effect similar to that in a boundary layer. For density ratios such that $\rho_j u_j / \rho_\infty u_\infty > 1$ ($\rho_j / \rho_\infty = 1/2$ and 1), the profile is "seen" as a mass excess or negative displacement effect. Thus, while the magnitude of the entrainment interaction appears to depend mainly on the velocity gradient across the shear layer, the type of interaction (source or sink) depends on the mass-flow ratio. Since the magnitude of the entrainment effect on nozzle afterbody drag depends directly on the source strength, both density and velocity effects are expected to be important in the viscous-inviscid afterbody calculations.

Application of Interactive Model to Nozzle

Afterbody Flow Predictions

To demonstrate the sensitivities of the viscous-inviscid procedure to various model and flow-field parameters, calculations of the effective plume boundary and source strength distributions and afterbody pressure distributions were performed for a circular-arc boattail nozzle with $l/D = 1.768$ and $d_b/D = 0.51$. The jet was assumed to exhaust from a choked, convergent nozzle with exit conditions duplicating the cold-air experiments of reference 9. All calculations presented in this section are for a nozzle pressure ratio of 2.0 and a free-stream Mach number of 0.4 yielding a jet plume shape that is nearly fully expanded (essentially a cylinder).

Typical entrainment effect.- The effect of entrainment is shown in figures 15 and 16 by comparing the results obtained with the displacement effect of entrainment included with those obtained by treating the inviscid plume shape as a solid boundary. For the solid plume case, the boundary-layer calculation was continued over the plume in accordance with the local inviscid pressure gradient. The results show a significant reduction in the effective size of the plume when entrainment is allowed. (See fig. 15.) This reduction is mainly due to the elimination of the boundary-layer defect which with a solid plume boundary remains essentially constant over the distance shown. The effective non-dimensionalized source strength $v_{eff}r_{eff}/u_e r_j$ shows a corresponding reduction when entrainment is included. (The effective velocity v_{eff} is defined as $v_e r_e/r_{eff}$ such that $v_{eff} = u_e dr_{eff}/dx$.) The resulting afterbody pressure distribution (fig. 16) shows a significant reduction in the pressure near the end of the boattail because of the acceleration of the flow by the jet mixing. As shown in references 8 and 12, including this entrainment effect results in significantly better agreement with the experimental results of reference 9.

Boundary-layer effects.- By far the most important contribution to the entrainment effect results from the washing away of the external boundary-layer defect that is present at the nozzle exit. This effect is shown in figures 17 and 18 by comparing the results calculated with and without an external boundary layer. In the calculations without a boundary layer, the boundary-layer displacement effect was neglected over the entire body and the mixing analysis was initiated at the nozzle exit with a nearly discontinuous velocity profile characteristic of free shear layers. Significant differences are seen in the plume boundary shapes and are most evident in the source strength distribution (fig. 17). These results indicate clearly that the major contribution to the near-field source strength results from the transition of the wakelike boundary-layer defect to a free shear-layer type of behavior.

Pressure-gradient effects.- For nozzle afterbodies having significant closure, rather large axial pressure gradients can exist in the near-field mixing layer. These gradients are generally favorable in the usual boundary-layer sense in that they tend to inhibit the outward growth of the viscous layer.

However, in near-field mixing layers with initial boundary layers, such gradients tend to produce an undesired effect; that is, the pressure gradient accelerates the washing away of the boundary-layer defect yielding an increase in the mass entrained and a corresponding increase in the nozzle drag. The importance of including the pressure gradient in the jet entrainment calculation is shown in figures 19 and 20. The zero pressure-gradient results (dashed-line curve) were obtained by setting the pressure-gradient term in the axial momentum equation equal to zero only for the mixing solution. As shown in reference 8, this calculation gives almost the same displacement effect as the method of Yaros (ref. 5) which uses the isobaric mixing analysis of Korst and Chow (ref. 13). Significantly stronger (more negative) displacement effects are seen when the inviscid pressure gradients are included, thereby indicating an acceleration of the mixing process. Clearly, the assumption of isobaric mixing can lead to significant errors in the treatment of near-field mixing layers of nozzle boattails.

Effect of $d\rho_e u_e/dx$.- One assumption used to derive equation (7) (from which r_{eff} is calculated) is that the term involving $d\rho_e u_e/dx$ (see eq. (6)) is negligible compared with the source term due to entrainment. To test the validity of this assumption, calculations were performed in which r_{eff} was calculated from equation (6). A comparison of the results obtained with equations (6) and (7) is given in figures 21 and 22. These results indicate that in the near-field region the term $d\rho_e u_e/dx$ is not completely negligible although its contribution to the source strength is significantly smaller than the entrainment contribution. (See fig. 21.) Including this term also leads to a prediction of somewhat higher pressures near the end of the boattail. (See fig. 22.) However, recall that in both equations (6) and (7) the radial variation of $\rho_e u_e$ has been neglected. Since the effect on r_{eff} of including these radial variations in the equivalent inviscid properties is difficult to determine (requiring a solution to the integral differential eq. (4) or (5)), it is not evident that equation (6) is a better approximation; in fact, from an engineering standpoint, the use of equation (7) always gave slightly better agreement with experiment. Furthermore, the much larger axial grid size used for the inviscid calculation than that for the viscous calculation makes the numerical determination of the term $d\rho_e u_e/dx$ less accurate than the calculation of the mass entrainment term. Since the difference between results obtained with the two equations was always much smaller than the total entrainment effect, equation (7) has been used throughout the rest of this paper.

Effect of turbulence model.- One of the greatest uncertainties in most predictions involving turbulent flow is the modeling of the turbulence effects. In the overlaid mixing model of reference 10, these effects can be modeled with either a Prandtl mixing length (ML) or a two-equation (kε2) transport model of the turbulence quantities. Calculations were performed with each of these models, and the results are compared in figures 23 and 24. The ML model generally gave slightly larger predictions for the mixing rate yielding slightly more negative displacement effects. (See fig. 23.) Predictions with the ML model were also more sensitive to variations in the inviscid pressure gradients which resulted in oscillations in the source distribution. (See fig. 23 at $x/r_j \approx 8$.) This sensitivity to the pressure gradients resulted in the ML giving poor results at the higher pressure ratios. (See ref. 12.) Thus, the

kε2 model was selected as the base line turbulence model for the present calculations. At a pressure ratio of 2, both models gave about the same afterbody pressure predictions. (See fig. 24.)

Comparisons With Experimental Data

In order to validate the overall viscous-inviscid computational model, comparisons have been made with experimental results for which an extensive data base exists. These data consisted of the flow-field measurements of references 7 and 25 and afterbody pressure and drag measurements of reference 9. All data were obtained for the same circular-arc boattail with $l/D = 1.768$ and $d_b/D = 0.51$. The cold-air jet data were obtained with a choked, convergent nozzle; whereas the solid plume data were obtained with the jet simulated by a cylinder with a diameter equal to the nozzle exit diameter and extending about four nozzle exit diameters downstream.

Flow field.- A comparison between the predictions and measurements of the local flow angle and pressure distributions at various radial locations is shown in figure 25. The results are presented at the flow condition ($M_\infty = 0.6$, NPR = 2.9) for which the shear-layer velocity ratio is the greatest, and therefore entrainment effects are expected to be the most significant for any of the data available from reference 7. The agreement between the predicted and experimental results is very good everywhere except at the innermost radial location ($r/D = 0.36$). There the oscillations in flow properties produced by the wave-like structure of the inviscid plume boundary are not reproduced in the predicted result since the plume shape beyond the first inviscid cell is not accounted for in the calculation. Even so, the average calculated flow properties at the lower location agree well with the average measured properties, thereby indicating that any error associated with neglecting the multiple cell structure of the plume remains localized.

In assessing the predictions, note the relative location of the outer mixing-layer boundary. The two uppermost radial locations ($r/D = 0.99$ and 0.74) are well outside the calculated mixing-layer boundary, whereas the two lower locations ($r/D = 0.48$ and 0.36) are within the mixing layer (although not in a region of strong shear). Since the agreement is generally good in both regions, the overlaid mixing-layer concept seems well validated here.

In order to assess the accuracy of the calculations inside the full mixing layer, comparisons are made with the data of reference 25 and are shown in figure 26. These data consist of impact pressure measurements across the jet mixing layer at several axial locations. In figure 26(a) predicted results are presented for both the ML and kε2 turbulence models. The ML model is seen to provide much better agreement with experiment, although both models seem to underpredict the rate of spreading of the mixing layer. Fortunately, the interactive effect of entrainment appears to depend mainly on the rate of mass entrained per unit length which is about the same for both models even though the profiles are considerably different. The main difficulty with the kε2 model lies in the estimation of the initial turbulent kinetic-energy profile in the external boundary layer at the nozzle exit. Figure 26(b) shows a comparison

of the profiles predicted for two different initial turbulence levels. For one of the calculations (dashed-line curve), the initial turbulent kinetic energy and dissipation rate were increased by a factor of 4 over that used for the base line calculation. The results with the higher initial turbulence show a significant increase in the spreading of the mixing layer and actually over-predict this spreading compared with experiment. This sensitivity to the initial turbulence properties does not indicate a failure of the $k\varepsilon2$ model but, as pointed out in reference 26, simply indicates a need to know accurately these initial values. For the present calculations, the turbulence profiles were initialized from the calculated boundary-layer thickness by assuming a law-of-the-wall—law-of-the-wake form for the mean velocity profile. (See ref. 10 for details.) If the correct initial profiles were known, much better predictions for the downstream mixing behavior could probably be obtained. A more consistent approach would be to replace the integral-type boundary-layer solution with a finite-difference boundary-layer solution which modeled the turbulence in a manner consistent with the turbulent mixing solution. Thus the initial turbulent kinetic-energy profiles could be specified directly from the results of the boundary-layer solution.

Boattail pressures.- A comparison between predicted and measured afterbody pressure distributions is shown in figure 27 for various flow conditions. The first set of comparisons (fig. 27(a)) shows the effect of free-stream Mach number at a constant NPR which, since the jet velocity is essentially constant, also includes the effect of the shear-layer velocity ratio u_j/u_∞. The second set (fig. 27(b)) shows the effect of plume underexpansion or blockage (NPR) at a constant free-stream Mach number. The calculated pressure distribution on the effective plume boundary downstream of the nozzle exit is included to give an indication of the axial pressure gradients in the mixing layer. Increasing the shear-layer velocity gradient (and decreasing M_∞) weakens the pressure gradients over the afterbody and in the mixing layer, whereas the opposite effect is true for increasing the pressure ratio. For all flow conditions analyzed, the agreement between predicted and measured afterbody pressures is excellent with only a slight overprediction near the end of the boattails. The agreement is well within the estimated limits of experimental accuracy.

Boattail drag.- A comparison of the predicted and measured boattail drag coefficients obtained by integrating the pressure-coefficient distributions is given in figure 28. The calculated result with entrainment correctly predicts the relative variations with Mach number and pressure ratio and only slightly underpredicts the measured boattail drag. This slight underprediction of the drag is due almost entirely to the slight overprediction of the pressure at the end of the boattail and is typical of results obtained for circular-arc boat-tails which are extremely sensitive to small errors in the pressure distribution. (See ref. 2.) The predictions obtained by treating the inviscid plume boundary as a solid body are quite poor in comparison as are typically the results of models which do not account for local pressure gradients and non-similar turbulent mixing behavior.

Predictions of Real Gas Effects

Real gas effects occurring in actual aircraft jet exhausts are known to have a significant influence on nozzle afterbody drag. Attempts to correlate experimentally these effects with various jet and free-stream flow parameters over a wide range of conditions have been largely unsuccessful (e.g., see refs. 27 and 28). One of the main problems in finding adequate correlation parameters lies in the difficulty of isolating the effects of plume blockage and jet entrainment experimentally. With the present computational model, it is possible to isolate these effects in order to gain insight to the basic interaction mechanisms.

Based on the analysis used in deriving the interactive entrainment model, it is expected that real gas effects can be correlated through the manner in which the velocity and density profiles across the mixing layer are altered by changing the composition and temperature of the jet exhaust. (Changing the nozzle exit pressure produces effects due to both entrainment and blockage, and such simultaneous effects are not considered here.) In order to illustrate the predicted effects, a series of calculations were performed for the circular-arc boattail with $l/D = 1.768$ at $M_\infty = 0.4$ and NPR = 2.0. A constant nozzle exit Mach number of 1.0 was also assumed for all calculations. The velocity and density in the jet were varied by separately changing the gas composition and temperature at the nozzle exit. A third means considered for producing these variations is chemical reactions in the mixing layer.

Effect of gas composition.- The jet density was varied from that for a pure nitrogen jet to that for a pure hydrogen jet. This variation gave a density ratio ρ_j/ρ_∞ across the mixing layer of about 1 for nitrogen and about 1/14 for hydrogen. Intermediate density ratios were obtained by assuming various mixtures of the two gases. A comparison of the effective plume boundaries and source distributions for pure nitrogen and hydrogen jets is shown in figure 29. Decreasing the density of the jet is expected to give a blockage effect (positive displacement), whereas increasing the velocity should increase the magnitude of the displacement. Since the direction of the net change in displacement depends on the mass-flow ratio (which decreases for hydrogen), the hydrogen jet gives a net outward displacement of the effective plume boundary. This displacement results in a blockage-like effect which decreases the boattail drag in a manner similar to the effect of increasing the pressure ratio.

The variation in boattail drag with density is illustrated in figure 30 where $C_{D,\beta}$ is plotted as a function of the square root of the molecular weight ratio $\sqrt{W_\infty/W_j}$. This parameter was selected to allow direct comparisons with the experimental results of Peters (ref. 29) who found good correlation of boattail drag with $\sqrt{R_j}$. (For a constant jet temperature and Mach number, the mass-flow ratio $\rho_j u_j/\rho_\infty u_\infty$ is inversely proportional to $\sqrt{W_\infty/W_j} = \sqrt{R_j/R_\infty}$.) Peters' experiments were performed by using various mixtures of nitrogen and hydrogen with a boattail nozzle having an external shape very similar to that used for the present calculations. His results showed trends for the decrease in boat-

tail drag with increasing $\sqrt{R_j}$ similar to those shown here with increasing $\sqrt{W_\infty/W_j}$. The percentage decrease measured with hydrogen was about the same as that predicted here (≈ 50 percent). Thus, the predicted molecular weight (or density) effect seems well verified.

Effect of temperature.- For a constant jet gas composition and Mach number, the mass-flow ratio is proportional to $\sqrt{T_\infty/T_j}$. Thus, increasing the jet temperature decreases $\rho_j u_j / \rho_\infty u_\infty$ and should result in a blockage type of entrainment effect. For temperature ratios T_j/T_∞ up to about 5, this effect was found to be the case; that is, increasing the jet temperature pushed the effective plume boundary outward. (See fig. 31.) However, increasing the temperature ratio beyond 5 produced a change in the near-field behavior of the effective boundary because of an apparent increase in the rate at which the boundary-layer defect is removed. Thus, the initial slope of the effective boundary is much more negative at the higher temperature ($T_j/T_\infty = 6.75$ in fig. 31). This behavior is better illustrated by examining separately the near-field and far-field source strength variations with jet temperature shown in figure 32. The far-field source strength increases almost linearly with jet temperature, whereas the near-field source strength increases up to $T_j/T_\infty \approx 5$ and then decreases rapidly (becoming more sinklike) for $T_j/T_\infty > 5$. The near-field behavior appears to be caused by competition between the boundary-layer defect being washed away (negative source strength) and the density blockage effect. Thus, at sufficiently high temperatures the boundary-layer effect becomes dominant in the near field.

The resulting effect on the variation of the predicted boattail drag with jet temperature is shown in figure 33. Increasing the temperature ratio up to about 5 gives a decrease in the drag due to the density blockage effect, whereas increasing the temperature ratio above 5 gives an increase in drag. The predicted decrease in drag with increasing temperature is in qualitative agreement with the experimental results of references 27 and 28. However, the temperature range of these experiments did not extend beyond $T_j/T_\infty \approx 5$ and the predicted increase in drag at the higher temperature has not been validated. However, most aircraft exhausts operate at the lower temperatures where the interactive model does give the correct qualitative trends.

Effects of chemistry.- In view of the sensitivity of the entrainment effect to gas composition and temperature, a test case was chosen to illustrate the significance of the interactive effect for a more realistic jet exhaust condition. In addition to simulating a realistic exhaust temperature and composition, the effect of external afterburning of some "unburned fuel" was considered. Since any heat released from chemical reactions occurring in the near-field mixing layer could cause a significant increase in the local temperature, it was anticipated that chemistry could have a significant effect on the local mass entrainment rate.

The exhaust composition assumed for these calculations is shown in table I. The species listed are typical of the combustion products of a hydrocarbon fuel. However, in order to provide a relatively simple mechanism for the chemical reactions, it has been assumed that most of the carbon is present as CO rather

than CO_2 as it would be if the primary combustion were complete. The CO thus represents the unburned fuel for the external afterburning. While the relative amounts of CO and CO_2 listed in table I do not represent any known engine, the total mole fraction of CO and CO_2 are reasonable for a turbojet engine operating in an afterburning model. Thus, the assumed mole fraction of CO (10 percent) is probably an upper limit for such an engine. The reaction scheme used for the CO afterburning case is given in table II. Viscous-inviscid interaction calculations were performed at $M_\infty = 0.4$ and NPR = 2.0 for this exhaust composition both with and without external reactions allowed. A jet temperature of 1500 K and a nominal γ of 1.27 were assumed for the inviscid jet calculation. These results were then compared with those for a cold-air jet ($T_j = 243$ K and $\gamma = 1.4$).

A comparison of the calculated radial distributions in velocity, temperature, and mass flux at an axial location of $x/r_j = 12$ is given in figure 34. The primary effect of increasing the temperature is to increase the velocity ratio while decreasing the mass-flux ratio. For the case with CO afterburning, the heat released produces a significant bulge in the temperature profile with a further decrease in mass flux. The resulting effective plume boundaries and source distributions are shown in figure 35. The effect of chemistry is just an additional outward shift in the plume boundary because of the increase in temperature (and decreased density). The shift does not become significant until several jet radii downstream since no significant burning of the CO takes place until sufficient mixing has occurred with the external airstream. The outward displacement effect of combustion has been described by others (see refs. 30 and 31), and effective body techniques have been used previously to represent the streamline deflections induced by combustion in a supersonic jet. (See ref. 31.)

A comparison of the calculated boattail drag for these cases is shown in figure 36. The drag calculated for the hot jet without afterburning is less than 60 percent of that for cold air. This decrease in drag is almost entirely due to the increased temperature since a separate calculation for a hot-air jet showed essentially no effect due to composition (different γ). (Note that the temperature effect shown here is opposite to that given in ref. 8 because of an error in the effective body calculations of ref. 8 for the hot jet cases.) An additional decrease in drag of slightly more than 10 percent is seen when the effects of CO afterburning are included. The main reason that the afterburning effect is much smaller than the temperature effect alone is that most of the burning takes place too far downstream of the nozzle exit to have a significant effect on the boattail. However, the afterburning effect shown here is not negligible. Furthermore, note that the type of mixing-layer chemical reactions considered here represents a rather mild form of afterburning; for example, the temperature rise frequently seen in the mixing layers of afterburning rocket plumes can be many times greater than that obtained here. The treatment of strongly afterburning plumes would require a more fully coupled treatment between the inviscid, viscous, and thermochemical processes than the approximate overlaid procedure used here. Thus, the sensitivity of the afterbody flow to thermochemical processes shown by these results indicates a need for further studies of real gas effects in exhaust jet and external flow interactions.

CONCLUDING REMARKS

A viscous-inviscid interaction model has been developed to account for jet entrainment effects in the prediction of the subsonic flow over nozzle after-bodies. The model has been combined with an inviscid external flow solution, an external boundary-layer solution, and an inviscid jet exhaust solution to provide an iterative technique for determining the afterbody-exhaust jet interaction effects. An analysis of the interaction model and applications of the iterative technique have provided the following results:

1. The streamline deflections associated with jet entrainment can be accounted for by performing an inviscid calculation over an effective jet plume boundary that is properly displaced from the inviscid plume boundary. An approximate technique has been developed for calculating the shape of the effective boundary based on the results of a numerical solution for the viscous mixing layer. For weakly interacting shear layers, excellent matching of the calculated mass entrainment was obtained between the viscous and inviscid solutions.

2. For small streamline deflections, the effective plume boundary shape can be represented by an equivalent source distribution, the local strength of which is directly proportional to the local mass entrainment rate at the outer edge of the mixing layer. The source strength was found to vary in a manner which suggests that the basic character of the entrainment interaction is governed by the shear-layer velocity ratio and the mass-flux ratio.

3. For nozzle afterbodies with relatively thick external boundary layers, the jet entrainment effect appears to result mainly from the washing away of the low-velocity mass defect. This washing away was found to be greatly accelerated by the favorable pressure gradients that typically exist in near-field mixing layers.

4. The validity of the overlaid viscous-inviscid approach has been demonstrated by comparisons with experimental flow-field data for circular-arc boattail nozzles. While some discrepancies exist between predicted and experimental results inside the viscous mixing region, the mean flow properties are adequately predicted, and excellent agreement is obtained for the external inviscid flow structure.

5. The inclusion of jet entrainment effects significantly improves the prediction of nozzle boattail drag over that obtained by treating the inviscid plume boundary as an effective solid body. The predicted variations in boattail drag with free-stream Mach number and nozzle pressure ratio are in good agreement with experiment.

6. The predicted variation in boattail drag with jet gas composition and temperature is in qualitative agreement with experimental data. The drag is found to decrease with either a decrease in the jet molecular weight or an increase in jet temperature (decreasing the shear-layer mass-flux ratio in both cases) except at very high temperatures (>1500 K) where the predicted drag

appears to reach a minimum and then increases with further increases in temperature. This high-temperature behavior was not evident in any of the experimental data examined. However, the temperature at which the minimum drag occurs is expected to be very problem dependent since it is related to the washing away of the external boundary layer and not to any fundamental entrainment mechanism.

7. Results predicted for the effects of external afterburning indicate a possible sensitivity to the heat released from chemical reactions in the mixing layer. For the case considered, a reduction in boattail drag of about 10 percent was produced by the afterburning associated with a jet having a 10-percent mole fraction of carbon monoxide. While such predictions remain to be validated by appropriate experiments, further studies of thermochemical effects on nozzle afterbody flows as well as further improvements in computational techniques for treating such flows appear to be warranted.

Langley Research Center
National Aeronautics and Space Administration
Hampton, VA 23665
February 8, 1980

APPENDIX A

INCOMPRESSIBLE SHEAR-LAYER MODEL FOR

STREAMLINE CALCULATIONS

The following shear-layer model is intended only to provide a qualitative description of the variation of the external streamline patterns as a function of the velocity ratio across the shear layer. The qualitative behavior of this model was verified by limited comparisons with the results calculated by the more exact shear-layer model of reference 10 for similar test cases.

Consider the incompressible flow of an axisymmetric jet with velocity u_j exhausting from a nozzle with radius r_j into a stream with velocity u_e and assume a fully developed, turbulent shear layer. A reasonable representation of the velocity profile across the region $0 \leqq r < \infty$ is given by

$$u = \begin{cases} u_j & (0 \leqq r < r_1) \\ u_j + (u_e - u_j)(3\eta^2 - 2\eta^3) & (r_1 \leqq r < r_2) \\ u_e & (r_2 \leqq r < \infty) \end{cases} \qquad (A1)$$

where $\eta = (r - r_1)/l$, $l = (r_2 - r_1)$, and r_1 and r_2 are the inner and outer boundaries, respectively, of the shear layer. Define a nondimensional, incompressible stream function $\bar{\psi} = \psi/\psi_j$ where $\psi_j = \sqrt{\rho_j u_j r_j^2}$. By using the stream-function definition given by equation (1), the variation of $\bar{\psi}$ across the region is then

$$\bar{\psi} = \begin{cases} \bar{r} & (0 \leqq \bar{r} < \bar{r}_1) \\ \left[\bar{r}_1^2 + 2\bar{r}_1\bar{l}I_1(\eta) + \bar{l}^2 I_2(\eta) \right]^{1/2} & (\bar{r}_1 \leqq \bar{r} < \bar{r}_2) \\ \Big[\bar{r}_1^2 + 2\bar{r}_1\bar{l}I_1(1) + \bar{l}^2 I_2(1) \\ \qquad + \dfrac{u_e}{u_j}\big(\bar{r}^2 - \bar{r}_2^2\big) \Big]^{1/2} & (\bar{r}_2 \leqq \bar{r} < \infty) \end{cases} \qquad (A2)$$

where

$$I_1(\eta) = \eta + \left(\frac{u_e}{u_j} - 1\right)\left(\eta^3 - \frac{1}{2}\eta^4\right) \tag{A3}$$

$$I_2(\eta) = \eta^2 + \left(\frac{u_e}{u_j} - 1\right)\left(\frac{3}{2}\eta^4 - \frac{4}{5}\eta^5\right) \tag{A4}$$

and $\bar{r}$ and $\bar{l}$ denote values nondimensionalized by r_j. For given values of u_j/u_e, $\bar{r}_1$ and $\bar{l}$, equation (A2) can be solved numerically to obtain the streamline location $\bar{r}(\psi)$.

The axial variation of $\bar{\psi}$ in equation (A2) is contained implicitly in $\bar{r}_1$ and $\bar{l}$, both of which depend on the distance $\bar{x}$ from the nozzle exit. The lower boundary $\bar{r}_1(\bar{x})$ is determined by applying the approximate rule governing the mass entrained at the shear-layer edge given by (ref. 10)

$$\bar{\psi}_1 \frac{\partial \bar{\psi}_1}{\partial x} \approx \bar{r}_1 \lim_{u_{\bar{r}} \to 0} \frac{\left(\mu \bar{r} u_{\bar{r}}\right)_{\bar{r}}}{\bar{r} u_{\bar{r}}} \tag{A5}$$

where μ is the turbulent viscosity and the subscript $\bar{r}$ denotes differentiation with respect to $\bar{r}$. By assuming a Prandtl mixing-length relation

$$\mu = \rho l_m^2 \left|\frac{\partial u}{\partial r}\right| \tag{A6}$$

to hold, by noting that $\bar{\psi}_1 = \bar{r}_1$, and by using equations (A1), (A5), and (A6), the following relation for $\bar{r}_1(\bar{x})$ is obtained:

$$\bar{r}_1(\bar{x}) = 1 - 12\left(\frac{\bar{l}_m}{\bar{l}}\right)^2 \left|1 - \frac{u_e}{u_j}\right|\bar{x} \tag{A7}$$

In evaluating equation (A7) for use in equation (A2), a value for the length scale $\bar{l}_m/\bar{l}$ of 0.065 (based on the recommendation of ref. 10 for near-field shear layers) is used.

APPENDIX A

The spread rate of the shear layer (which determines $\bar{l}$) was obtained by using

$$\sigma = \sigma_0 \left| \frac{1 + \dfrac{u_e}{u_j}}{1 - \dfrac{u_e}{u_j}} \right| \tag{A8}$$

as recommended in reference 32, with $\sigma_0 = 12$. The spread rate is defined by

$$\sigma \equiv \frac{1.855 \, \Delta\bar{x}}{(\Delta\bar{y})_{0.1\to0.9}} \tag{A9}$$

where $(\Delta\bar{y})_{0.1\to0.9}$ is the change in the shear-layer width over the distance Δx; the width is defined as the radial distance between points where $(u - u_e)/(u_j - u_e) = 0.1$ and 0.9. For the velocity profile given by equation (A1), equation (A9) gives the following relation for $l(\bar{x})$:

$$\bar{l}(\bar{x}) \approx \frac{3.049\bar{x}}{\sigma} \tag{A10}$$

Equations (A2), (A7), and (A10) were solved for $1 \leqq \bar{\psi} \leqq 20$ and $0 \leqq \bar{x} \leqq 10$ in increments $\Delta\bar{\psi} = 1$, where $\bar{\psi} = 1$ is the jet dividing streamline, to produce the streamline patterns given in figure 4.

ANALOGY BETWEEN DISPLACEMENT THICKNESSES

FOR SHEAR LAYERS AND BOUNDARY LAYERS

By combining equations (3) and (4) with the assumptions that $\rho_e v_e = \rho_e^I v_e^I$ and that $\rho_e u_e = \rho^I u^I$ and does not vary significantly with r

$$\int_{r_{eff}}^{r_e} \frac{\partial \rho_e u_e}{\partial x} r \, dr = \int_0^{r_e} \frac{\partial \rho u}{\partial x} r \, dr + \rho_{eff} v_{eff} r_{eff} \tag{B1}$$

By subtracting the term $\displaystyle\int_0^{r_e} \frac{\partial \rho_e u_e}{\partial x} r \, dr$ from both sides of equation (B1), by applying Liebnitz' formula to the integrals, and by using the tangency condition $v_{eff} = u_{eff} \dfrac{dr_{eff}}{dx}$

$$\frac{d}{dx}\left(\frac{1}{2} \rho_e u_e r_{eff}^2\right) = \frac{d}{dx}\left[\rho_e u_e \int_0^{r_e} \left(1 - \frac{\rho u}{\rho_e u_e}\right) r \, dr\right] \tag{B2}$$

This equation can readily be integrated to give

$$r_{eff}^2 = 2 \int_0^{r_e} \left(1 - \frac{\rho u}{\rho_e u_e}\right) r \, dr + C \tag{B3}$$

where C is an arbitrary constant.

Now define $\delta_{eff}^* = r_{eff} - r_j$ and assume that $\delta_{eff}^* \ll r_j$, that is, a thin shear layer. (This assumption is not necessary to evaluate δ_{eff}^* but is simply used to make the boundary-layer analogy clearer.) Then $r_{eff}^2 \approx r_j^2 + 2r_j \delta_{eff}^*$ (to a first-order approximation) and equation (B3) gives

$$\delta_{eff}^* \approx \frac{1}{r_j} \int_0^{r_e} \left(1 - \frac{\rho u}{\rho_e u_e}\right) r \, dr - r_j + C \tag{B4}$$

The integration constant C could now be determined by the initial conditions at the nozzle exit; for example, $\delta_{eff}^* = 0$ at $x = 0$ without an initial

boundary layer or $\delta^*_{eff} = \delta^*_{bl}$ at $x = 0$ with an initial boundary layer. Assuming an inviscid, irrotational external flow, the displacement effect is equivalent to a source of strength given by

$$v_e r_e \approx \frac{1}{\rho_e} \frac{d}{dx}\left(\rho_e u_e r_j \delta^*_{eff}\right) \tag{B5}$$

(See ref. 24 for a discussion of the equivalence between source strength and displacement effects.) Thus, the viscous-inviscid interaction depends only on the axial rate of change of δ^*_{eff}, and the integration constant is unimportant.

The analogy with the displacement thickness for a boundary layer is immediately made evident by applying a similar approach to a thin axisymmetric boundary layer. The analogous expression for the boundary-layer displacement thickness over a body of radius r_B can be readily shown to be

$$\delta^*_{bl} = \frac{1}{r_B} \int_{r_B}^{r_e} \left(1 - \frac{\rho u}{\rho_e u_e}\right) r \, dr + C \tag{B6}$$

and the source strength to be

$$v_e r_e = \frac{1}{\rho_e} \frac{d}{dx}\left(\rho_e u_e r_B \delta^*_{bl}\right) \tag{B7}$$

The only significant difference between equations (B4) and (B6) is the lower limit of integration. For the shear layer, this lower limit must extend to the axis to account properly for the blockage effect of the jet exhaust flow, whereas for a solid body, the lower limit is just the body radius. For the special case where the jet exhaust is fully expanded and $\rho_j u_j$ is constant in the inviscid core $0 \leq r \leq r_i$, the integration can be performed over the core and equation (B4) becomes

$$\delta^*_{eff} = \frac{1}{r_j} \int_{r_i}^{r_e} \left(1 - \frac{\rho u}{\rho_e u_e}\right) r \, dr + \frac{1}{2}\left(1 - \frac{\rho_j u_j}{\rho_e u_e}\right)\frac{r_i^2}{r_j} - r_j + C \tag{B8}$$

The analogy between the integrals in equations (B6) and (B8) is then clearer since both extend only over the viscous region. The main difference is that where δ^*_{bl} always represents a mass defect and is therefore positive, δ^*_{eff} can represent either a defect or an excess depending upon the parameter $\rho_j u_j / \rho_e u_e$. (The effect of the mass-flow ratio on the shear-layer source strength is discussed in the main text.)

In order to demonstrate that the effective plume boundary defined by equation (B3) contains the inviscid blockage effect, consider the inviscid limit of this expression. First evaluate C at $x = 0$ where $r_{eff} = r_j$ (if no external boundary layer exists). Then

$$r_{eff}^2 = \frac{2\dot{m}_j}{\rho_e u_e} + 2 \int_0^{r_e} \left(1 - \frac{\rho u}{\rho_e u_e}\right) r \, dr \tag{B9}$$

where $\dot{m}_j$ is the jet mass flow $\left(\dot{m}_j = \frac{1}{2} \rho_j u_j r_j^2 \text{ for uniform flow}\right)$. Note that $\int_0^{r_e} \rho u r \, dr = \dot{m}_j + \dot{m}_{ent}$; thus,

$$r_{eff}^2 = r_e^2 - \frac{2\dot{m}_{ent}}{\rho_e u_e} \tag{B10}$$

But in the inviscid limit, $\dot{m}_{ent} \to 0$ and $r_e = \lim_{\delta \to 0}\left(r_j^I + \delta\right) = r_j^I$ where δ is proportional to the width of the shear layer and r_j^I is the inviscid plume boundary.

REFERENCES

1. Reubush, David E.; and Putnam, Lawrence E.: An Experimental and Analytical Investigation of the Effect on Isolated Boattail Drag of Varying Reynolds Number up to 130×10^6. NASA TN D-8210, 1976.

2. Wilmoth, Richard G.: Computation of Transonic Boattail Flow With Separation. NASA TP-1070, 1977.

3. Cosner, Raymond R.; and Bower, William W.: A Patched Solution of the Transonic Flowfield About an Axisymmetric Boattail. AIAA Paper 77-227, Jan. 1977.

4. Yaeger, L. S.: Transonic Flow Over Afterbodies Including the Effects of Jet-Plume and Viscous Interactions With Separation. AIAA Paper 77-228, Jan. 1977.

5. Yaros, Steven F.: An Analysis of Transonic Viscous/Inviscid Interactions on Axisymmetric Bodies With Solid Stings or Real Plumes. AEDC-TR-77-106, U.S. Air Force, Feb. 1978. (Available from DTIC as AD A050 401.)

6. Bergman, Dave: Effects of Engine Exhaust Flow on Boattail Drag. AIAA Paper 70-132, Jan. 1970.

7. Putnam, Lawrence E.; and Abeyounis, William K.: Experimental and Theoretical Study of Flow Fields Surrounding Boattail Nozzles at Subsonic Speeds. AIAA Paper No. 76-675, July 1976.

8. Wilmoth, R. G.; Dash, S. M.; and Pergament, H. S.: A Numerical Study of Jet Entrainment Effects on the Subsonic Flow Over Nozzle Afterbodies. AIAA Paper 79-0135, Jan. 1979.

9. Reubush, David E.: Experimental Study of the Effectiveness of Cylindrical Plume Simulators for Predicting Jet-On Boattail Drag at Mach Numbers up to 1.30. NASA TN D-7795, 1974.

10. Dash, Sanford M.; and Pergament, Harold S.: A Computational Model for the Prediction of Jet Entrainment in the Vicinity of Nozzle Boattails (The BOAT Code). NASA CR-3075, 1978.

11. Dash, S. M.; and Thorpe, R. D.: A New Shock-Capturing/Shock-Fitting Computational Model for Analyzing Supersonic Inviscid Flows (The SCIPPY Code). Rep. No. 366, Aeronaut. Res. Assoc. Princeton, Inc., Nov. 1978.

12. Dash, S. M.; Wilmoth, R. G.; and Pergament, H. S.: Overlaid Viscous/ Inviscid Model for the Prediction of Near-Field Jet Entrainment. AIAA J., vol. 17, no. 9, Sept. 1979, pp. 950-958.

13. Korst, H. H.; and Chow, W. L.: Non-Isoenergetic Turbulent ($Pr_t = 1$) Jet Mixing Between Two Compressible Streams at Constant Pressure. NASA CR-419, 1966.

14. Dash, S. M.; and Pergament, H. S.: The Analysis of Low Altitude Rocket and Aircraft Plume Flowfields: Modelling Requirements and Procedures. JANNAF 10th Plume Technology Meeting, Volume 1. CPIA Publ. 291 (Contract N00017-72-C-4401), Appl. Phys. Lab., Johns Hopkins Univ., Dec. 1977, pp. 53-131. (Available from DTIC as AD B025 704.)

15. Burggraf, Odus R.: Choice of Boundary Conditions in Viscous Interaction Theory. AIAA J., vol. 4, no. 6, June 1966, pp. 1145-1146.

16. South, Jerry C., Jr.; and Jameson, Antony: Relaxation Solutions for Inviscid Axisymmetric Transonic Flow Over Blunt or Pointed Bodies. AIAA Computational Fluid Dynamics Conference, July 1973, pp. 8-17.

17. Keller, James D.; and South, Jerry C., Jr.: RAXBOD: A FORTRAN Program for Inviscid Transonic Flow Over Axisymmetric Bodies. NASA TM X-72831, 1976.

18. Reshotko, Eli; and Tucker, Maurice: Approximate Calculation of the Compressible Turbulent Boundary Layer With Heat Transfer and Arbitrary Pressure Gradient. NACA TN 4154, 1957.

19. Users Manual for the External Drag and Internal Nozzle Performance Deck (Deck XI) - Supersonic Flow Analysis (Applicable to Deck VI). PWA-3465, Suppl. F, Pt. I (Contract No. AF33(615)-3128), Pratt & Whitney Aircraft, Sept. 1, 1968.

20. Salas, Manuel D.: The Numerical Calculation of Inviscid Plume Flow Fields. AIAA Paper No. 74-523, June 1974.

21. Patankar, S. V.; and Spalding, D. B.: Heat and Mass Transfer in Boundary Layers. Second ed. Int. Textbook Co. Ltd. (London), c.1970.

22. Launder, B. E.; Morse, A.; Rodi, W.; and Spalding, D. B.: Prediction of Free Shear Flows - A Comparison of the Performance of Six Turbulence Models. Free Turbulent Shear Flows. Volume I - Conference Proceedings, NASA SP-321, 1973, pp. 361-426.

23. Mikatarian, R. R.; Kau, C. J.; and Pergament, H. S.: A Fast Computer Program for Nonequilibrium Rocket Plume Predictions. AFRPL-TR-72-94, U.S. Air Force, Aug. 1972. (Available from DTIC as AD 751 984.)

24. Lighthill, M. J.: On Displacement Thickness. J. Fluid Mech., vol. 4, pt. 4, Aug. 1958, pp. 383-392.

25. Mason, Mary L.; and Putnam, Lawrence E.: Pitot Pressure Measurements in Flow Fields Behind Circular-Arc Nozzles With Exhaust Jets at Subsonic Free-Stream Mach Numbers. NASA TM-80169, 1979.

26. Pergament, H. S.; Dash, S. M.; and Varma, A. K.: Evaluation of Turbulence Models for Rocket and Aircraft Plume Flowfield Predictions. Rep. 370-I, Aeronaut. Res. Assoc. Princeton, Inc., Feb. 1979. (Available from DTIC as AD A068 388.)

27. Compton, William B., III: Effects of Jet Exhaust Gas Properties on Exhaust Simulation and Afterbody Drag. NASA TR R-444, 1975.

28. Peters, W. L.; and Kennedy, T. L.: An Evaluation of Jet Simulation Parameters for Nozzle/Afterbody Testing at Transonic Mach Numbers. AIAA Paper 77-106, Jan. 1977.

29. Peters, W. L.: Jet Simulation Techniques: Simulation of Temperature Effects By Altering Gas Composition. AEDC-TR-78-43, U.S. Air Force, Mar. 1979. (Available from DTIC as AD A067 084.)

30. Ferri, Antonio: Mixing-Controlled Supersonic Combustion. Annual Review of Fluid Mechanics, Volume 5, Van Dyke, Milton, Vincente, Walter G., and Wehausen, J. V., eds. of Vol. 5, Annu. Rev., Inc., 1973, pp. 301-338.

31. Anderson, Griffin Y.; Agnone, Anthony M.; and Russin, Wm. Roger: Composition Distribution and Equivalent Body Shape for a Reacting, Coaxial, Supersonic Hydrogen-Air Flow. NASA TN D-6123, 1971.

32. Free Turbulent Shear Flows. Vol. I - Conference Proceedings. NASA SP-321, 1973.

TABLE I.- ASSUMED EXHAUST COMPOSITION FOR

AFTERBURNING TURBOJET ENGINE

$$[W = 27.225]$$

Species	Mole fraction
N_2	0.75
O_2	.05
CO_2	.0001
H_2O	.1
CO	.1
OH	.001
H	.001
O	.000001
H_2	.0001

TABLE II.- CO AFTERBURNING REACTIONS

Reaction	Rate coefficient, molecule-cm-sec units
(1) $CO + OH \rightarrow CO_2 + H$	$1.1 \times 10^{-19}T^2 \exp(1600/RT)$
(2) $CO + O + M \rightarrow CO_2 + M$	$1.0 \times 10^{-32} \exp(-4000/RT)$
(3) $H + OH + M \rightarrow H_2O + M$	$1.0 \times 10^{-25}T^{-2}$
(4) $O + H + M \rightarrow OH + M$	3.0×10^{-32}
(5) $O + O + M \rightarrow O_2 + M$	$5.0 \times 10^{-30}T^{-1} \exp(-340/RT)$
(6) $H + H + M \rightarrow H_2 + M$	$5.0 \times 10^{-30}T^{-1}$
(7) $OH + H \rightarrow H_2 + O$	$1.4 \times 10^{-14}T \exp(-7000/RT)$
(8) $OH + O \rightarrow H + O_2$	4.0×10^{-11}
(9) $OH + H_2 \rightarrow H_2O + H$	$1.0 \times 10^{-17}T^2 \exp(-2900/RT)$
(10) $OH + OH \rightarrow H_2O + O$	$1.0 \times 10^{-11} \exp(-1100/RT)$
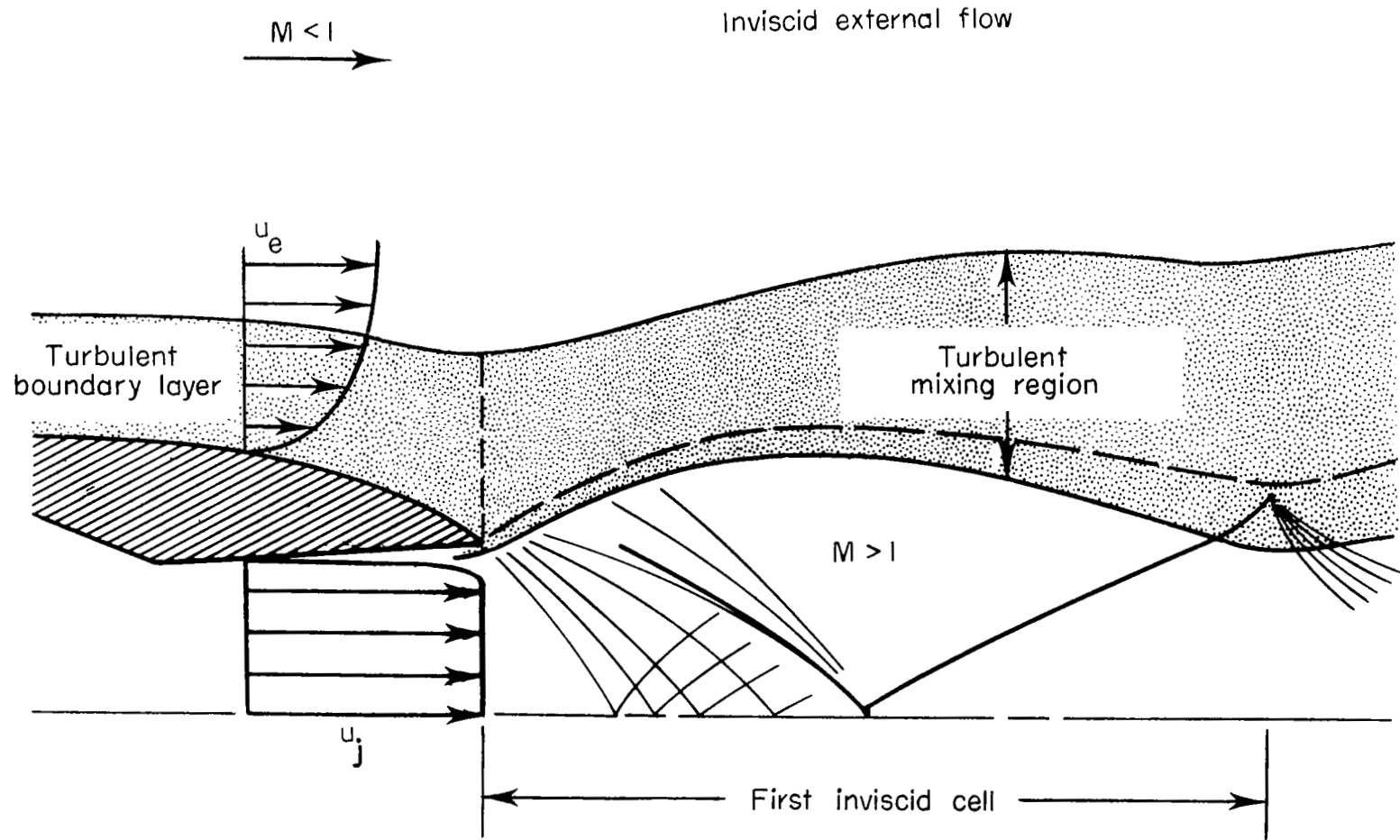
Figure 1.- Schematic of nozzle afterbody flow field.
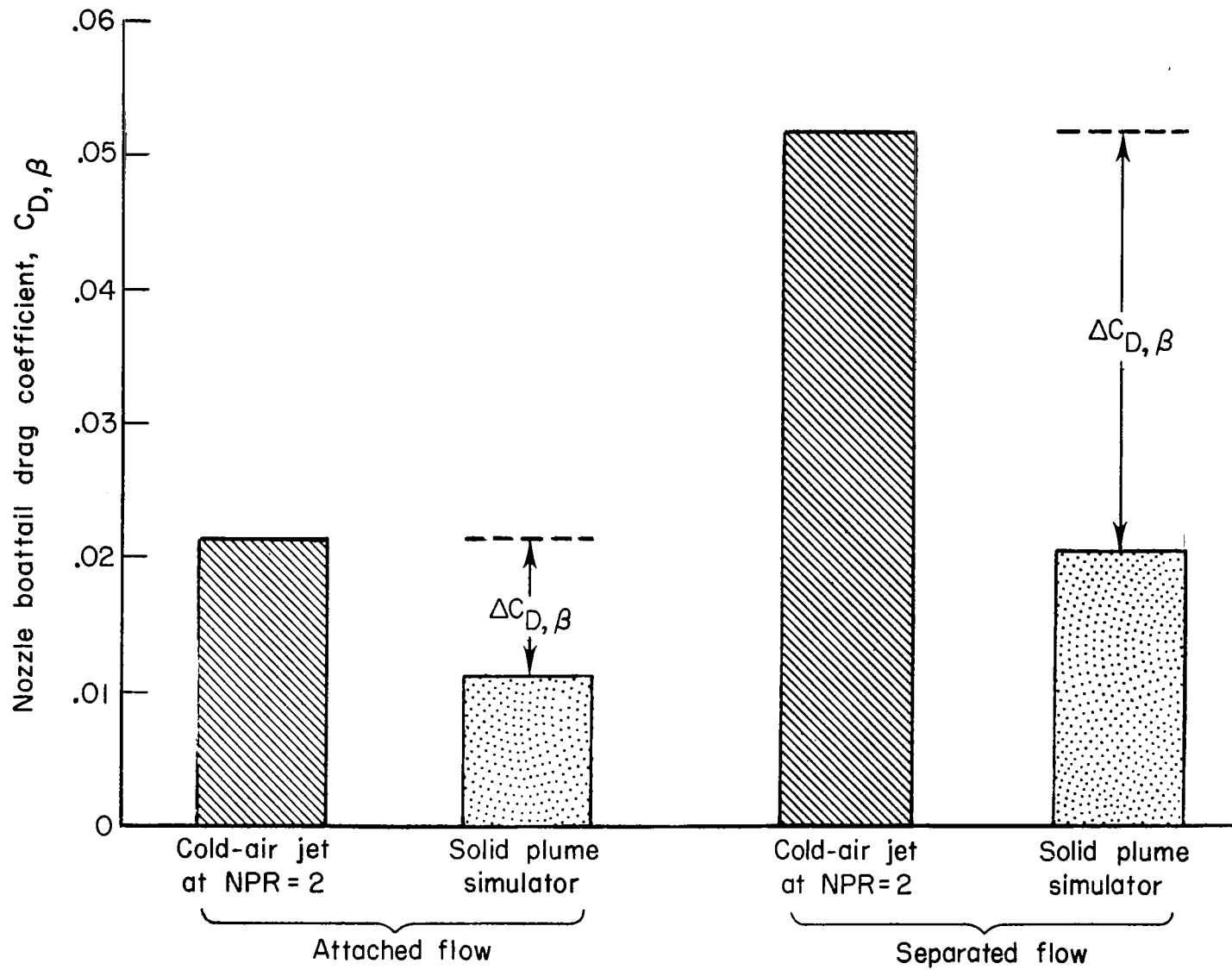
Figure 2.- Typical entrainment effect on nozzle boattail drag determined
from experiment. Data from reference 9; $M_\infty = 0.4$.
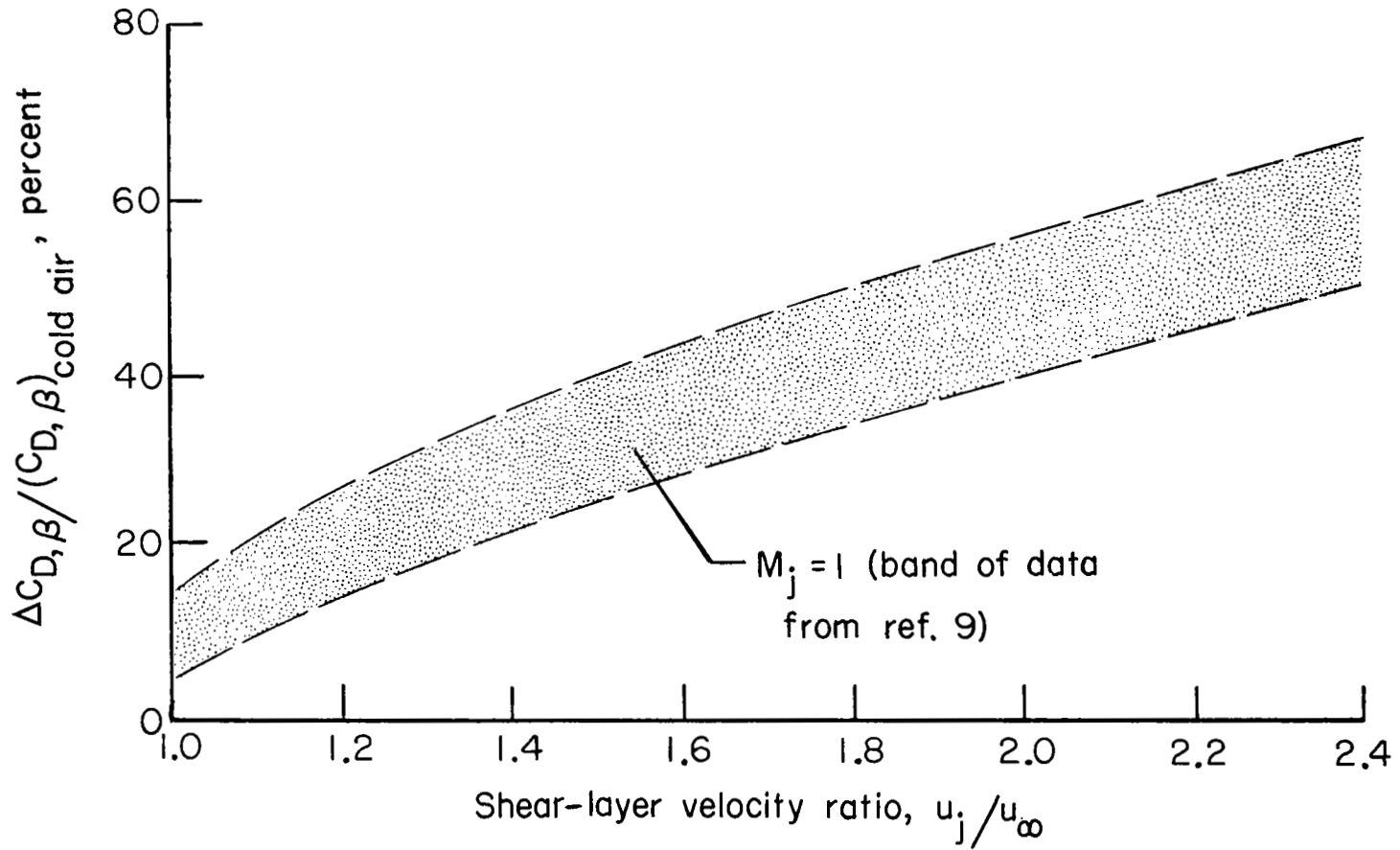
Figure 3.- Correlation of measured drag increment due to entrainment with
shear-layer velocity ratio.
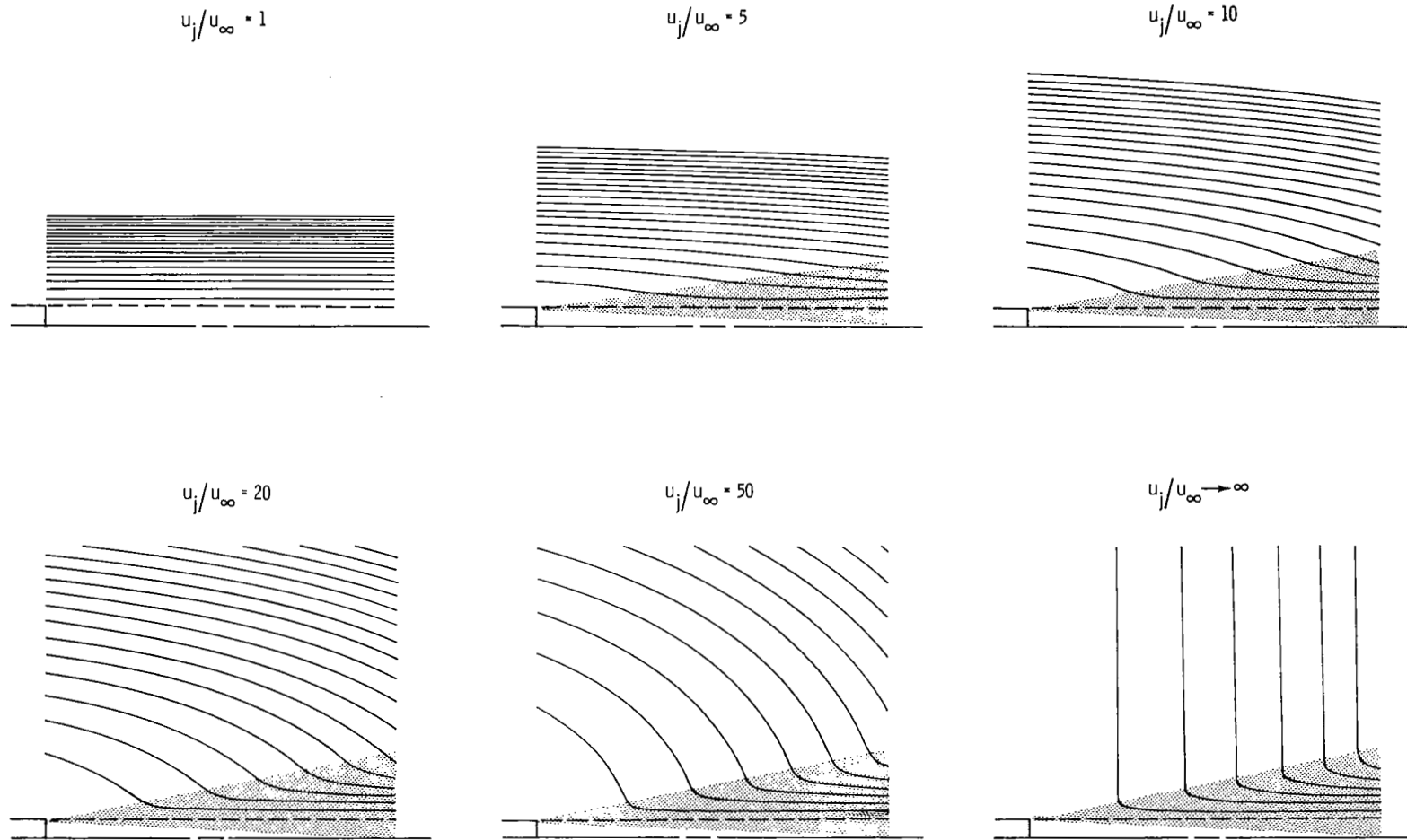
Figure 4.- Streamline patterns produced by entrainment at various velocity ratios. Incompressible flow; $p_j = p_\infty$; $\Delta\psi = \psi_j$. Dashed line indicates ψ_j and shaded area indicates assumed mixing region.
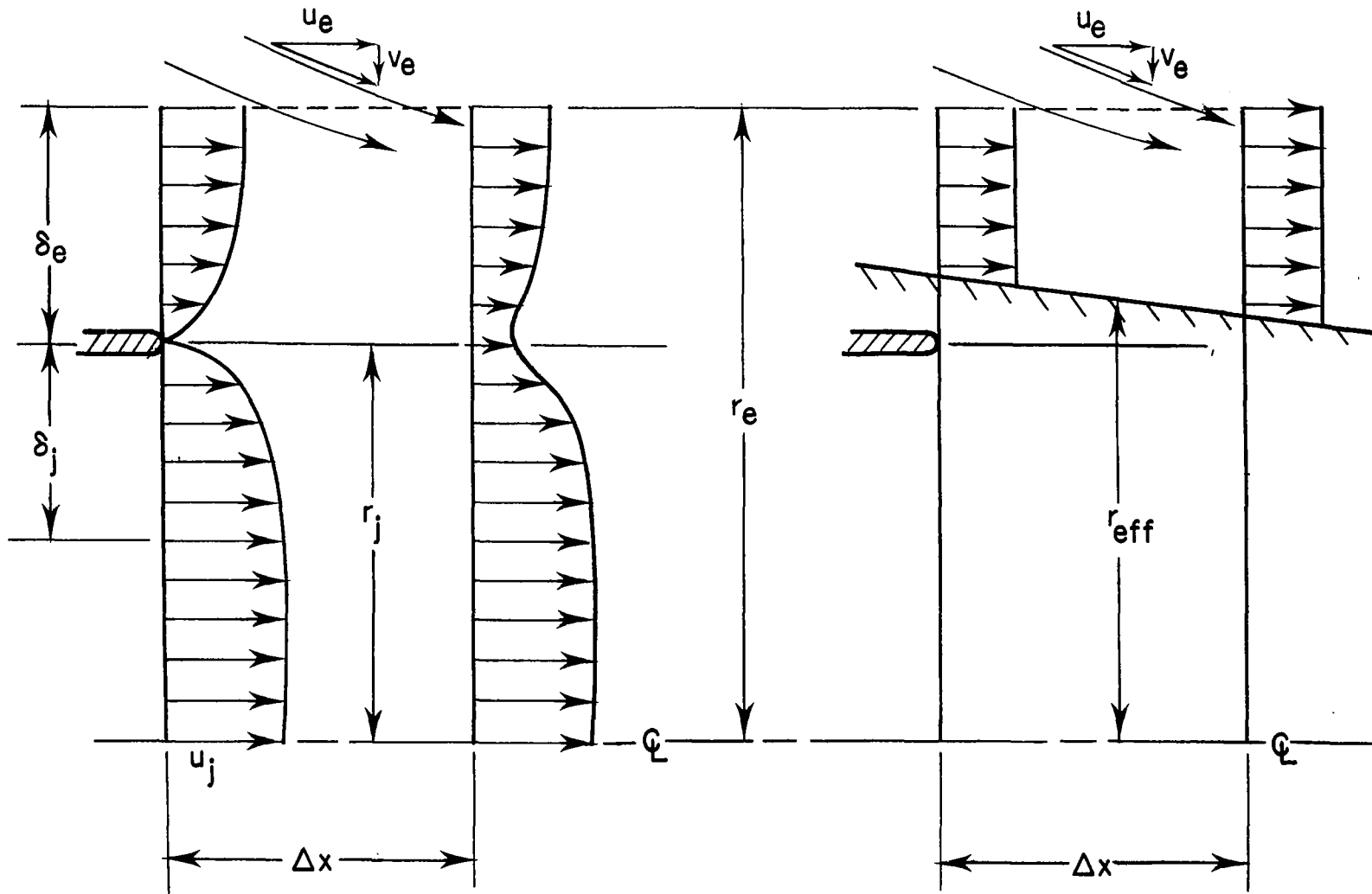
(a) Control volume for
viscous flow.

(b) Control volume for equivalent
inviscid flow.

Figure 5.- Control volume for effective plume boundary definition.
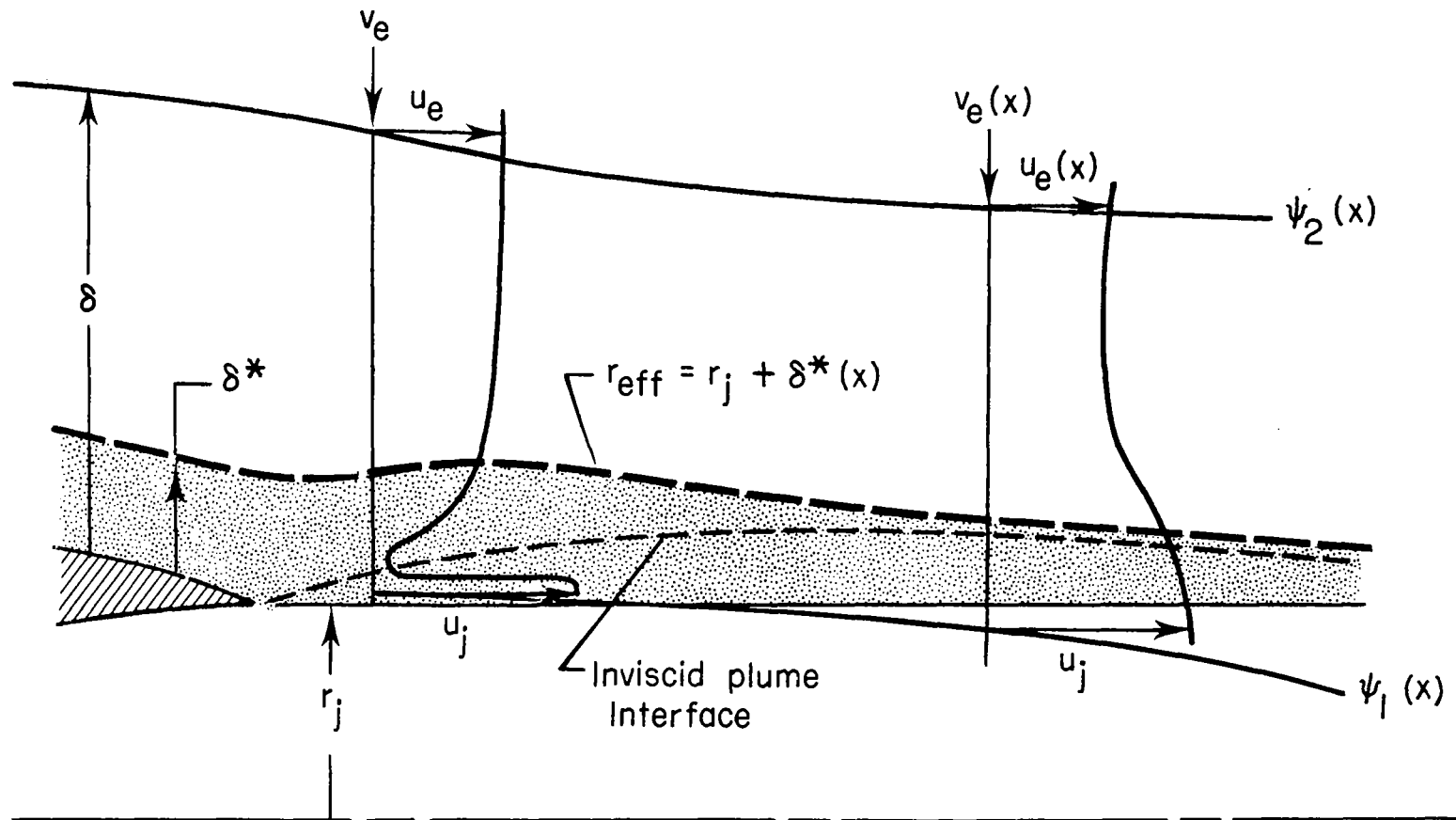
Figure 6.- Application of effective plume boundary as equivalent
displacement-thickness correction.

START → Input body geometry and flow conditions → Set uniform initial external flow, i.e., $p = p_\infty$, $u = u_\infty$, etc. → Set initial $\delta^*_{b\,l}$ and $\delta^*_{eff} = 0$

$$p_j\left(x, r_j^I\right) = p_\infty$$

Inviscid jet exhaust calculation (SCIPPY)

$p_j(x, r)$
$T_j(x, r)$
$u_j(x, r)$

→ Update inviscid jet exhaust flow map and plume boundary, r_j^I

$$p_j\left(x, r_j^I\right) = p_e\left(x, r_j^I\right)$$

Inviscid flow maps, $\delta^*_{b\,l}$ at nozzle exit

Overlaid mixing-layer calculation (BOAT)

$\delta^*_{eff}(x)$

→ Update effective body shape by underrelaxation
$r_{eff}(x) = r_B(x) + \delta^*_{b\,l}(x)$ over body
$= r_j + \delta^*_{eff}(x)$ over plume

$r_{eff}(x)$

Inviscid external flow calculation (RAXBOD)

$p_e(x, r)$
$T_e(x, r)$
$u_e(x, r)$

→ Update inviscid external flow map and pressure along inviscid plume boundary, r_j^I

$C_p(x)$

Turbulent boundary-layer calculation (Reshotko-Tucker)

$\delta^*_{b\,l}(x)$

→ $C_p(x)$, $\delta^*(x)$ converged? — Yes → STOP

No

Figure 7.- Schematic of main viscous-inviscid iteration loop.
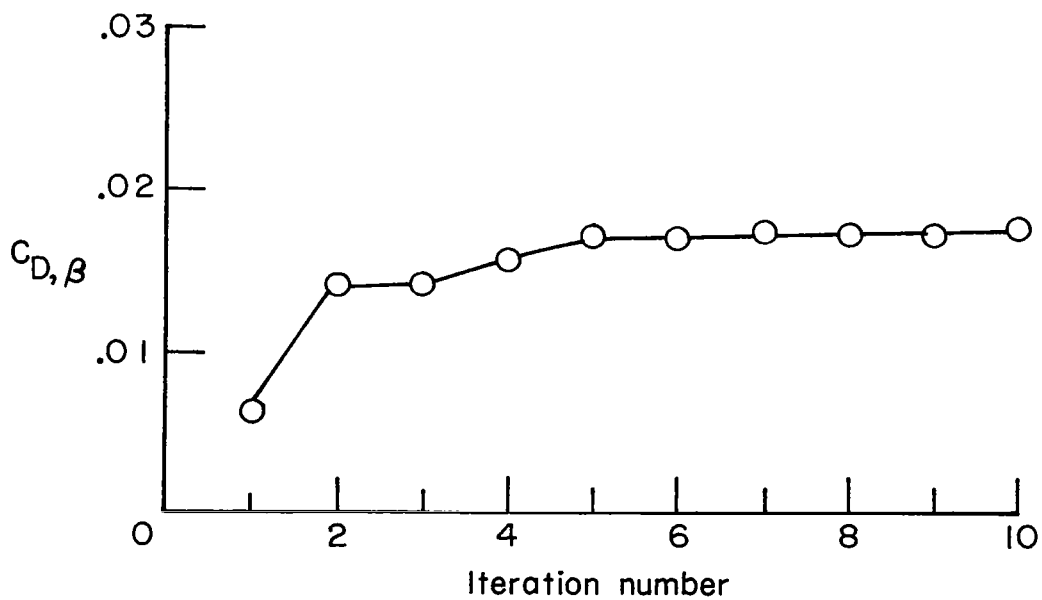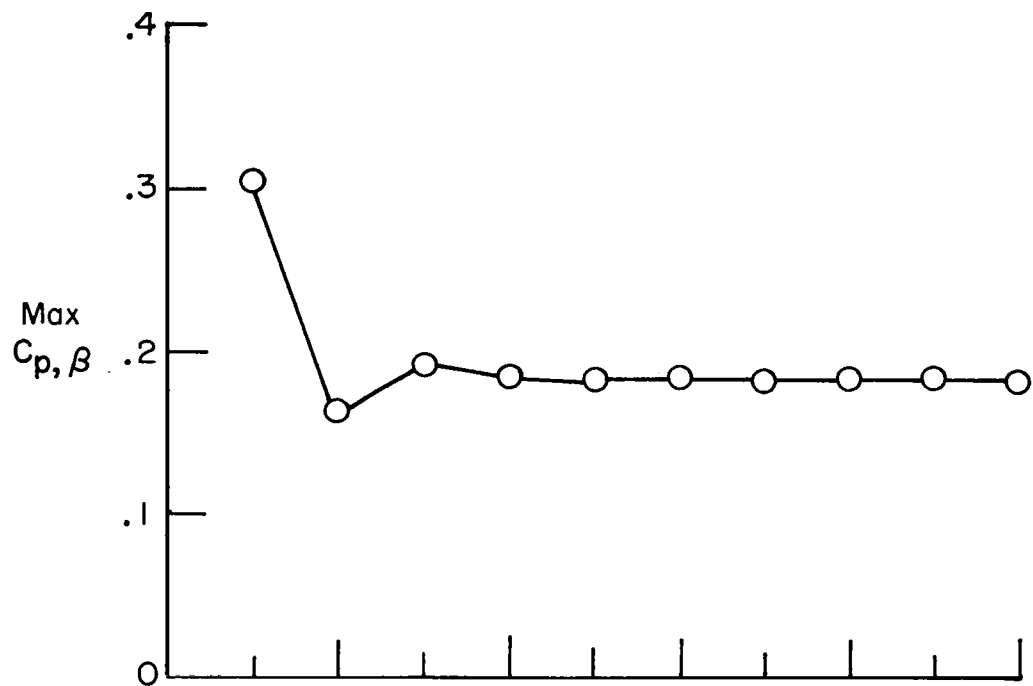
Figure 8.- Typical convergence characteristics of viscous-inviscid
interaction procedure.   Cold-air jet; $M_\infty = 0.4$;   NPR = 2.0.

×   Subsonic-transonic external flow map
O   Supersonic exhaust plume flow map
●   Mixing-layer grid

$\psi_2 (x)$

$u_e (\psi, x)$

Inviscid plume
interface
$\psi = \psi_j$

$u_j (\psi, x)$

$\psi_1 (x)$
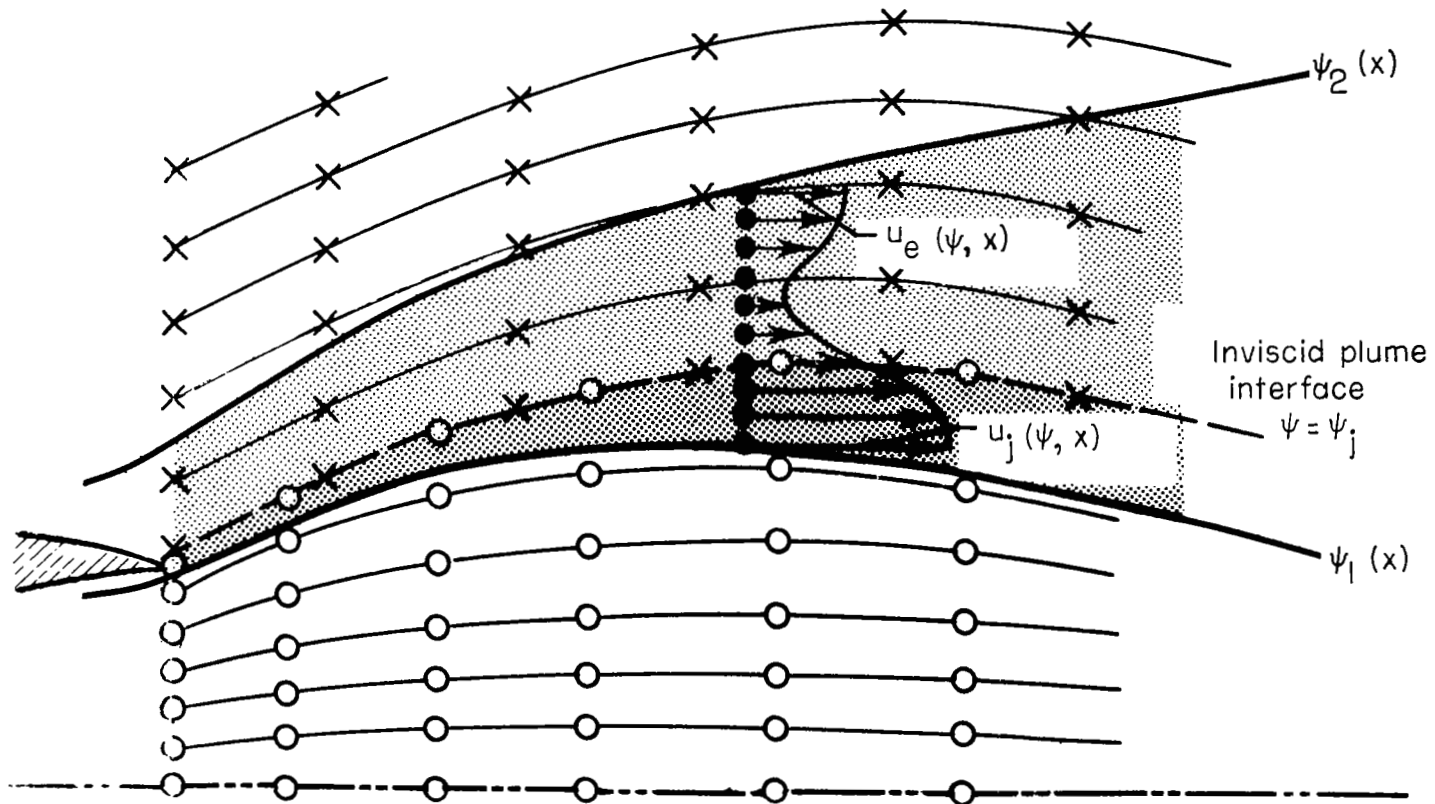
Figure 9.- Computational model for overlaid mixing-layer analysis.
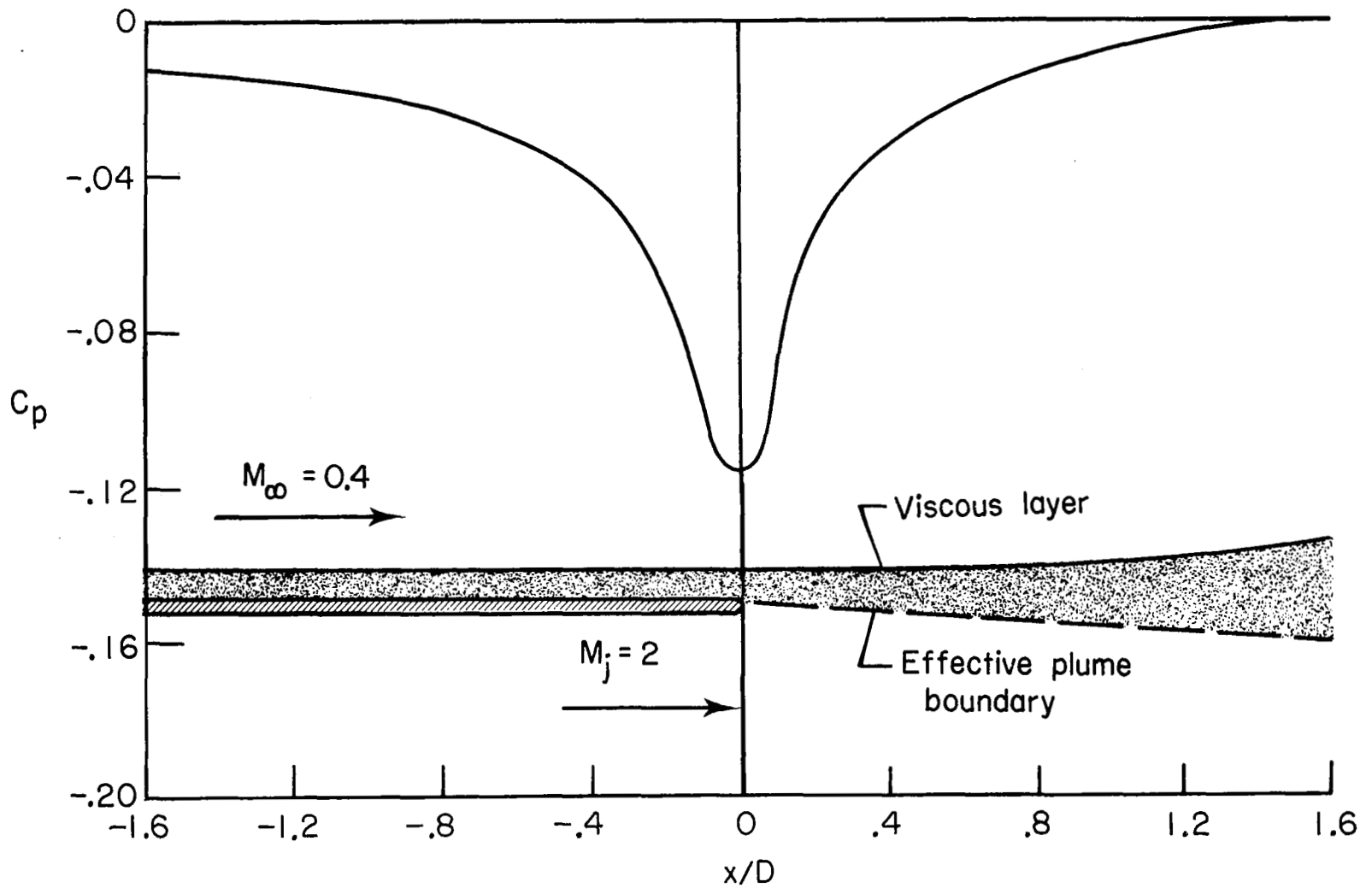
Figure 10.- Inviscid external pressure gradients induced by negative displacement effect for parallel, fully expanded jet exhaust. $N_{Re} = 1.2 \times 10^7$; $p_j = p_\infty$; $u_j/u_\infty = 5$.
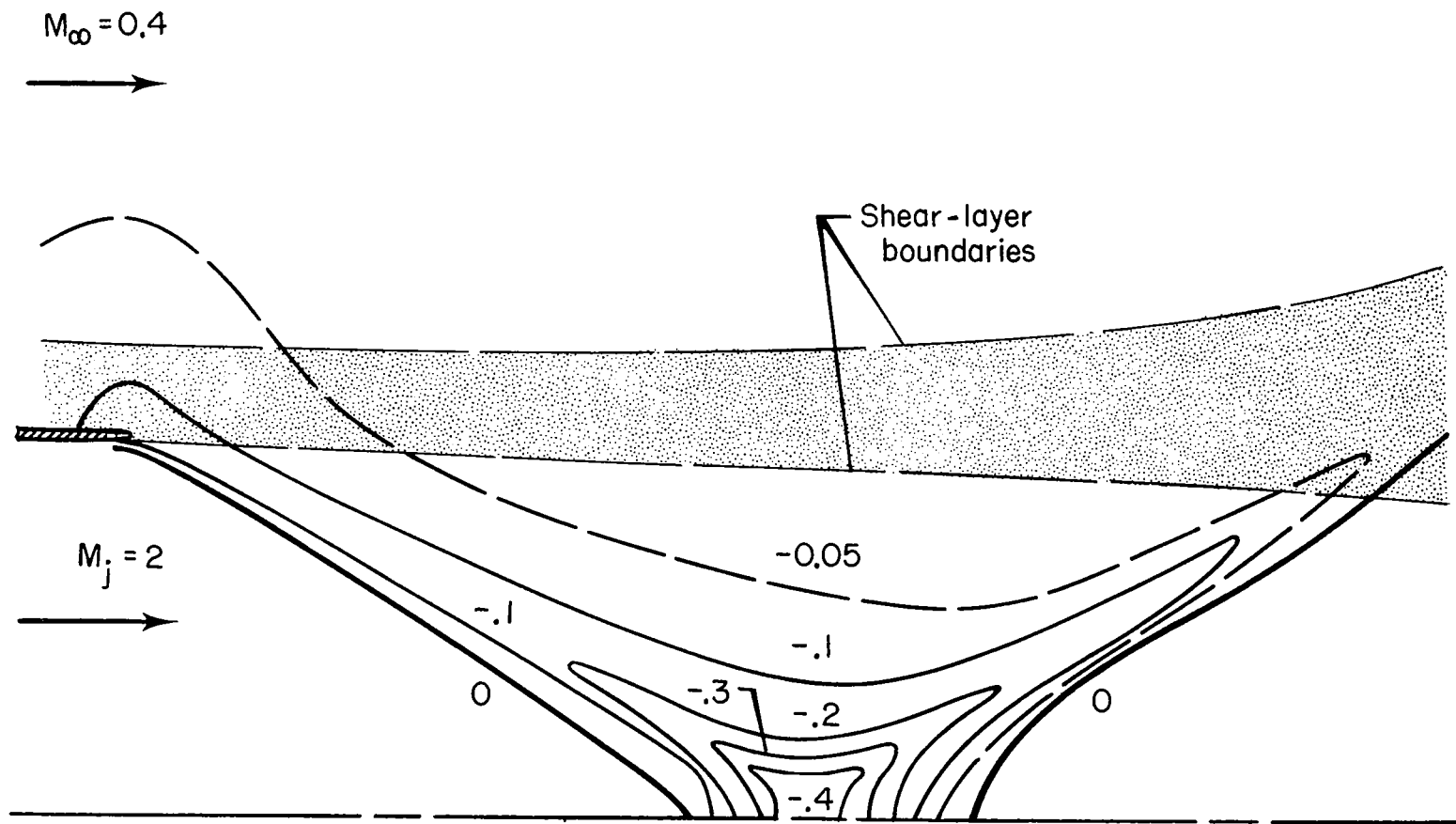
Figure 11.- Inviscid jet exhaust flow structure induced by entrainment. Contour lines of constant C_p. $N_{Re} = 1.2 \times 10^7$; $p_j = p_\infty$; $u_j/u_\infty = 5$.
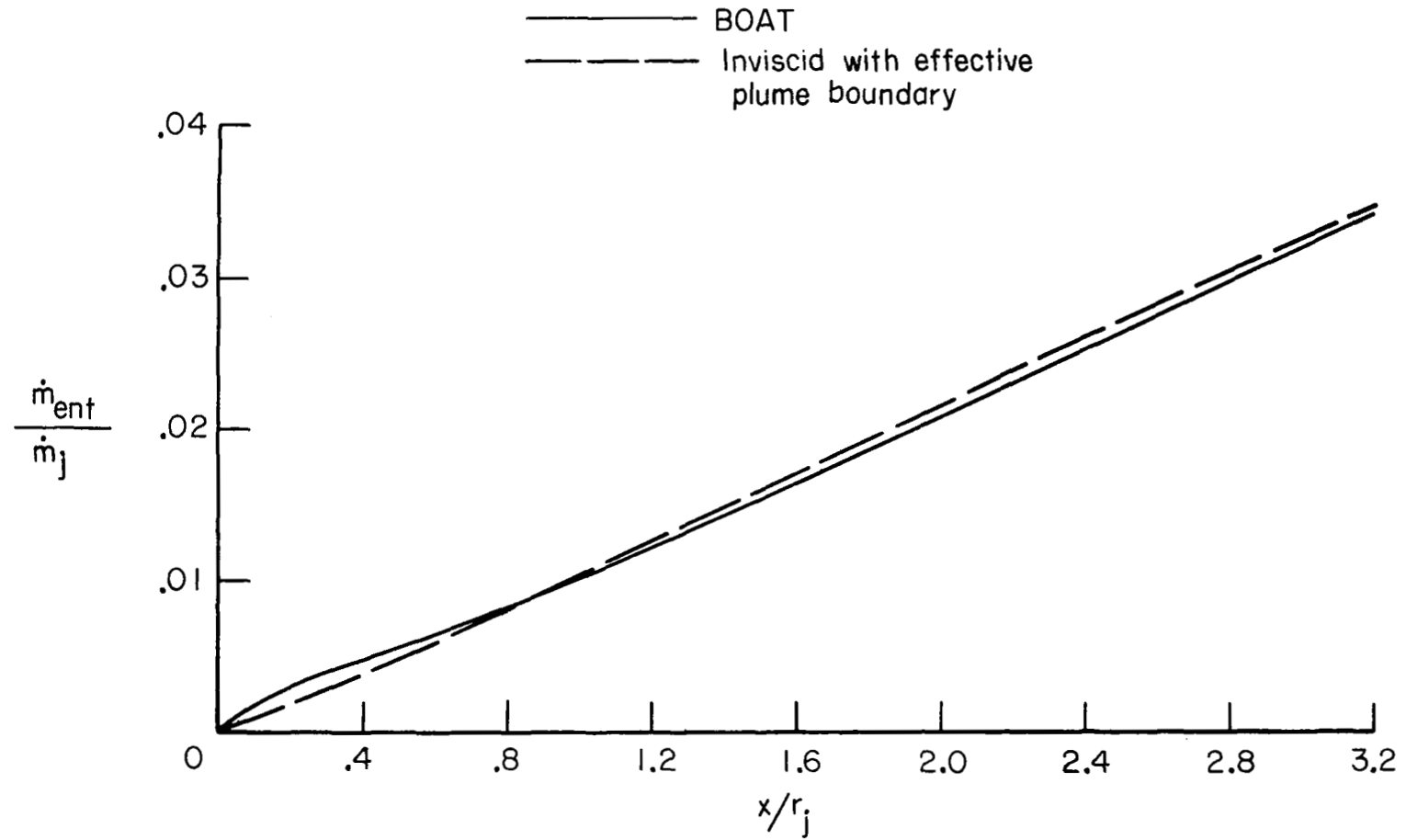
Figure 12.- Comparison of mass entrained across outer mixing-layer boundary calculated by BOAT and by inviscid solution with effective plume boundary. $N_{Re} = 1.2 \times 10^7$; $p_j = p_\infty$; $u_j/u_\infty = 5$.
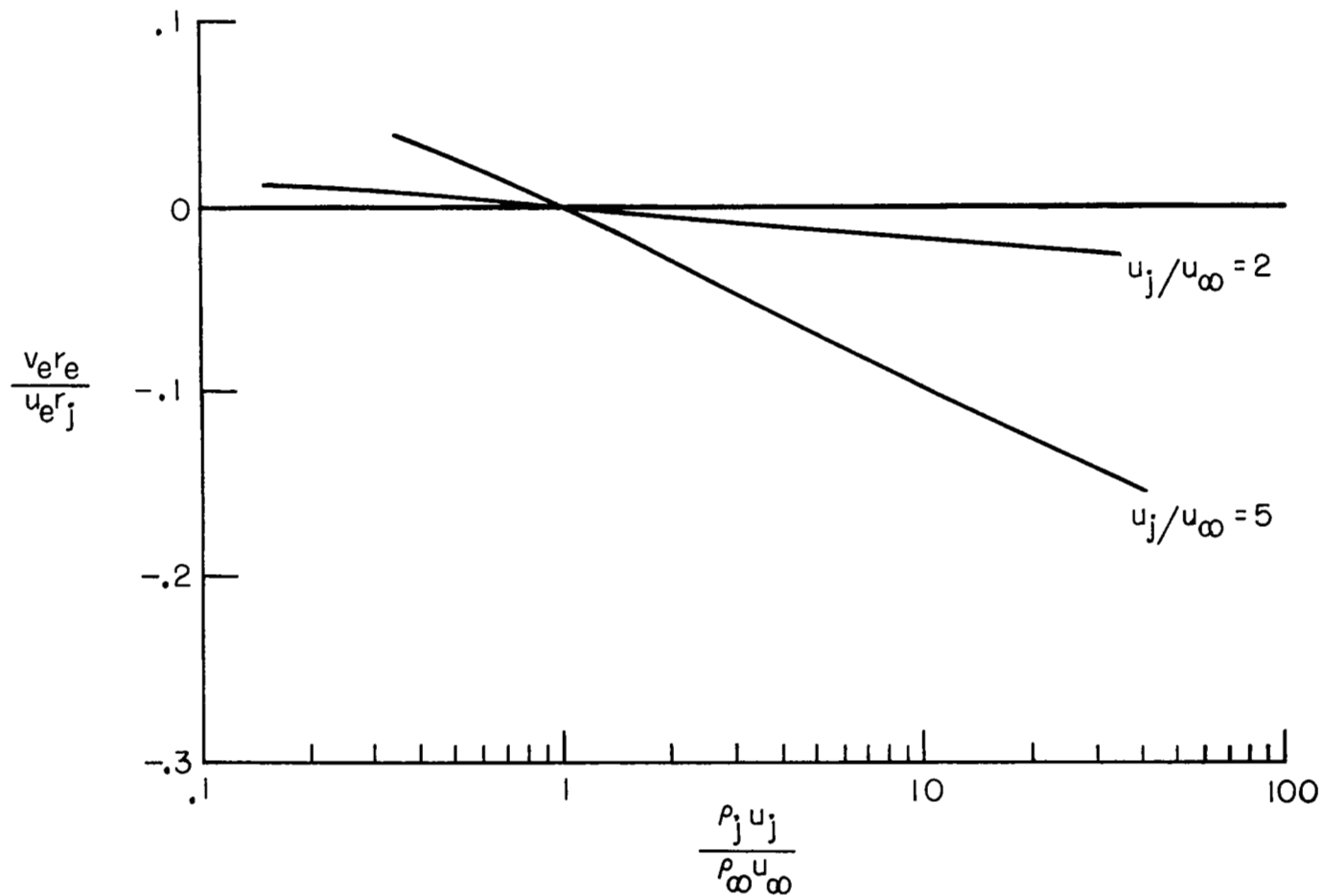
Figure 13.- Variation of near-field source strength due to entrainment with mass flow and velocity ratios. No external boundary layer; $p_j = p_\infty$; $T_j = T_\infty$; $x/r_j = 1$.
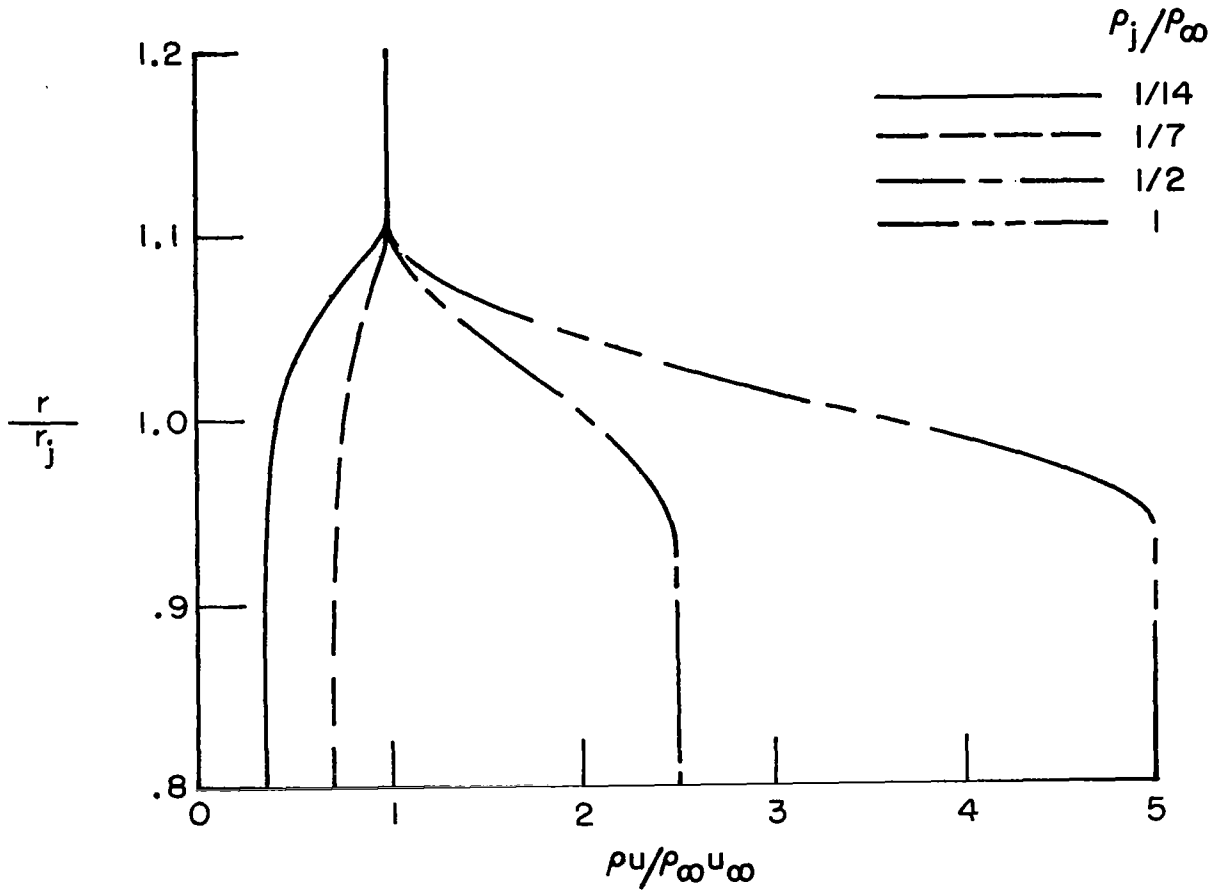
Figure 14.- Variation of mass-flow ratio across shear layer for
various density ratios. $u_j/u_\infty = 5$; $p_j = p_\infty$; $T_j = T_\infty$;
$x/r_j = 1.0$.
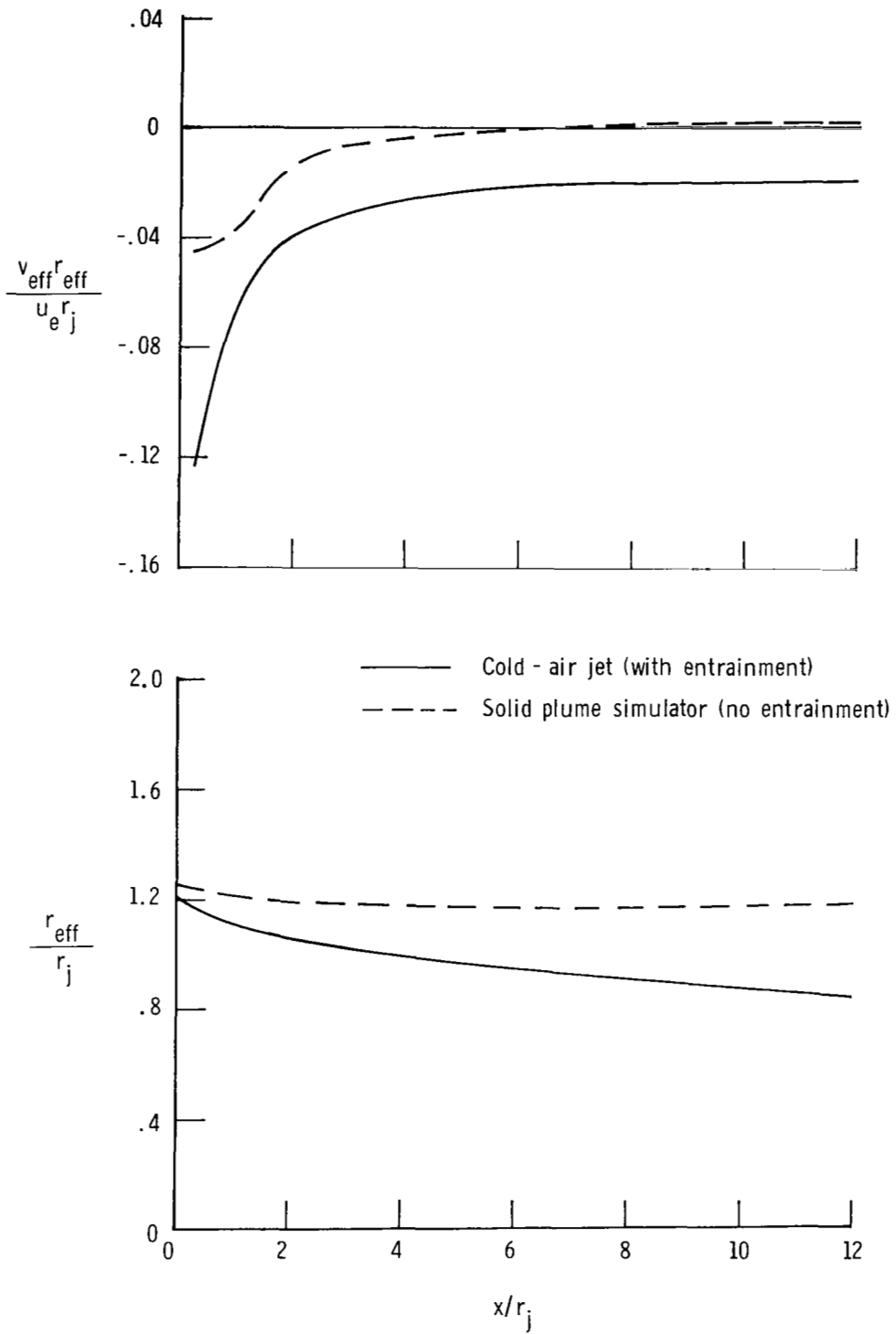
Figure 15.- Effect of entrainment on effective plume
boundary and source strength distribution.
$M_\infty = 0.4$;   NPR = 2.0.
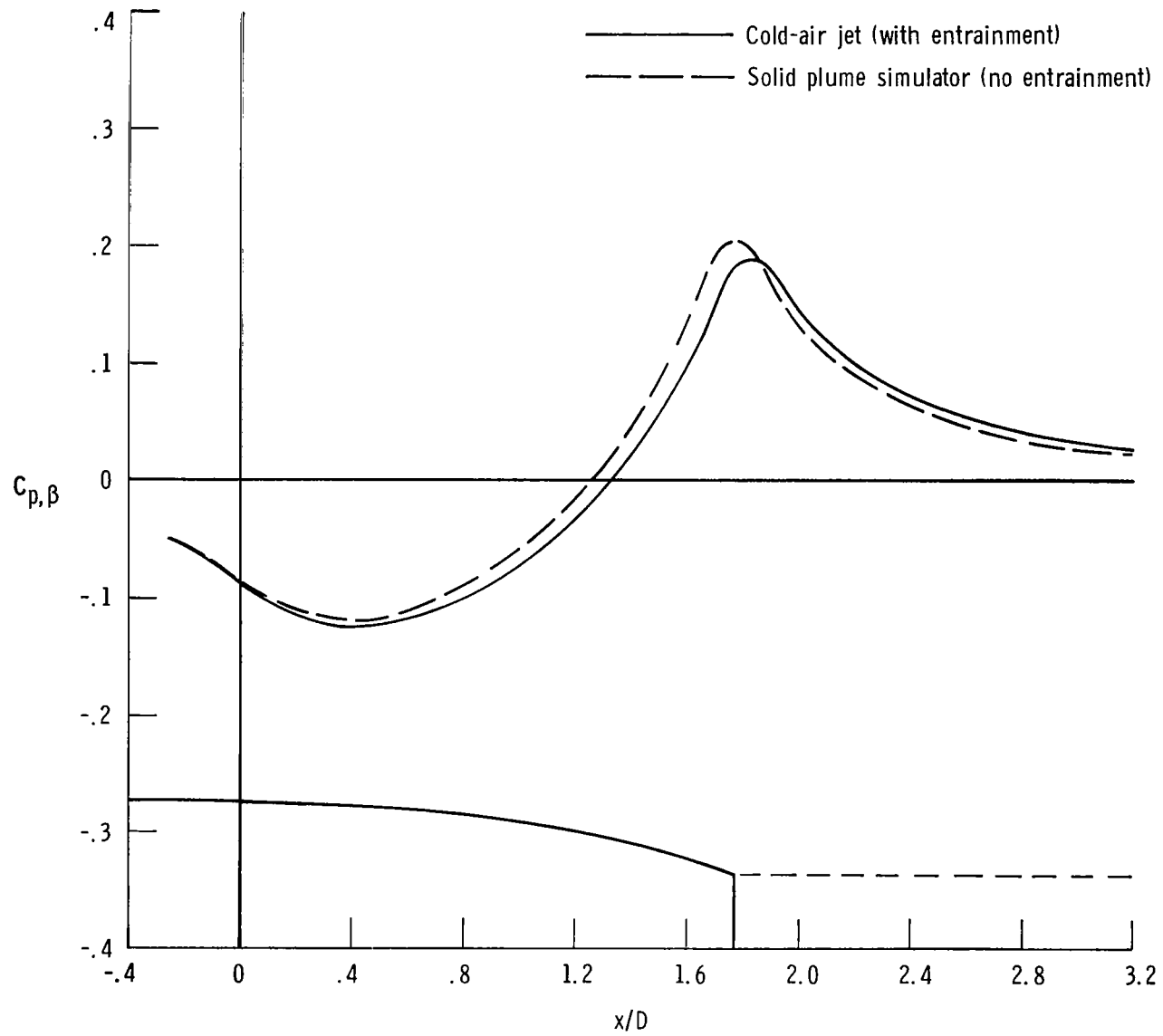
Figure 16.- Effect of entrainment on predicted boattail pressures.
$M_\infty = 0.4$; NPR = 2.0.
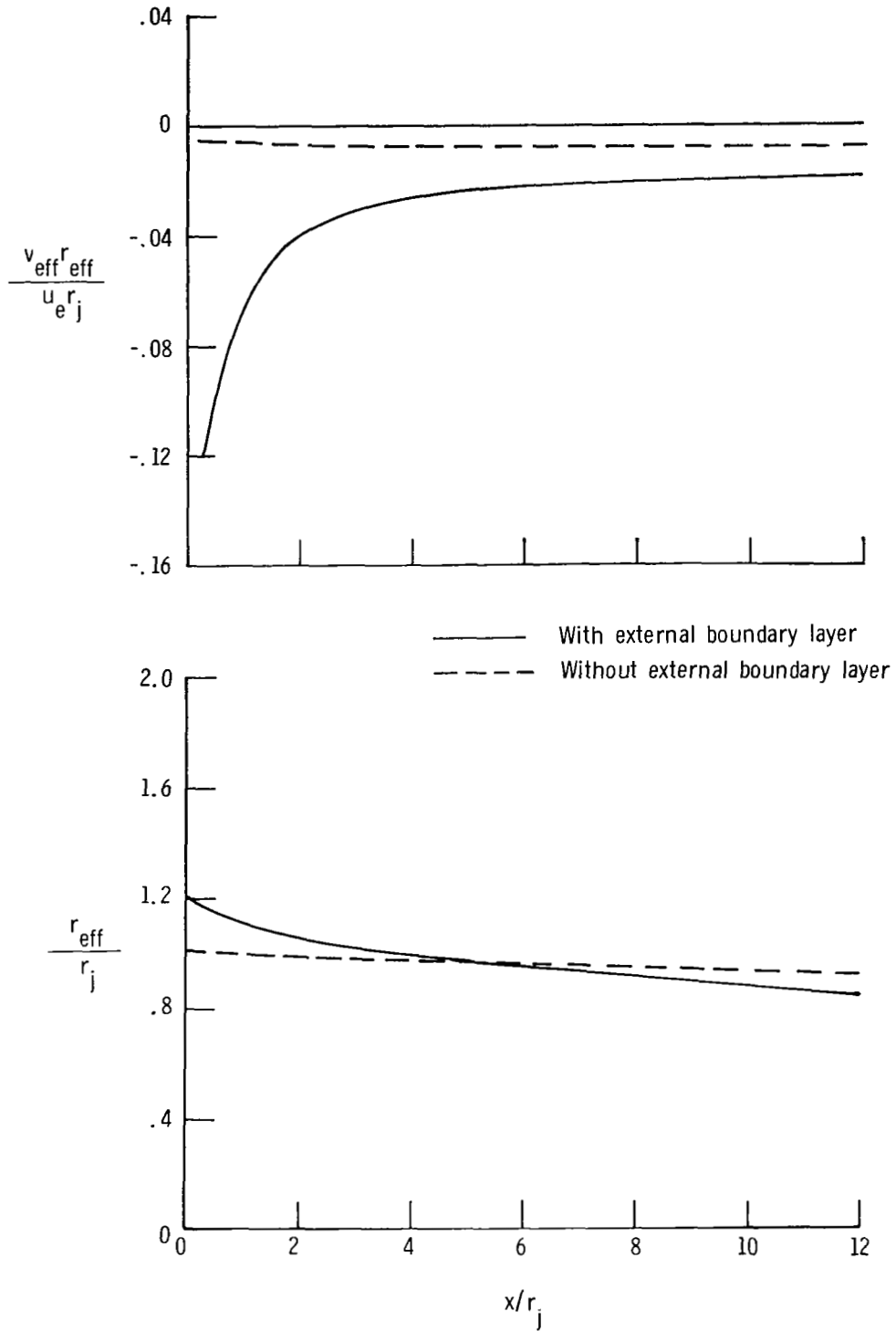
Figure 17.- Effect of external boundary layer on effective
plume boundary and source strength distribution.
$M_\infty = 0.4$; NPR = 2.0.
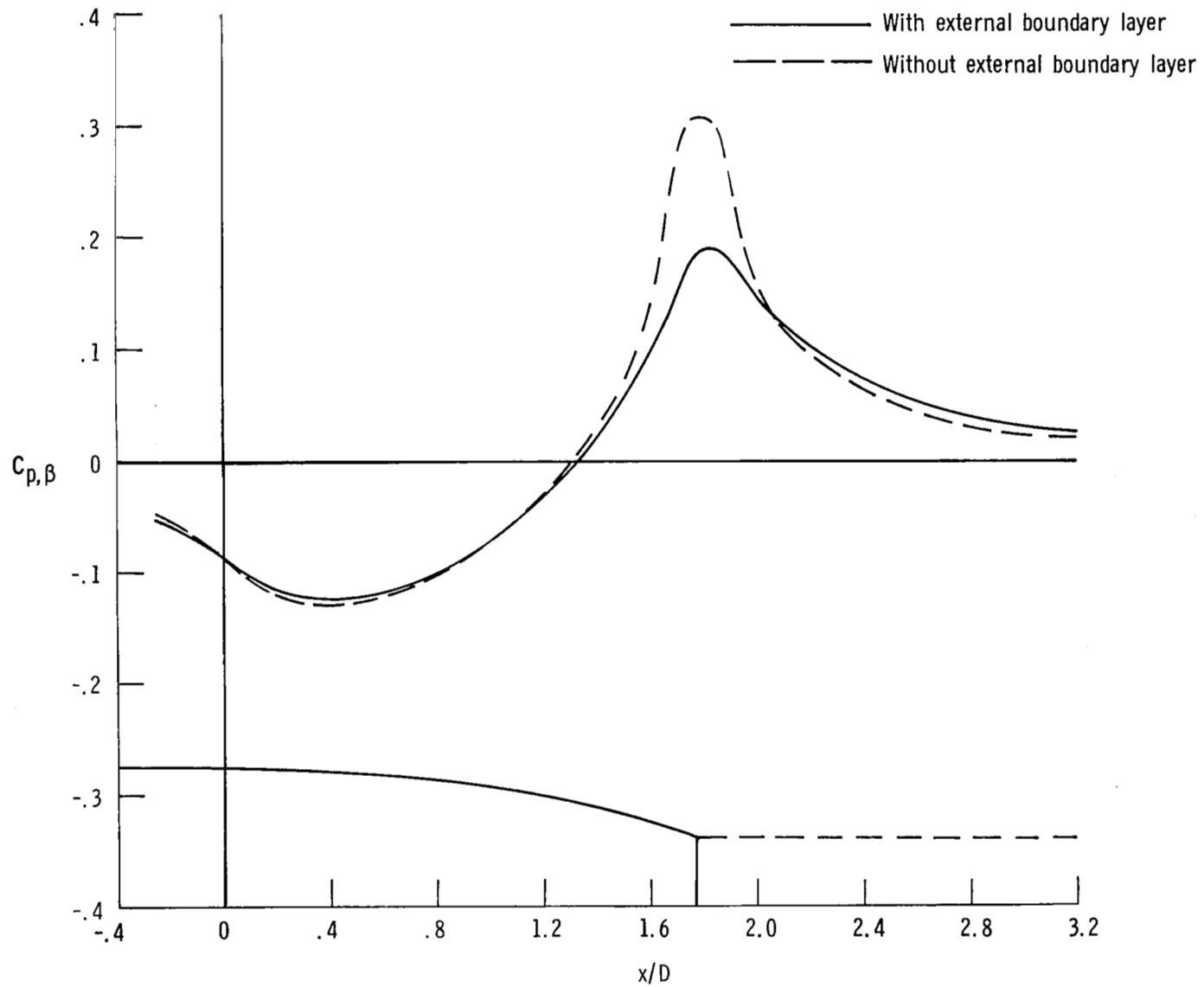
Figure 18.- Effect of external boundary layer on predicted boattail pressures.
$M_\infty = 0.4$;   NPR = 2.0.
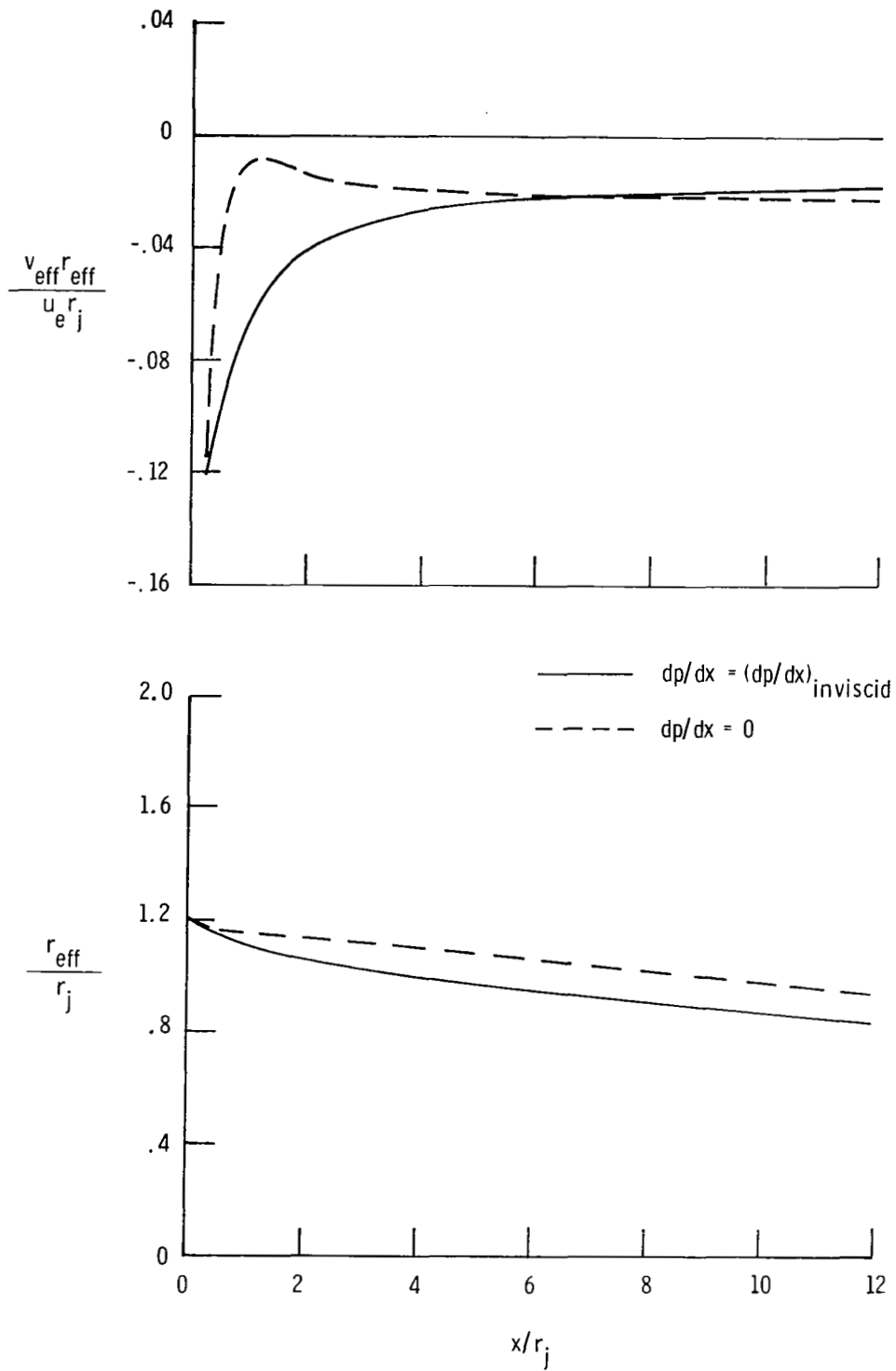
Figure 19.- Effect of neglecting pressure gradient in mixing-layer calculation on effective plume boundary and source strength distribution. $M_\infty = 0.4$; NPR = 2.0.
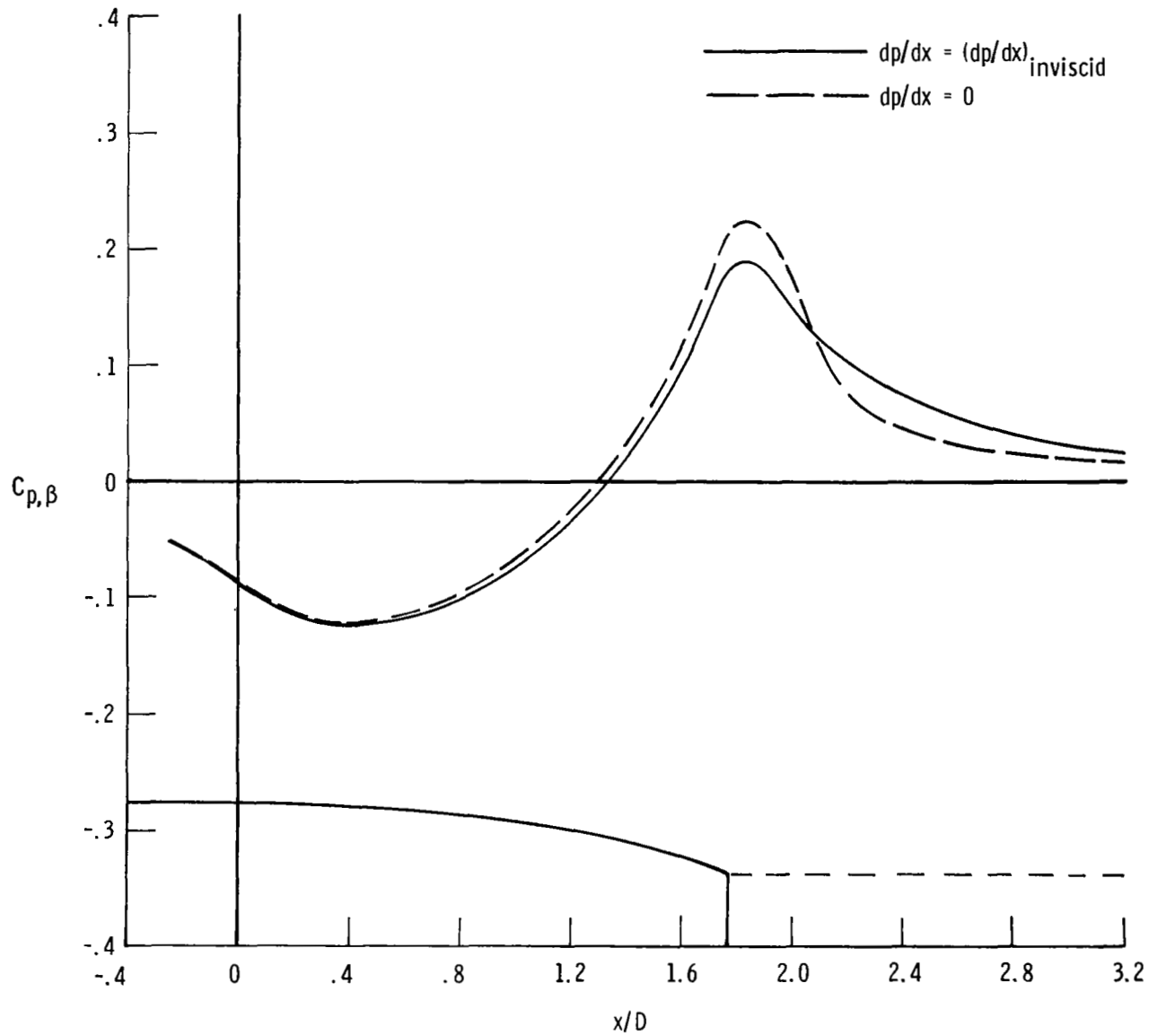
Figure 20.- Effect of neglecting pressure gradient in mixing-layer calculation on predicted boattail pressures. $M_\infty = 0.4$; NPR = 2.0.
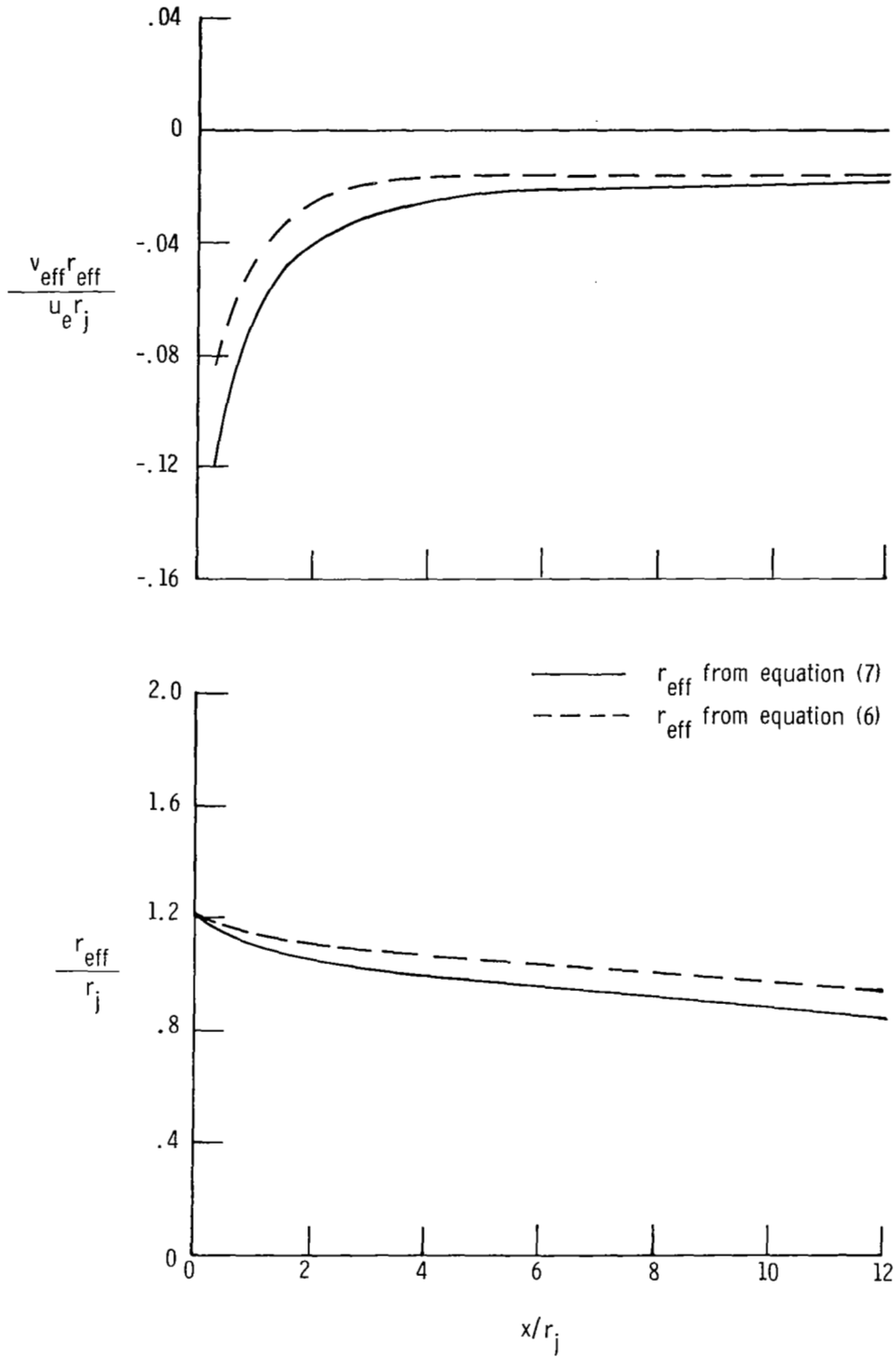
Figure 21.- Effect of including $d\rho_e u_e/dx$ in calculation of effective plume boundary and source strength distribution. $M_\infty = 0.4$; NPR = 2.0.
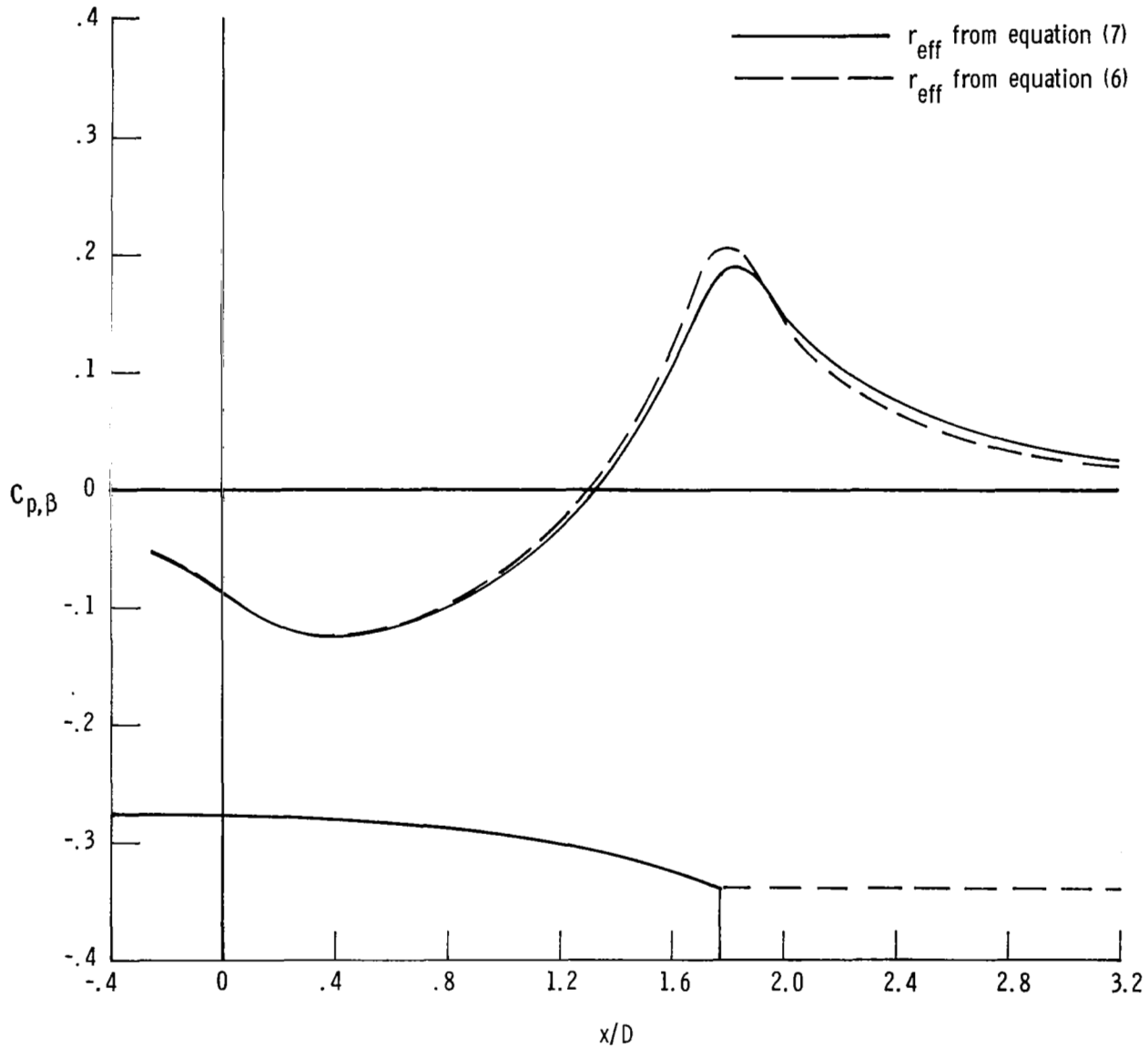
Figure 22.- Effect of including $d\rho_e u_e/dx$ in effective boundary calculation on predicted boattail pressures. $M_\infty = 0.4$; NPR = 2.0.
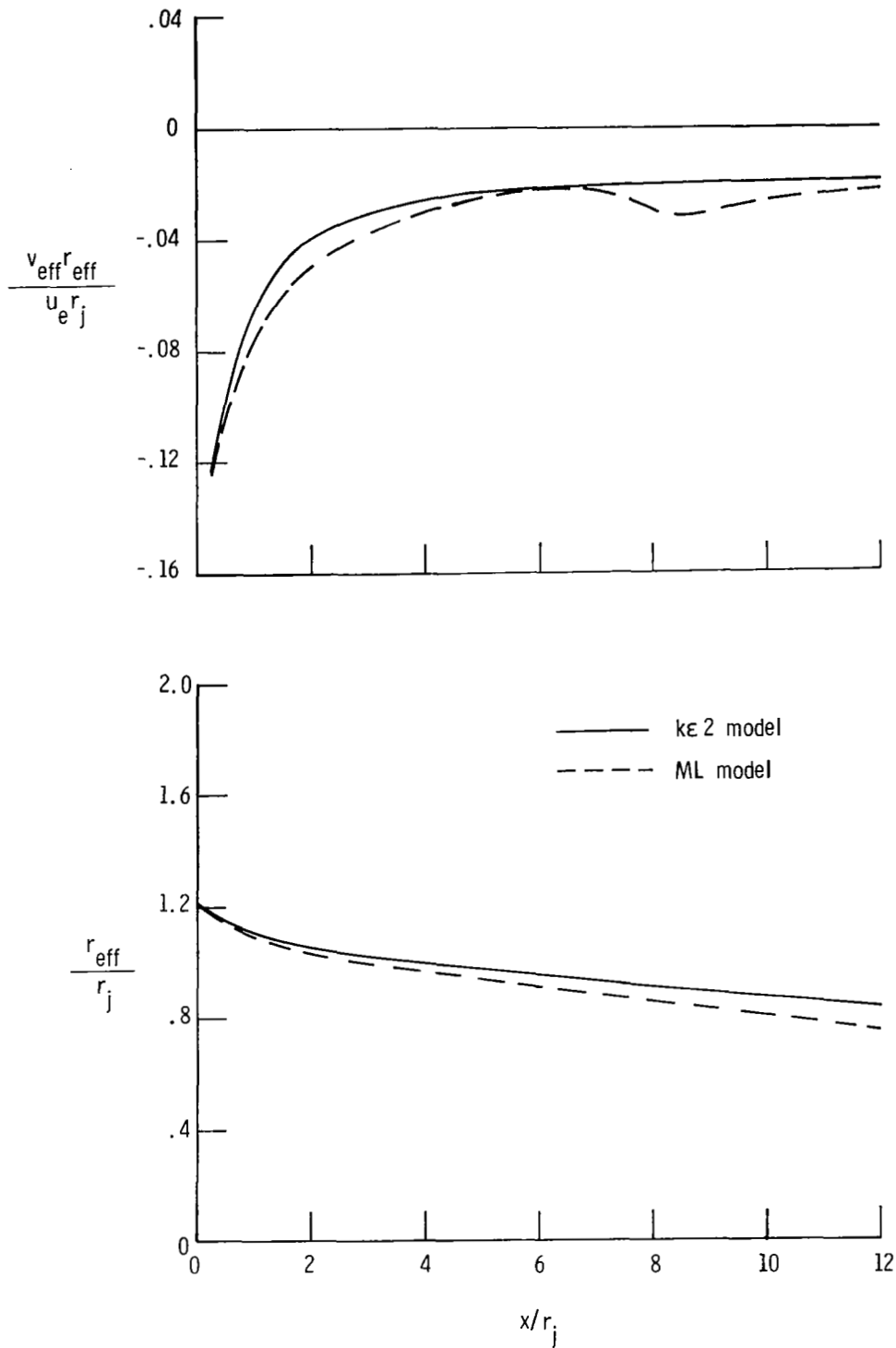
Figure 23.- Effect of mixing-layer turbulence model on effective plume boundary and source strength distribution. $M_\infty = 0.4$; NPR = 2.0.
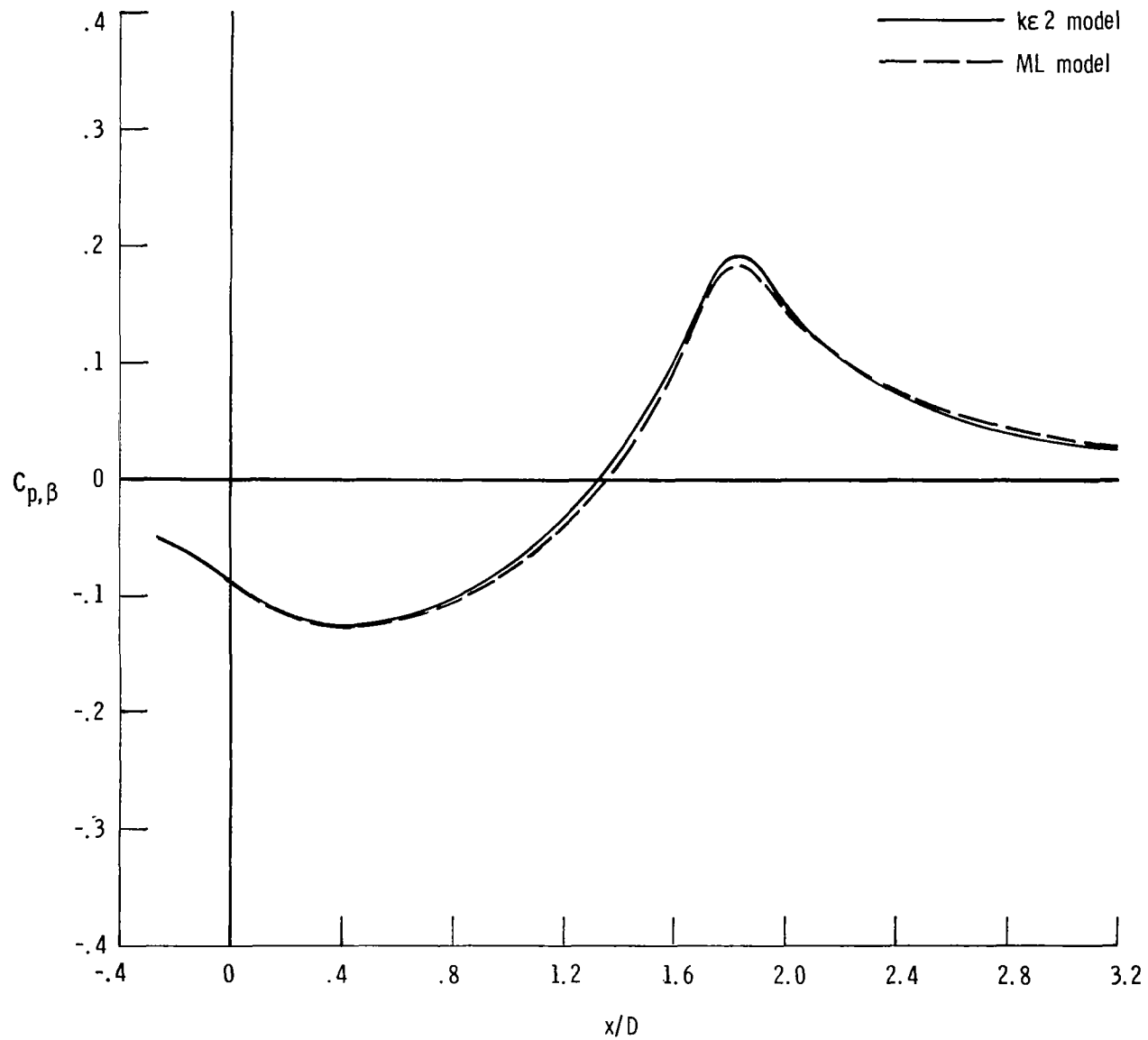
Figure 24.- Effect of mixing-layer turbulence model on predicted boattail pressures. $M_\infty = 0.4$; NPR = 2.0.
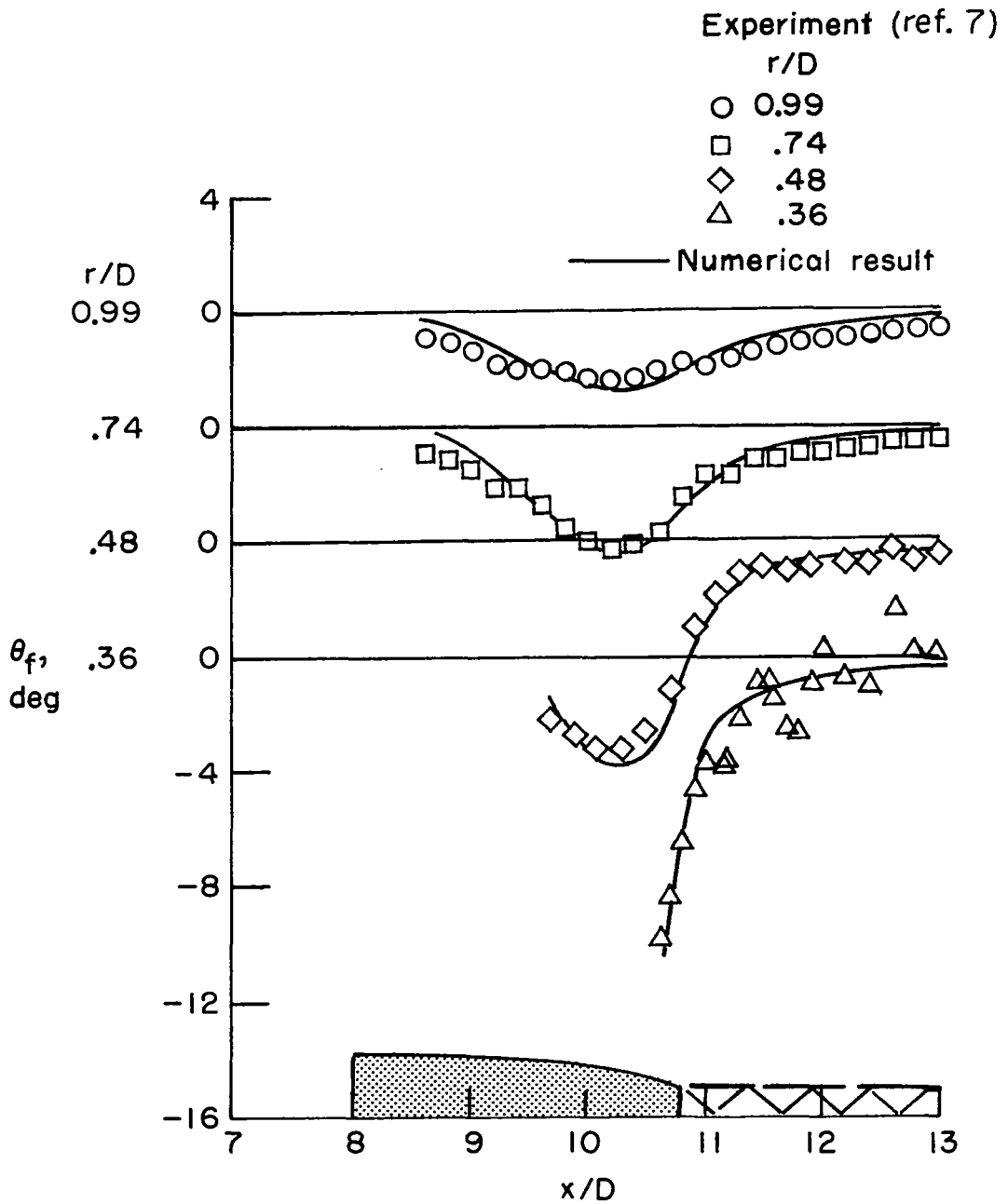
(a) Local streamline flow angles.

Figure 25.- Comparisons between predicted and measured flow-field
data for cold-air jet exhaust. $M_\infty = 0.6$; NPR = 2.9.
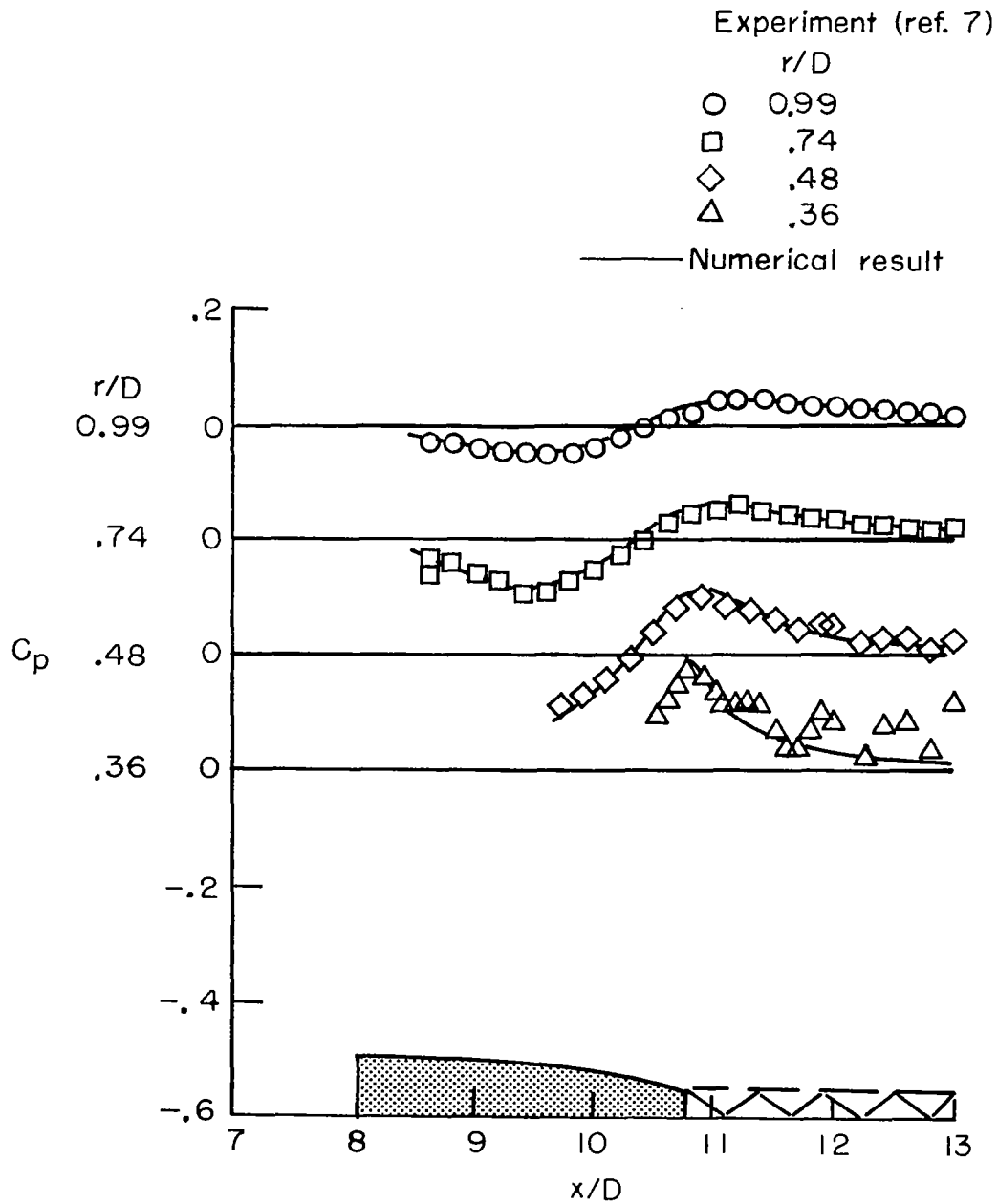
(b) Local pressure coefficients.

Figure 25.- Concluded.

(a) Effect of turbulence model.
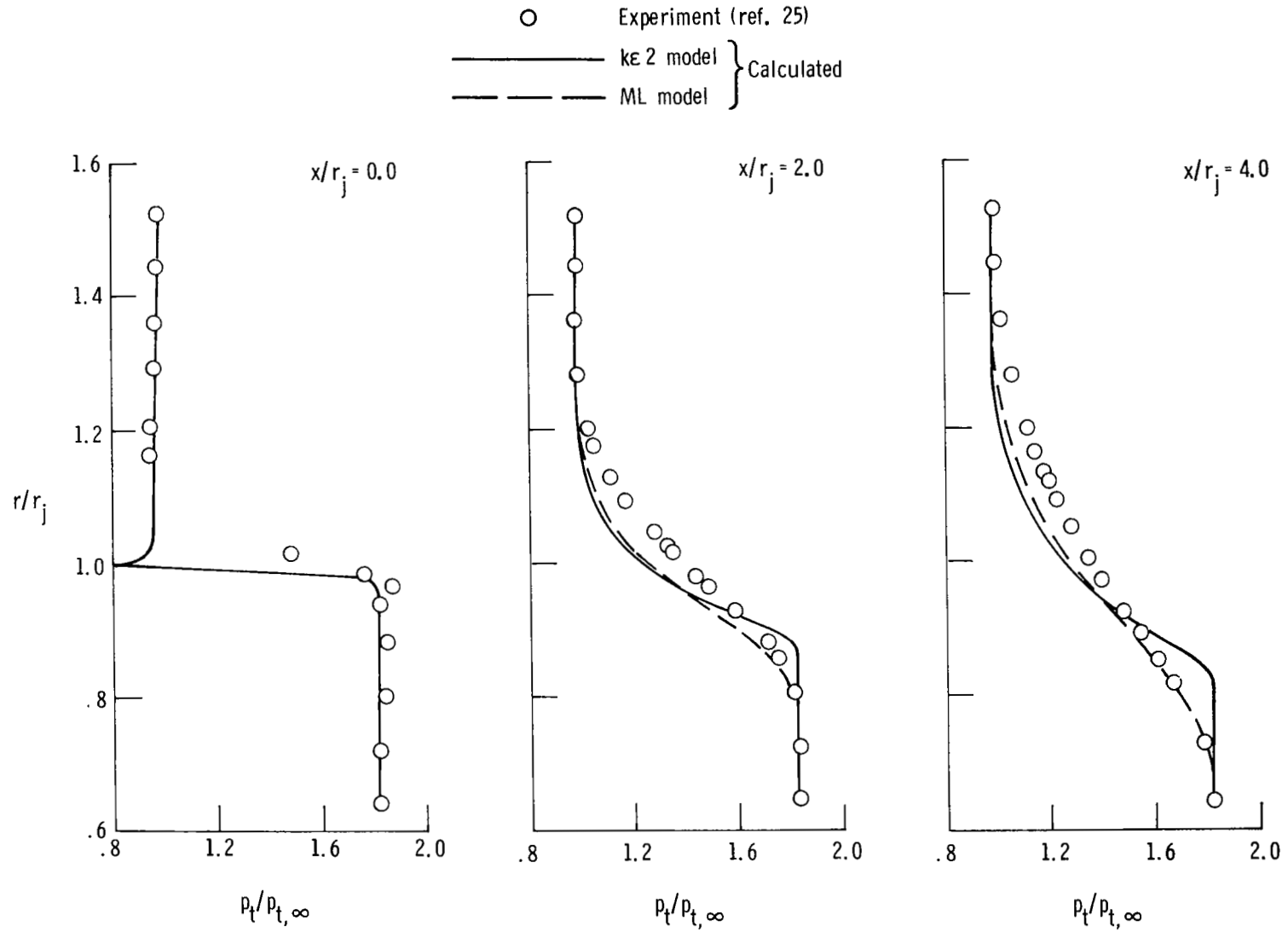
Figure 26.- Comparison of predicted and measured total-pressure profiles at several axial locations in mixing layer. $M_\infty = 0.4$; NPR = 2.0.
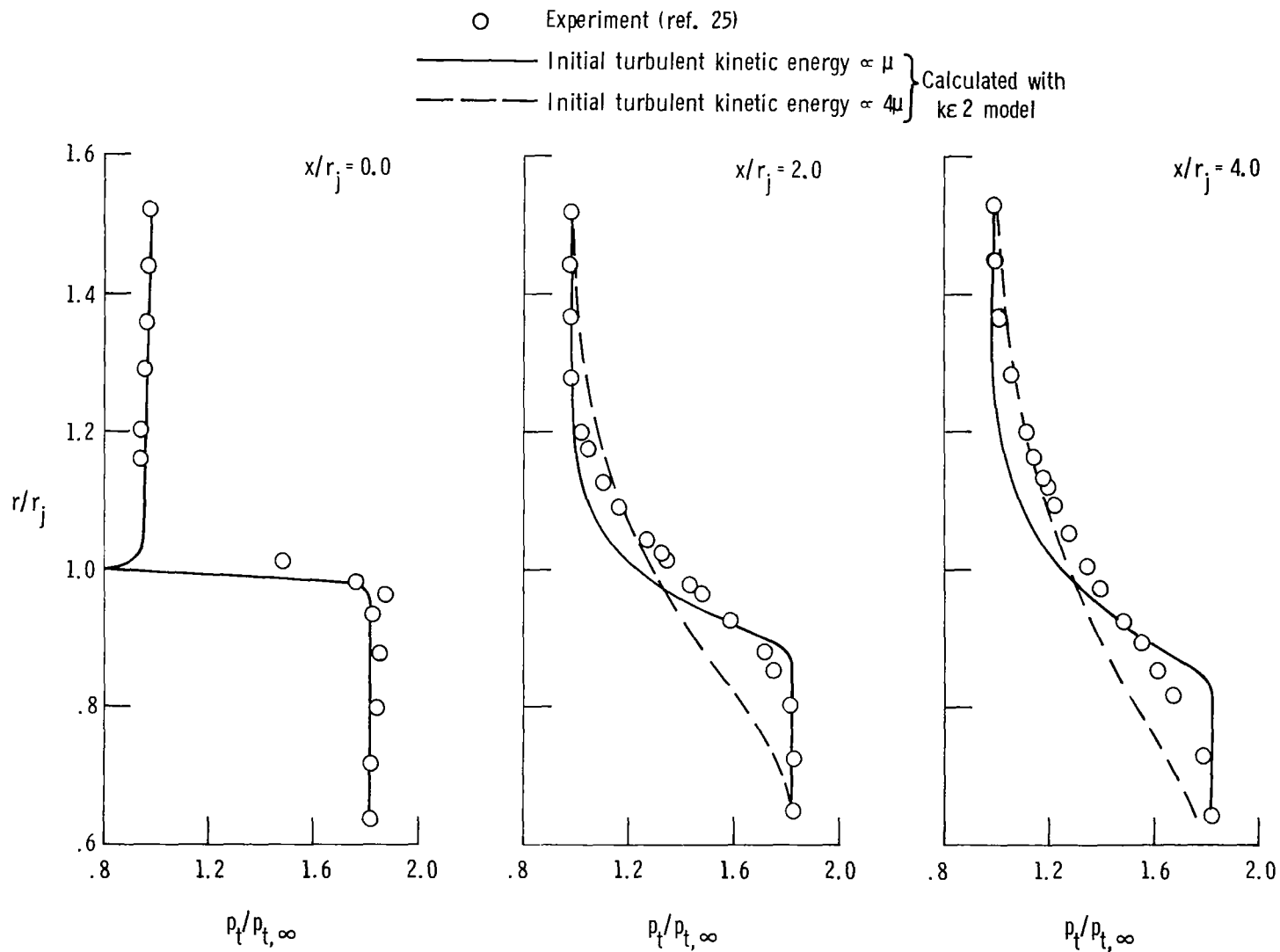
(b) Effect of initial turbulent kinetic energy.

Figure 26.- Concluded.
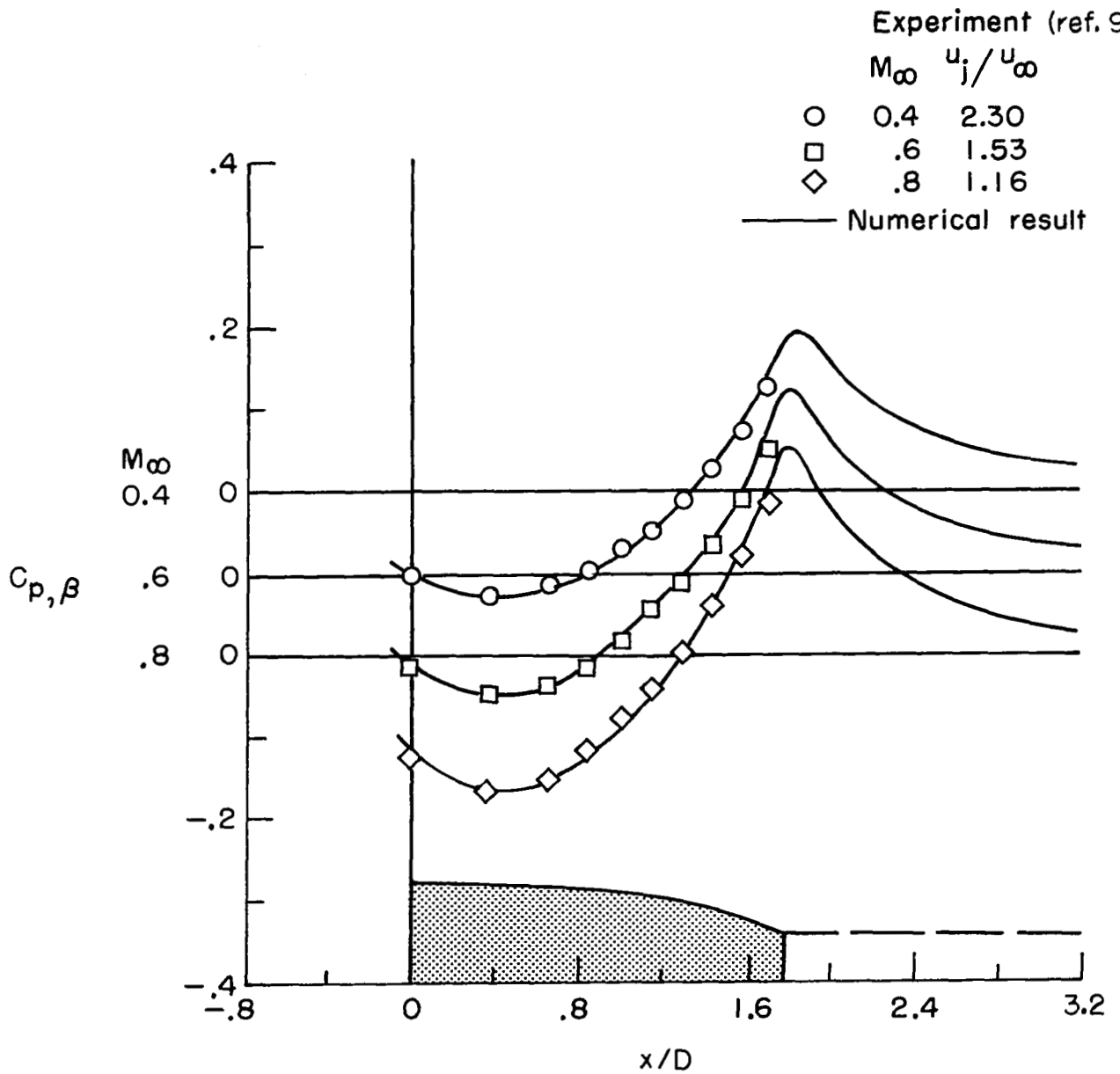
(a) Effect of free-stream Mach number at NPR = 2.0.

Figure 27.- Comparisons between predicted and measured boattail pressure distributions for cold-air jet exhaust.
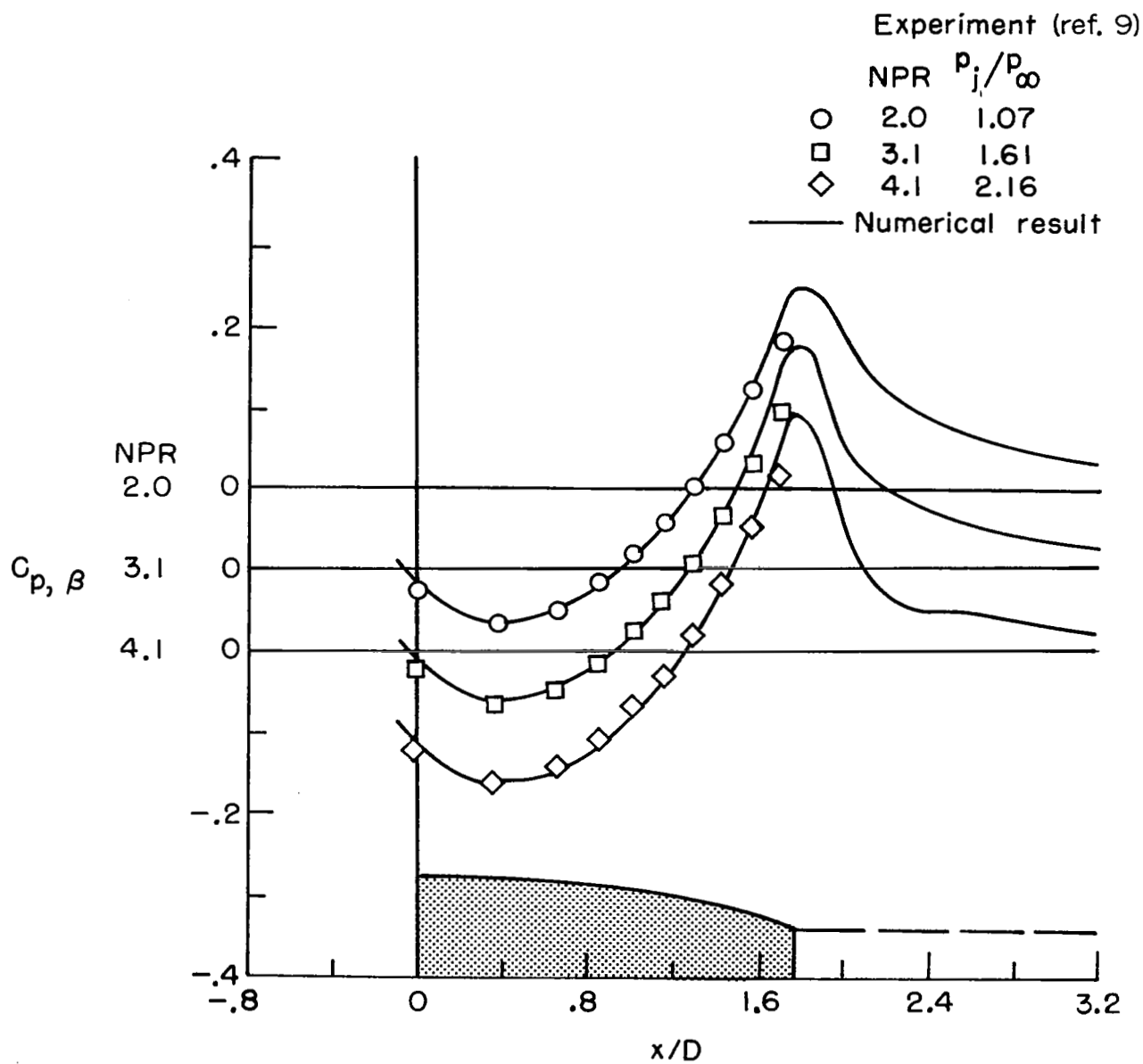
(b) Effect of NPR at $M_\infty = 0.80$.

Figure 27.- Concluded.
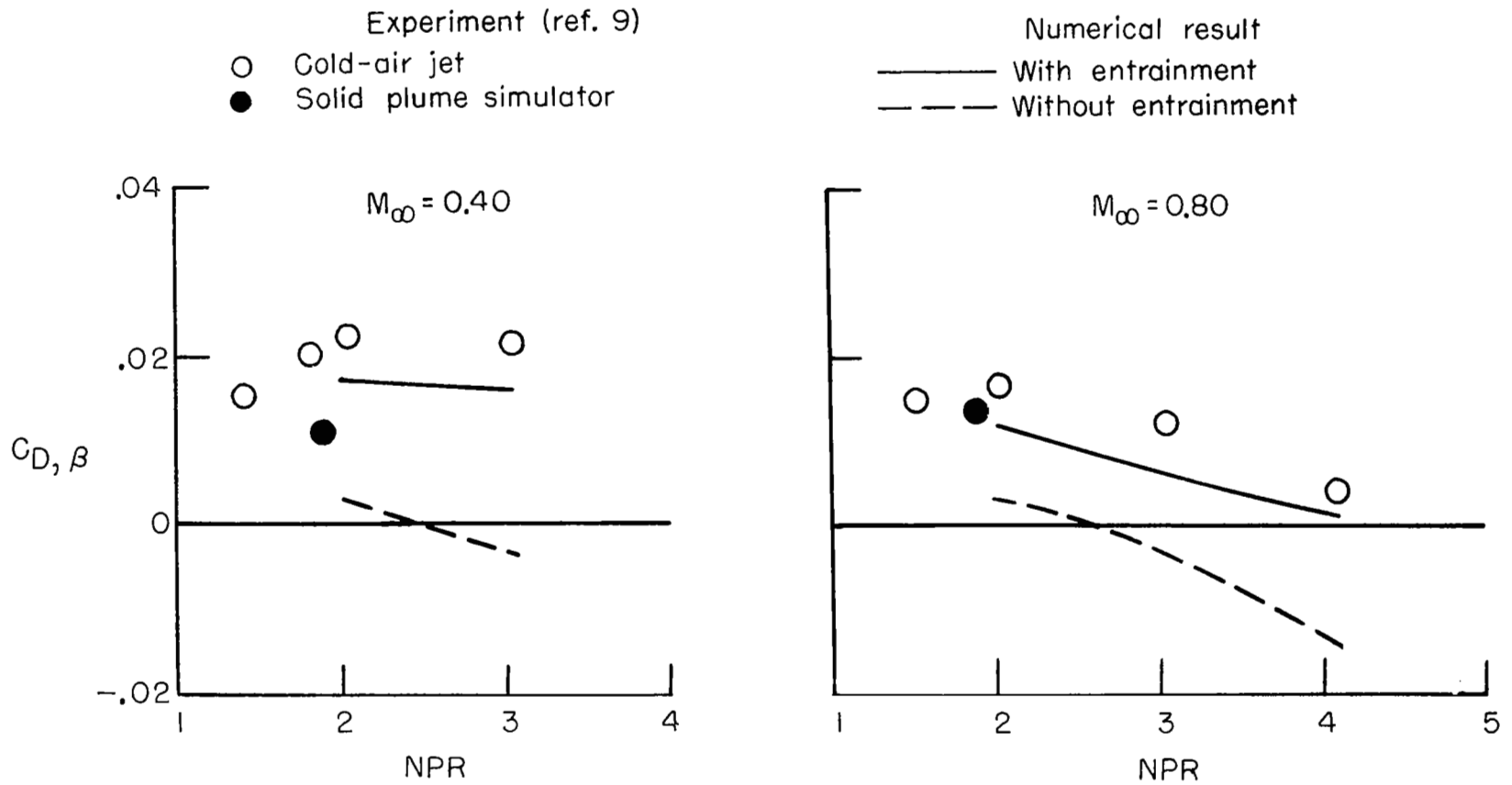
Figure 28.- Comparisons between predicted and measured boattail drag.
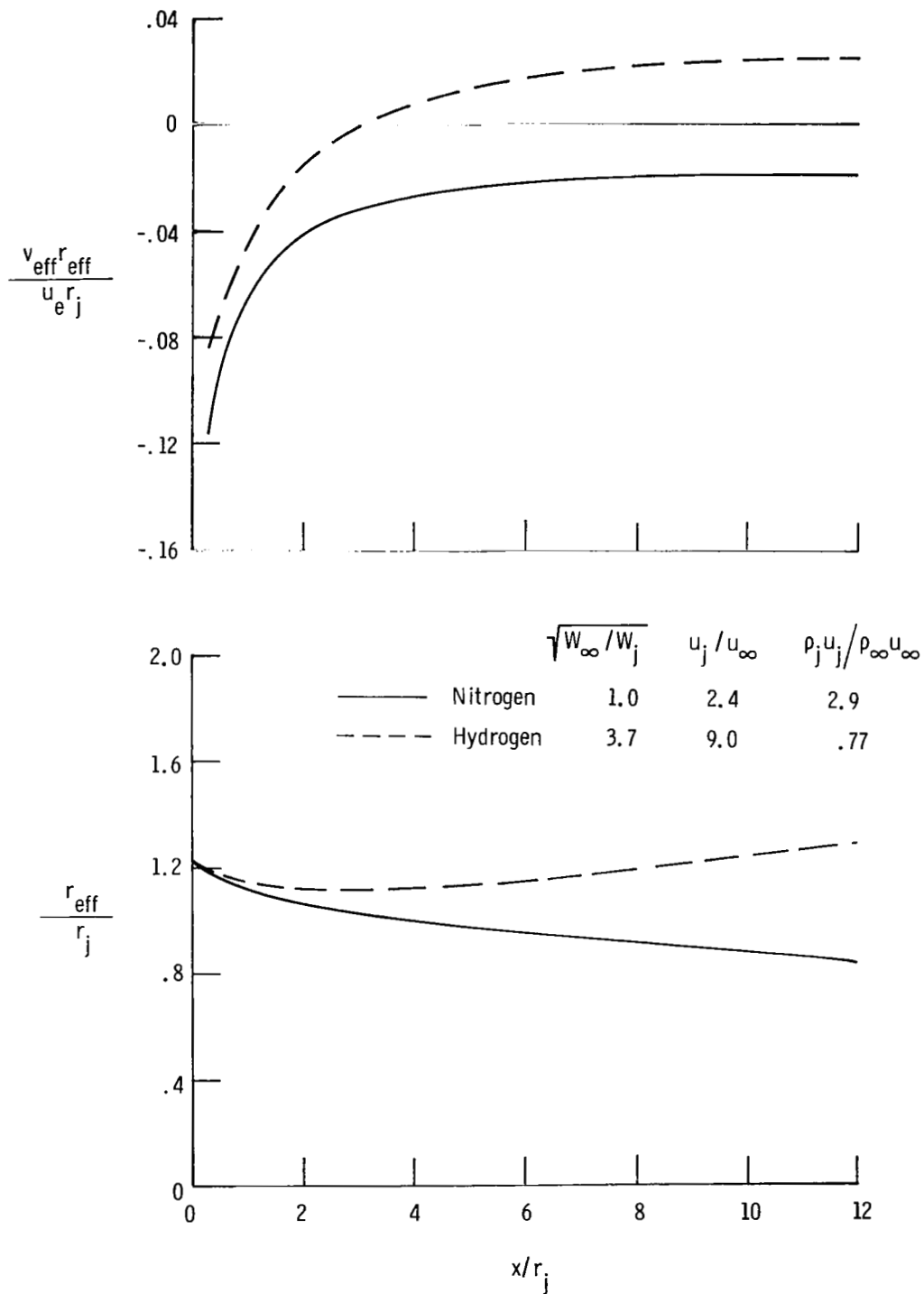
Figure 29.- Effect of jet exhaust composition on effective plume boundary and source strength distribution. $M_\infty = 0.4$; NPR = 2.0; $T_j/T_\infty = 0.82$.
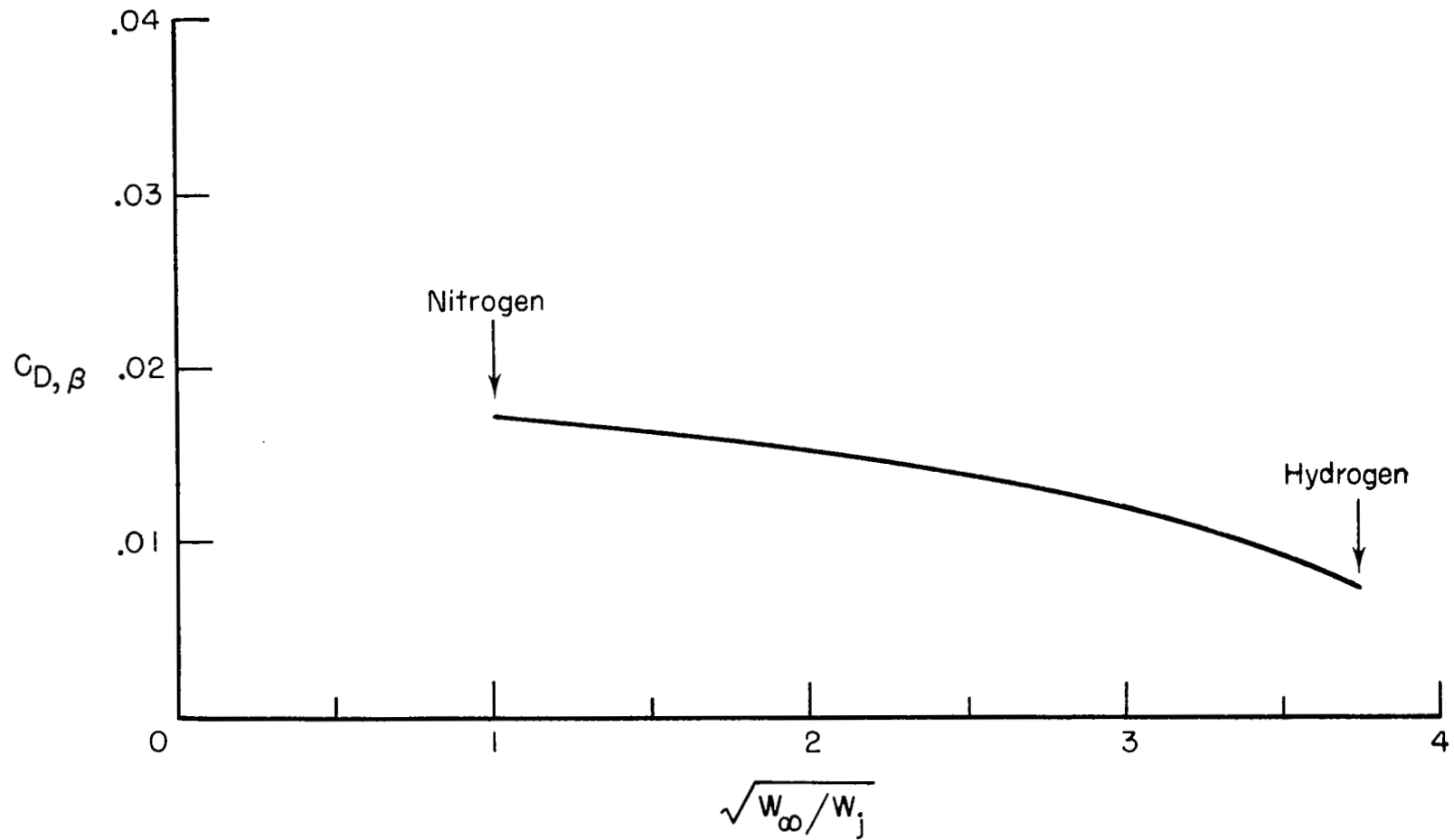
Figure 30.- Effect of jet exhaust composition on predicted boattail drag.
$M_\infty = 0.4$;   NPR = 2.0; $T_j/T_\infty = 0.82$.
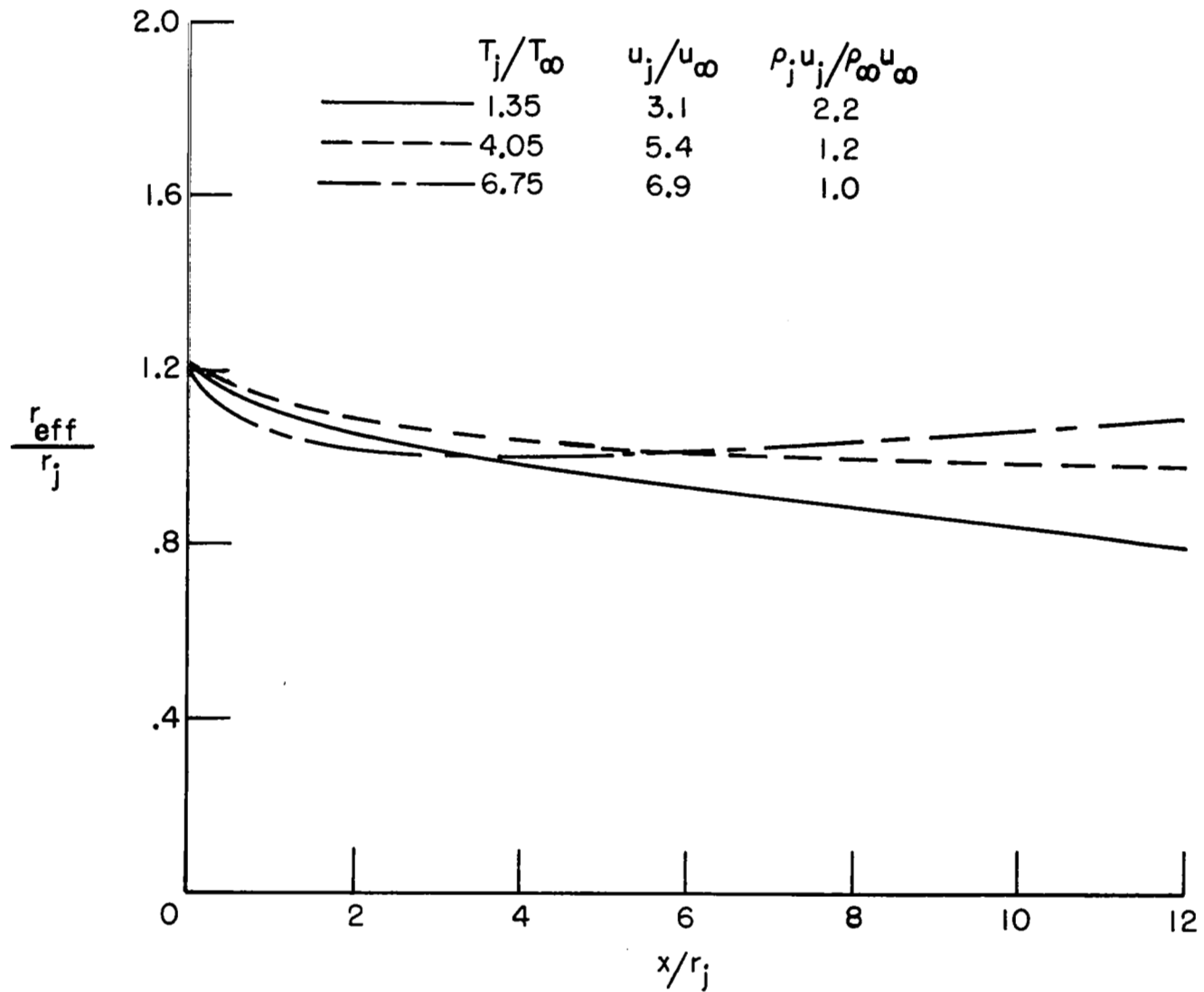
Figure 31.- Effect of jet exhaust temperature on effective plume boundary.
$M_\infty = 0.4$; NPR = 2.0; $W_j/W_\infty = 1.0$.
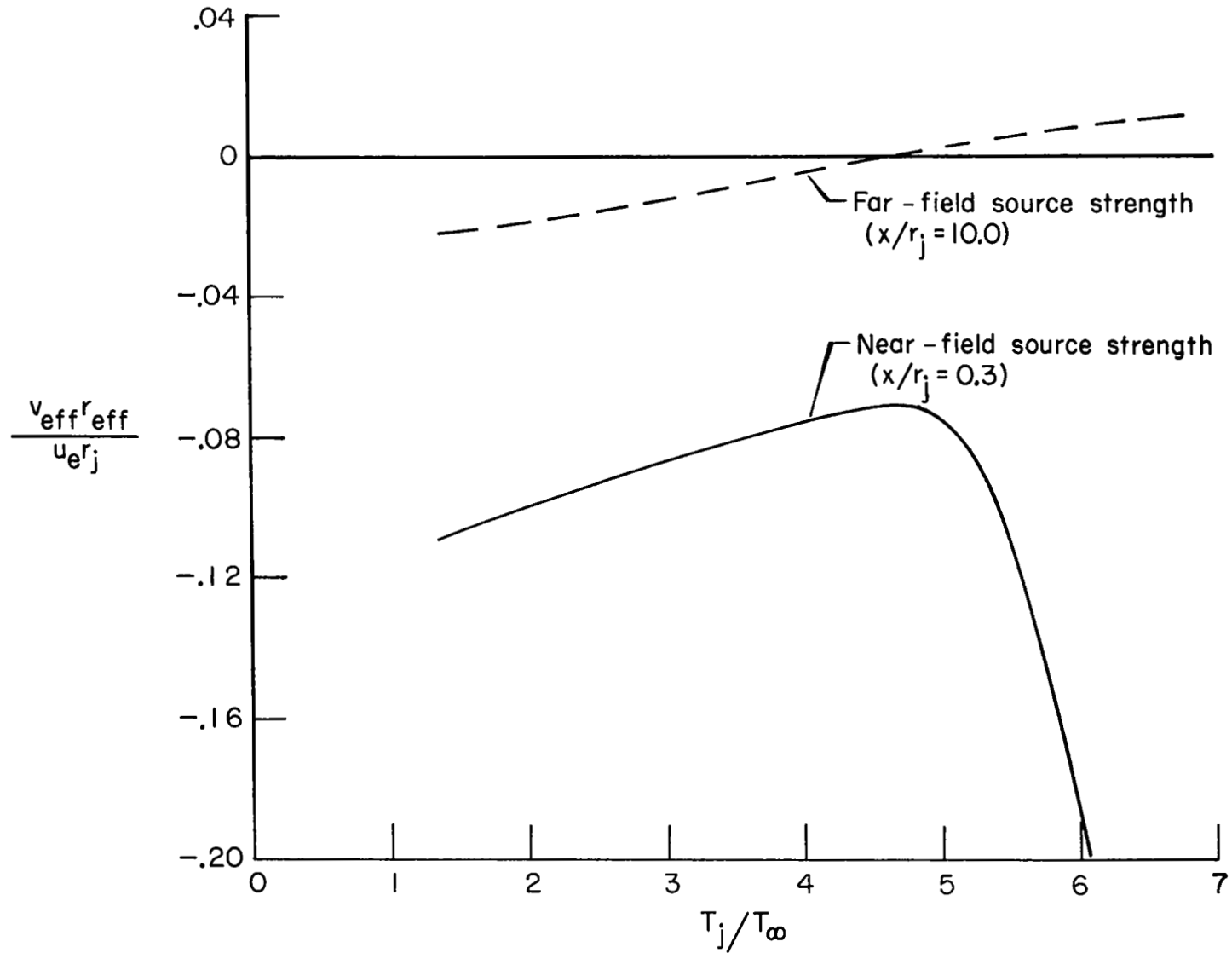
Figure 32.- Comparison of near-field and far-field source strength variations with jet exhaust temperature. $M_\infty = 0.4$; NPR = 2.0.
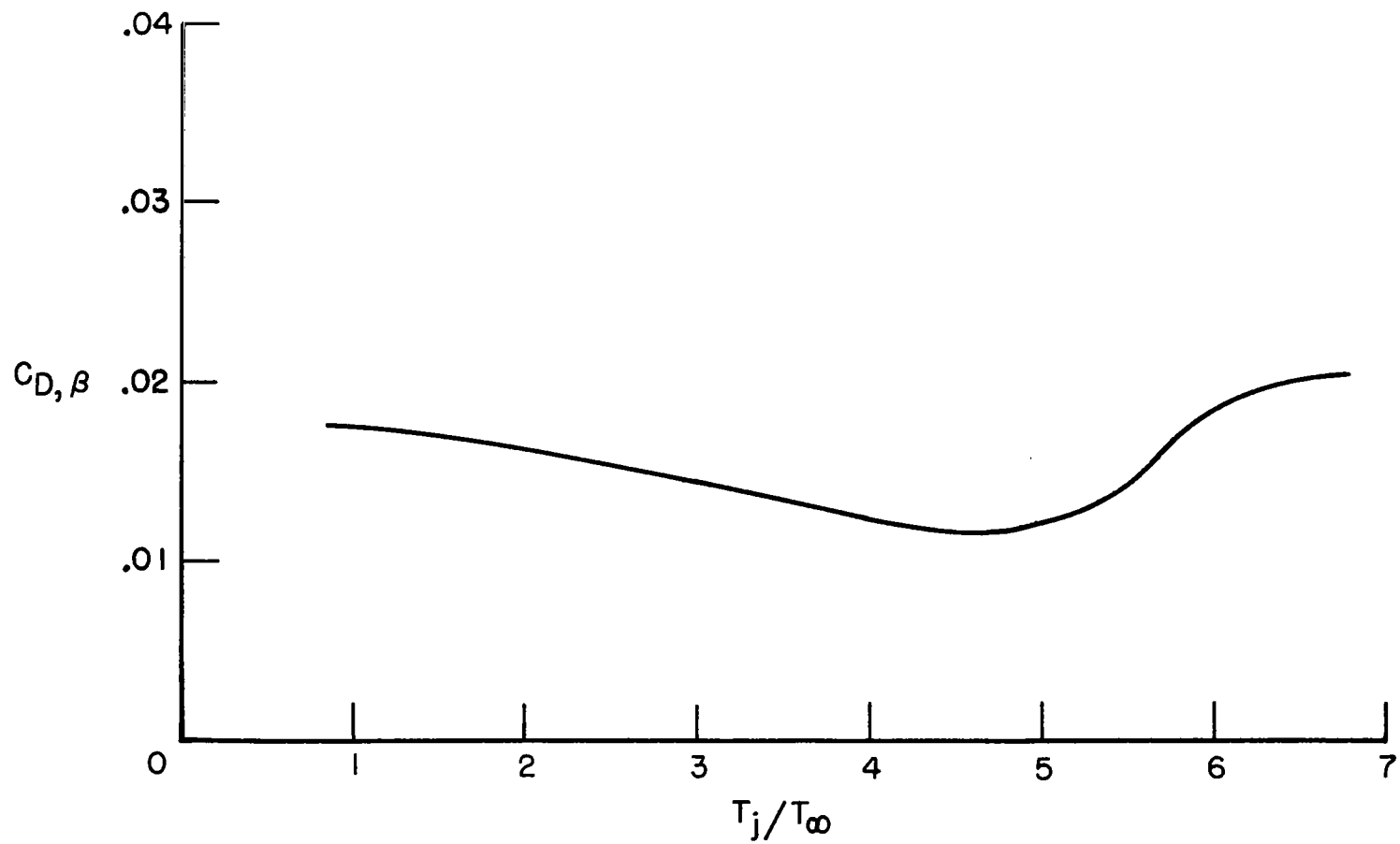
Figure 33.- Effect of jet exhaust temperature on predicted boattail drag.
$M_\infty = 0.4$;   NPR = 2.0; $W_j/W_\infty = 1.0$.
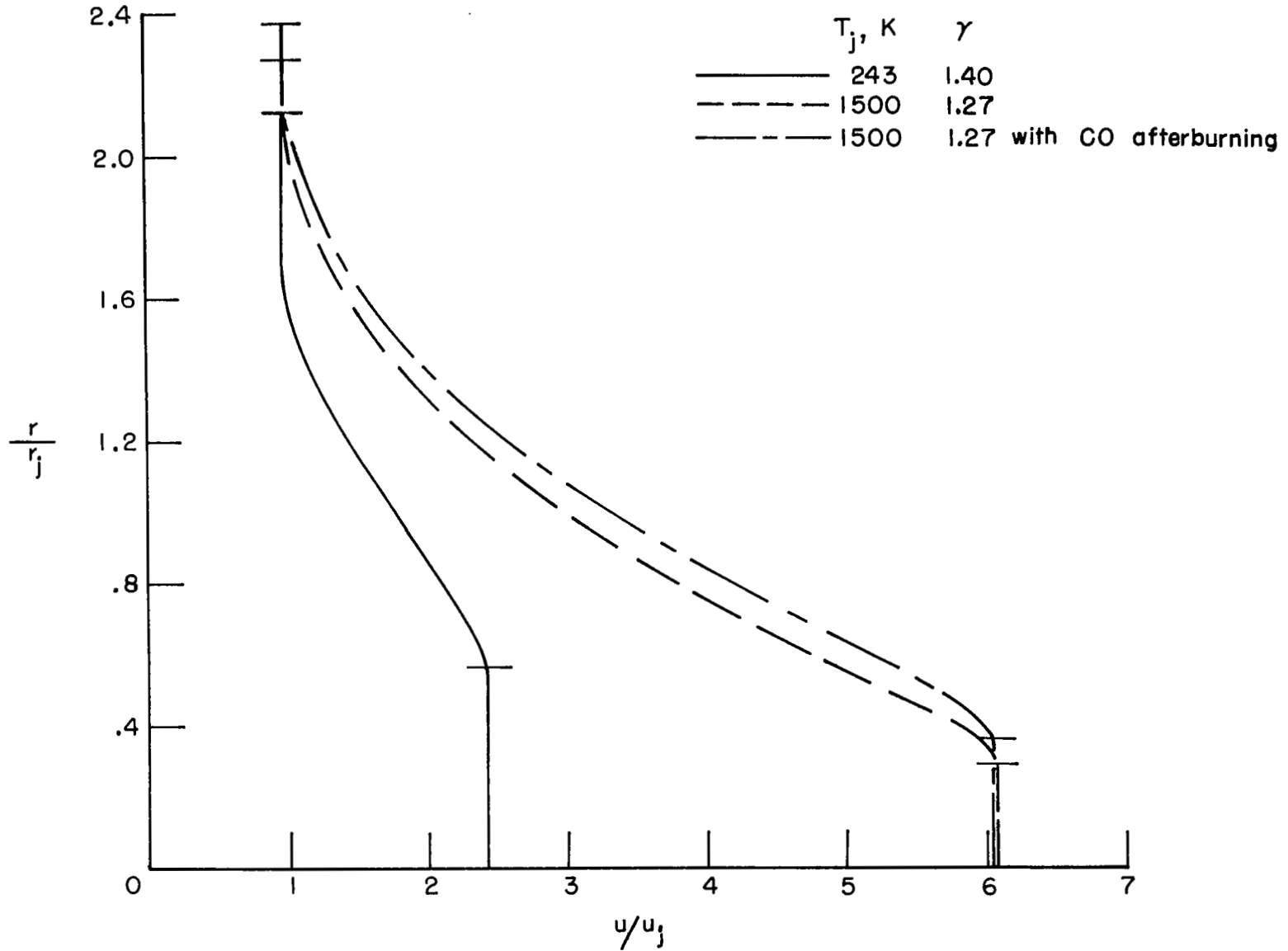
(a) Velocity profiles.

Figure 34.- Effect of CO afterburning on mixing-layer profiles. $M_\infty = 0.4$; NPR = 2.0; $x/r_j = 12$.
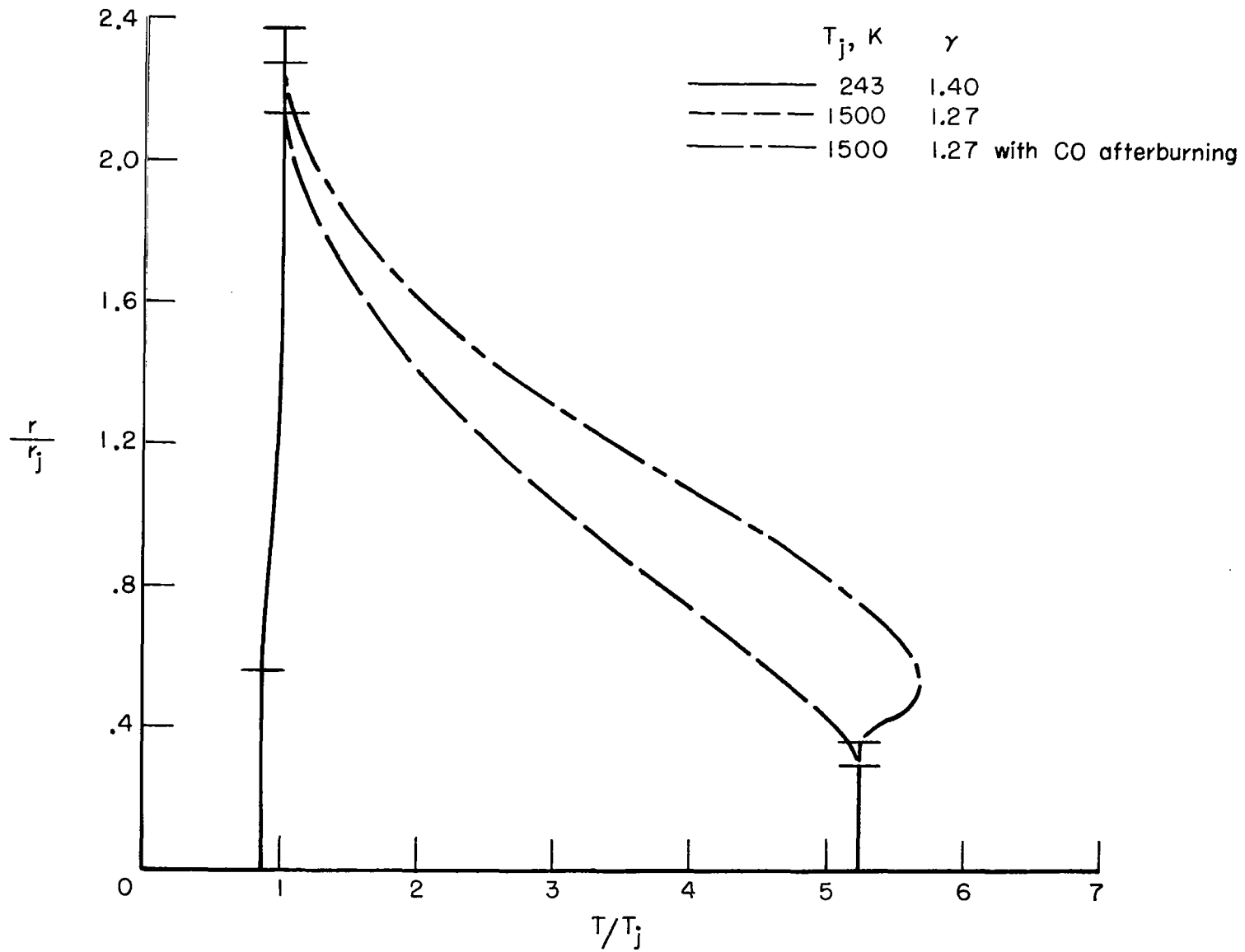
(b) Temperature profiles.

Figure 34.- Continued.
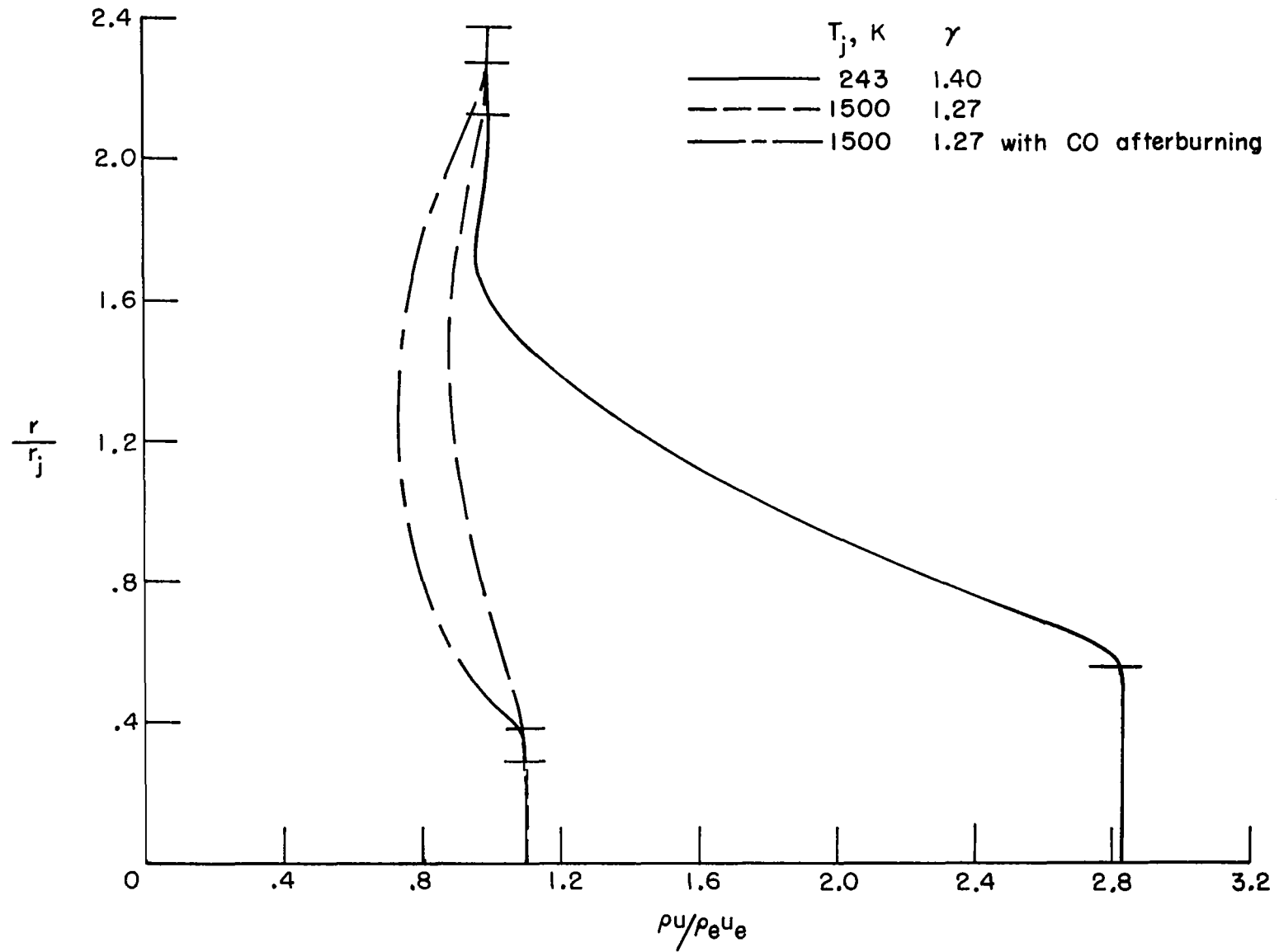
(c) Mass-flux profiles.

Figure 34.- Concluded.
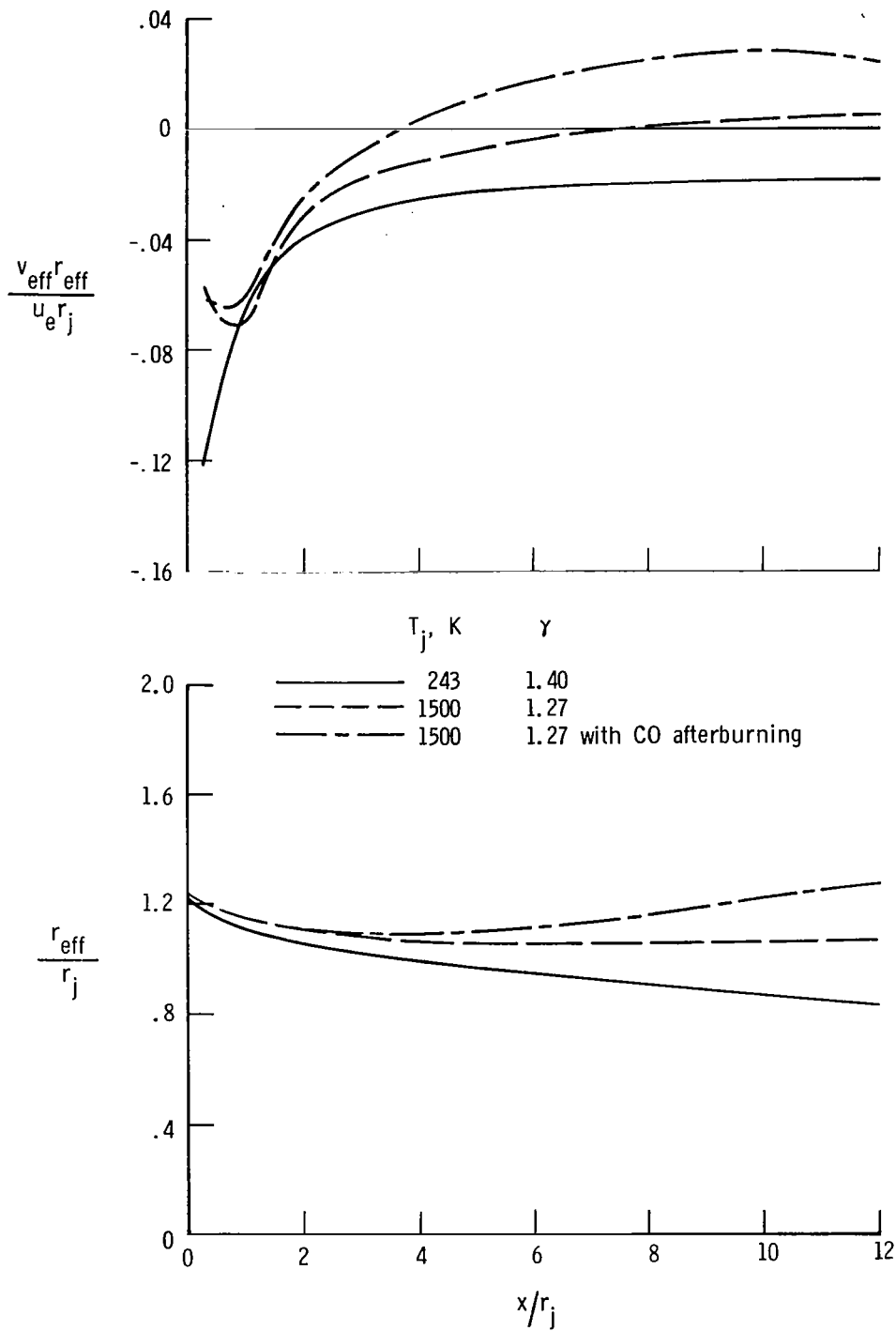
Figure 35.- Effect of CO afterburning on effective plume boundary and source strength distribution. $M_\infty = 0.4$; NPR = 2.0.
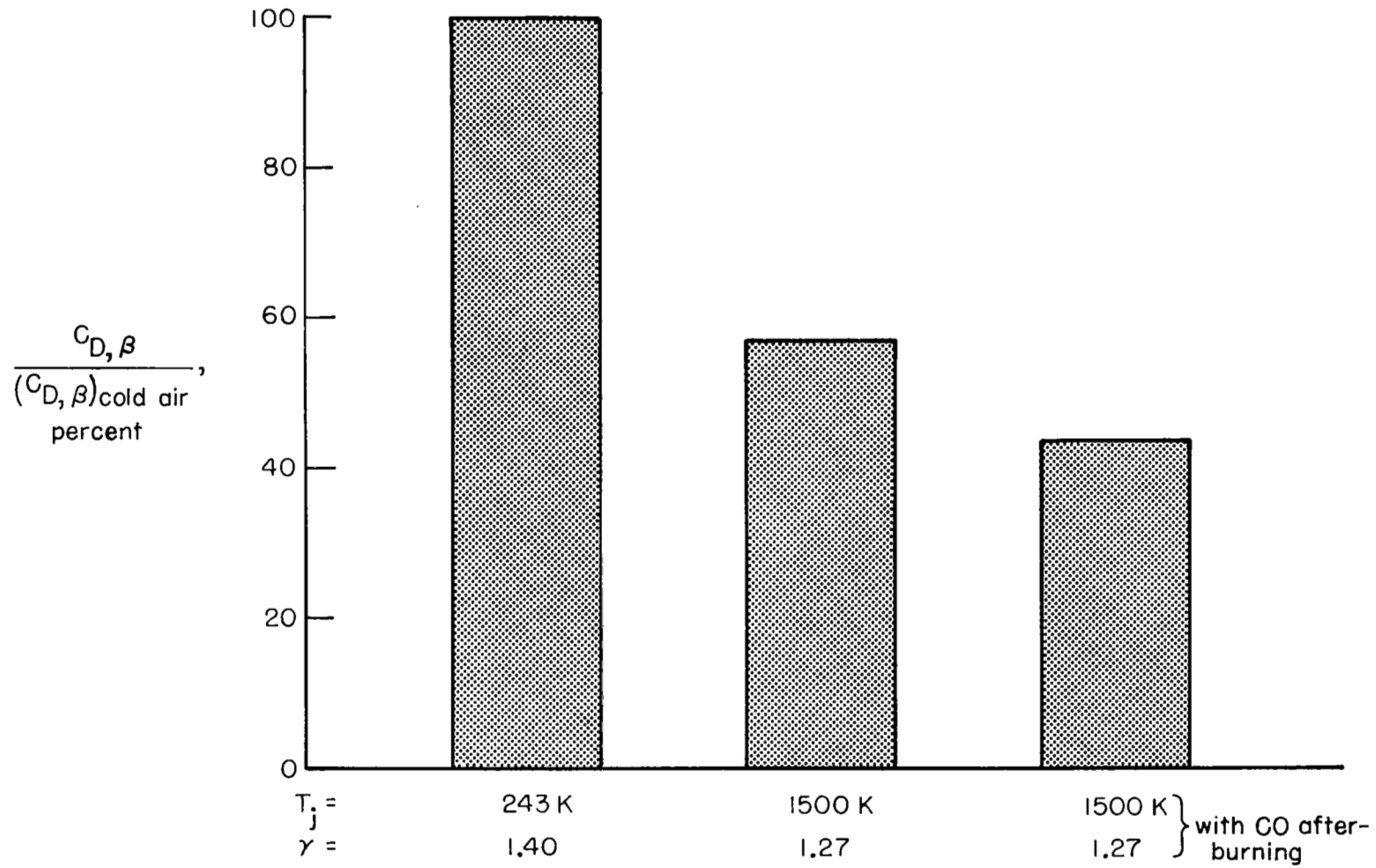
Figure 36.- Effect of CO afterburning on predicted boattail drag.
$M_{\infty} = 0.4$;   NPR = 2.0.

1. Report No. NASA TP-1626	2. Government Accession No.	3. Recipient's Catalog No.
4. Title and Subtitle VISCOUS-INVISCID CALCULATIONS OF JET ENTRAINMENT EFFECTS ON THE SUBSONIC FLOW OVER NOZZLE AFTERBODIES		5. Report Date April 1980
		6. Performing Organization Code
7. Author(s) Richard G. Wilmoth		8. Performing Organization Report No. L-13362
9. Performing Organization Name and Address NASA Langley Research Center Hampton, VA 23665		10. Work Unit No. 505-32-13-01
		11. Contract or Grant No.
12. Sponsoring Agency Name and Address National Aeronautics and Space Administration Washington, DC 20546		13. Type of Report and Period Covered Technical Paper
		14. Sponsoring Agency Code

15. Supplementary Notes

16. Abstract

A viscous-inviscid interaction model has been developed to account for jet entrainment effects in the prediction of the subsonic flow over nozzle afterbodies. The model is based on the concept of a weakly interacting shear layer in which the local streamline deflections due to entrainment are accounted for by a displacement-thickness type of correction to the inviscid plume boundary. The entire flow field is solved in an iterative manner to account for the effects on the inviscid external flow of the turbulent boundary layer, turbulent mixing and chemical reactions in the shear layer, and the inviscid jet exhaust flow. The components of the computational model are described, and numerical results are presented to illustrate the interactive effects of entrainment on the overall flow structure. The validity of the model is assessed by comparisons with data obtained from flow-field measurements on cold-air jet exhausts. Numerical results and experimental data are also given to show the entrainment effects on nozzle boattail drag under various jet exhaust and free-stream flow conditions.

17. Key Words (Suggested by Author(s)) Jet entrainment Nozzle afterbodies Viscous-inviscid interactions	18. Distribution Statement Unclassified - Unlimited Subject Category 02		
19. Security Classif. (of this report) Unclassified	20. Security Classif. (of this page) Unclassified	21. No. of Pages 76	22. Price* $6.00

NASA-Langley, 1980

National Aeronautics and
Space Administration

Washington, D.C.
20546

Official Business
Penalty for Private Use, $300

U.S.MAIL

3   1 1U, A,   040180 S00903DS
DEPT OF THE AIR FORCE
AF WEAPONS LABORATORY
ATTN: TECHNICAL LIBRARY (SUL)
KIRTLAND AFB NM 87117

NASA